



UNIVERSITY OF
BIRMINGHAM

**OPTICAL INVESTIGATION ON THE SPRAY
AND COMBUSTION CHARACTERISTICS OF
THE FURAN BIO-FUELS**

By

Changzhao Jiang

A thesis submitted to

The University of Birmingham

For the degree of

DOCTOR OF PHILOSOPHY

School of Mechanical Engineering

The University of Birmingham

September 2014

UNIVERSITY OF
BIRMINGHAM

University of Birmingham Research Archive

e-theses repository

This unpublished thesis/dissertation is copyright of the author and/or third parties. The intellectual property rights of the author or third parties in respect of this work are as defined by The Copyright Designs and Patents Act 1988 or as modified by any successor legislation.

Any use made of information contained in this thesis/dissertation must be in accordance with that legislation and must be properly acknowledged. Further distribution or reproduction in any format is prohibited without the permission of the copyright holder.

Abstract

The spray and combustion characteristics of the new bio-fuel candidates, 2,5-dimethylfuran (known as DMF) and 2-methylfuran (known as MF), are examined using optical diagnostic methods.

A macroscopic spray characteristics study using high speed imaging has been performed to gain the understanding of the bio-fuels' spray behavior under various conditions compared to gasoline and isooctane. It is found that at different injection pressure and back pressure, the penetration lengths of the 5 fuels (MF, DMF, ethanol, isooctane and gasoline) are quite similar. However, the penetration lengths of the two new bio-fuels, especially DMF, are longer than the gasoline at elevated temperatures due to their higher boiling points.

The droplet sizes of the bio-fuel injections under different operating conditions are also studied using Phase Doppler Particle Analyzer (PDPA). The study indicates that the fuels' properties (e.g. surface tension, viscosity, density, boiling point) have considerable impacts on the atomization of the spray. Moreover, the differences of these properties lead to different droplet size orders for the fuels at different test conditions. It should be note that the alternative fuels, MF and DMF, did have similar droplet sizes at various test conditions compared to the benchmark gasoline and isooctane. This was a good sign for them to be used in current GDI engines.

The laminar flame propagation and the turbulent flame propagation for MF and DMF have been benchmarked against isooctane. The laminar burning velocity of MF is around 17% faster than that of DMF and around 30% faster than that of isooctane. For turbulent flame

propagation in the engine cylinder, MF has the fastest flame area growth rate, highest peak flame speed and quickest heat release rate at different loads compared to the other two fuels due to its higher laminar burning velocity. Four functions have been constructed to reveal the close link between the flame in 2-D form and the combustion parameters in the cylinder. They offered alternative ways to estimate the combustion process and combustion parameters in the cylinder using photography method rather than using the pressure data.

Acknowledgements

Firstly, I am sincerely grateful for the guidance from my supervisor: Professor Hongming Xu. Without his help and patient instruction, my PhD work can never be finished. The support from Dr Steve Richardson, my second supervisor, is also greatly appreciated.

Many thanks to all my colleagues at the future power system department. They are all very nice persons and offered me useful advices. I wish them all the best with their future life and careers. In particular, I would like to thank Dr Xiao Ma for his tremendous help and support on all the work I undertook. Also, the help from my colleague, Thomas Lattimore, on the grammar is appreciated.

Great thanks go to the technicians in the department- Carl Hingley, Peter Thornton, Lee Gauntlett and Simon Rowan for their kindly support with the facility set up and maintenance.

Finally, I would like to thank my wife, Jieling Zhou, for her support and encouragement throughout my PhD period. I also thank my father, Hejian Jiang, and my mother, Huarong Zhao, who support me all the time in my life.

Contents

Abstract	I
Acknowledgements	III
Contents	IV
List of Figures	VI
List of Tables	XI
List of Abbreviations	XII
List of Publications	XV
Chapter 1	1
1 Introduction	1
1.1 Background	1
1.2 Research Outline	3
1.3 Objective and Approaches	4
1.4 Thesis Outline	5
Chapter 2	8
2 Literature Review	8
2.1 Modern Gasoline Direct-Injection (GDI) Engines	8
2.2 Bio-fuels for Spark Ignition Engines	21
2.3 Spray Characteristic of the GDI Injector	25
2.4 Laminar Premixed Flame and Turbulent Premixed Flame	31
2.5 Summary	36
Chapter 3	38
3 Experimental Set up and Techniques	38
3.1 Spray Image Acquisition System	38
3.2 PDPA system	43
3.3 Schlieren System	46
3.4 Optical Engine and PLIF Laser	48
3.5 Data Processing	61
3.6 Experiment Uncertainty Analysis	80
3.7 Summary	83
Chapter 4	85
4 Macroscopic Spray Characteristics	85

4.1	Introduction	85
4.2	Test Conditions and the Properties of the Fuel.....	85
4.3	High Speed Imaging Results	88
4.4	Summary	105
Chapter 5	108
5	Droplet Size and Velocity Measurement	108
5.1	Introduction	108
5.2	Test Conditions and calculation of	109
5.3	Results and Discussion.....	110
5.4	Summary	134
Chapter 6	137
6	Laminar Flame Characteristics of 2, 5-dimethylfuran and 2-methylfuran.....	137
6.1	Introduction	137
6.2	System Validation.....	138
6.3	Flame Morphology	140
6.4	Stretched and Unstretched Flame Speed	142
6.5	Adiabatic Flame Temperature and Laminar Burning Velocities	146
6.6	The Flame Instability.....	149
6.7	Summary	155
Chapter 7	157
7	Turbulent Flame Behavior in the Engine	157
7.1	Introduction	157
7.2	Test Conditions.....	158
7.3	Pressure Trace and Combustion Phase.....	158
7.4	Flame Propagation.....	160
7.5	OH-LIF.....	172
7.6	Summary	183
Chapter 8	186
8	Conclusions	186
8.1	Summary and Conclusions.....	186
8.2	Future Work.....	191
List of References	193

List of Figures

Figure 2-1: Mixture formation in gasoline engines (Celik, 2010).....	12
Figure 2-2: Operating modes in gasoline engines (Celik, 2010)	13
Figure 2-3: The direct-injection spark-ignition combustion systems(Celik, 2010).....	14
Figure 2-4 : Three kinds of GDI injectors (Zhao, 2009c).....	17
Figure 2-5: Spray structure (Hiroyasu, 1990).....	26
Figure 2-6: Jet stability curve (Dumouchel, 2008)	27
Figure 3-1: High speed image acquisition system for spray in the vessel	39
Figure 3-2: Constant volume vessel with heating units in 8 corners of the vessel	40
Figure 3-3: The multi-hole GDI injector (AJ133)	41
Figure 3-4: High speed camera coupled with the intensifier	42
Figure 3-5: Flame image in the cylinder (a) without the intensifier (b) with the intensifier	43
Figure 3-6: PDPA system working theory	44
Figure 3-7: PDPA system used in this study.....	45
Figure 3-8: Schlieren system setup.....	47
Figure 3-9: Single cylinder optical engine.....	49
Figure 3-10: Schematic of the optical engine, instrumentation and acquisition systems	50
Figure 3-11: Optical engine piston and full stroke transparent optical liner	55
Figure 3-12: The engine timing control system control panel.....	56
Figure 3-13: The beam expander for OH-LIF	60
Figure 3-14: Measurement of the spray tip penetration (a) Original image (b) Image processed by MATLAB code (c) Transformation from visual length to real length (d) Measurement of the cone angle	62
Figure 3-15: Effect of different thresholds on the penetration length measurement.....	65
Figure 3-16: Scattering modes of a set of rays incident on a liquid droplet	65

Figure 3-17: Effect of refractive index changes on PDA phase factor (Picher, 1991).	67
Figure 3-18: Laminar flame radius detection.....	71
Figure 3-19: Imaging processing using different thresholds.	73
Figure 3-20: Flame speed calculation (a) Normal condition (b) Flame partly beyond the window range.....	76
Figure 3-21: The schematic graphic of the piston window and the laser sheet region	77
Figure 3-22: Image processing for OH-LIF using different thresholds.....	79
Figure 4-1: Spray of the five fuels under different ambient conditions (1ms ASOI)...	89
Figure 4-2: Penetration length of different fuels under 150 bar injection pressure (a) ambient temperature 20°C, ambient pressure 1 bar (b) ambient temperature 20°C, ambient pressure 7 bar (c) ambient temperature 90°C, ambient pressure 1 bar	91
Figure 4-3 : Spray cone angle of different fuels under 150 bar injection pressure (a) ambient temperature 20°C, ambient pressure 1 bar (b) ambient temperature 20°C, ambient pressure 7 bar	94
Figure 4-4: Spray of MF, DMF and gasoline under three injection pressures (1 ms ASOI).....	97
Figure 4-5: Penetration length of MF and DMF under different injection pressures compared with gasoline (ambient temperature 20°C, ambient pressure 1bar)	97
Figure 4-6: Spray cone angle of MF and DMF under different injection pressures compared with gasoline	98
Figure 4-7: Spray images under different back pressure (1ms ASOI).....	100
Figure 4-8: Penetration length of MF and DMF under different ambient pressures compared with gasoline (ambient temperature 20°C, injection pressure 150 bar)	100
Figure 4-9: Spray cone angles of MF and DMF under different ambient pressures compared with gasoline	101
Figure 4-10: Spray images at different vessel temperatures (1 ms ASOI).....	103
Figure 4-11: Penetration length of MF and DMF under different ambient temperatures compared with gasoline (ambient pressure 1 bar, injection pressure 150 bar)	104
Figure 4-12: Spray cone angle of MF and DMF under different ambient temperatures compared with gasoline	105
Figure 5-1: Droplet velocity of gasoline against time at ambient conditions and an	

injection pressure of 150 bar (40 mm from the nozzle).....	111
Figure 5-2: The SMD and mean velocity of gasoline at different positions.....	112
Figure 5-3: SMD values of the tested fuels throughout the spray (Test conditions: 150 bar injection pressure, 1 bar back pressure, 20°C vessel temperature).....	116
Figure 5-4: SMD values and droplet velocity (40 mm from the nozzle) of the five fuels under 150 bar injection pressure, 1 bar back pressure and vessel temperature of 20 °C.....	117
Figure 5-5: Reynolds number and Weber number of MF and DMF at nominal conditions.....	118
Figure 5-6: Histogram of the five fuels at nominal conditions (40 mm from the nozzle).....	119
Figure 5-7: SMD values and droplet velocity of MF and DMF under three injection pressures, 1 bar back pressure and vessel temperature of 20 °C.....	120
Figure 5-8: Reynolds number and Weber number of MF and DMF at different injection pressures.....	121
Figure 5-9: Histogram of MF and DMF at different injection pressures (40 mm from the nozzle).....	121
Figure 5-10: SMD values and droplet velocities of the five fuels under 50 bar injection pressures, 1 bar back pressure and vessel temperature of 20 °C.....	124
Figure 5-11: Reynolds number and Weber number of the fuels at injection pressure of 50bar	124
Figure 5-12: SMD values and droplet velocity of MF and DMF under three back pressures, 150 bar injection pressure and vessel temperature of 20 °C.	126
Figure 5-13: Reynolds number and Weber number of MF and DMF under different back pressures	126
Figure 5-14: Histogram of MF and DMF at different back pressures (Injection pressure 150bar, vessel temperature 20°C and measured at 40 mm from the nozzle).....	127
Figure 5-15: SMD values and droplet velocity of the five fuels under 7 bar back pressures, 150 bar injection pressure and vessel temperature of 20 °C.	129
Figure 5-16: Reynolds number and Weber number of the fuel injections under back pressure of 7bar.....	129

Figure 5-17: SMD values and droplet velocities of MF and DMF under 150 bar injection pressures, 1 bar back pressure vessel temperature of 20°C, 60°C and 90°C.	131
Figure 5-18: Reynolds number and Weber number of MF and DMF at different ambient temperatures	132
Figure 5-19: Histogram of MF and DMF at different vessel temperatures (40 mm from the nozzle).....	132
Figure 5-20: Ohnesorge diagram for the injection.....	133
Figure 6-1: Laminar burning velocities and Markstein Length of isooctane-air mixtures versus equivalence ratios at 0.1MPa pressure and elevated initial temperature	139
Figure 6-2: Chronological schlieren images of stoichiometric fuel-air mixtures at initial temperature of 90°C.	141
Figure 6-3: Stretched flame speed of the test fuels at 120°C initial temperature at different equivalence ratios and stretch rates.....	144
Figure 6-4: Unstretched flame speed of the test fuels at different temperatures and equivalence ratios.....	145
Figure 6-5: Adiabatic flame temperatures for three fuels at 120 °C with varying equivalence ratios.....	146
Figure 6-6: Laminar burning velocities of test fuels at different temperatures and equivalence ratios.....	148
Figure 6-7: Markstein length of test fuels at different temperatures and equivalence ratios.....	151
Figure 6-8: Flame thickness (solid line) and density ratio (dot line) versus equivalence ratio for (a) MF under three temperatures (b) three fuels under 90°C.	153
Figure 6-9: Burning flux versus equivalence ratio for (a) MF under three temperatures (b) three fuels under 120°C.	155
Figure 7-1: In-cylinder Pressures and MFB (a) IMEP 4.5bar (b) IMEP 5.5bar	159
Figure 7-2: Single cycle images.....	162
Figure 7-3: Flame area and MFB data analyses (a) MFB and normalized area at IMEP 4.5bar (b) MFB and normalized area at IMEP 5.5bar (c) Correlation between flame	

area and MFB (4.5bar) (d) Correlation between flame area and MFB (5.5bar).....	163
Figure 7-4: Flame speed and ROHR (a) Flame speed and ROHR at IMEP 4.5bar (b) Flame speed and ROHR at IMEP 5.5bar (c) Correlation between flame speed and ROHR (4.5bar) (d) Correlation between flame speed and ROHR (5.5bar). (Scattering points: experiment data; lines: fitting results).....	167
Figure 7-5: The comparison of the flame speeds (a) IMEP 4.5 bar (b) IMEP 5.5 bar.....	169
Figure 7-6: The validation for the speed-ROHR function form (Sementa, 2011)....	171
Figure 7-7: ROHR and Normalized LIF Signal (IMEP=4.5bar) (a) Isooctane (b) DMF (c) MF	173
Figure 7-8: ROHR and Normalized LIF Signal (IMEP=5.5bar) (a) Isooctane (b) DMF (c) MF	175
Figure 7-9: Normalized LIF Signal.....	177
Figure 7-10: Interval between the OH and ROHR peaks with IMEP 4.5 bar and 5.5 bar	177
Figure 7-11: Correlations among LIF signal, MFB and flame area (a) OH-LIF versus MFB at IMEP 4.5bar (b) OH-LIF versus MFB at IMEP 5.5bar (c) OH-LIF versus Flame area at IMEP 4.5bar (d) OH-LIF versus Flame area at IMEP 5.5bar (Scattering points: experiment data; lines: fitting results).....	179
Figure 7-12: The validation for the LIF-MFB function form (Collin, 2003).....	182

List of Tables

Table 3-1: Specification of the camera and the intensifier.....	42
Table 3-2: The optical engine specification	52
Table 3-3: Calculation of the refractive index under different temperatures.....	68
Table 4-1: Test conditions for the high speed spray imaging test.....	86
Table 4-2 : Properties of the test fuels	87
Table 4-3: Vapor pressures of MF, DMF, Isooctane and Ethanol at different pressures.....	90
Table 5-1: Test conditions for PDPA test	109
Table 5-2: Summary of the trends for W_b , Re , and SMD at 50 bar and 150 bar injection pressure.....	123
Table 5-3: Summary of the trends for W_b , Re , and SMD at 1 bar and 7 bar back pressure.....	127
Table 5-4: Test conditions for the Ohnesorge numbers plotted in Figure 5-20.....	134
Table 7-1: Ignition delays	159
Table 7-2: The adiabatic flame temperatures and un-stretched laminar flame speeds of the three fuels.....	161
Table 7-3: Fitting results for flame area-MFB	165
Table 7-4: Fitting results for flame speed-ROHR.....	170
Table 7-5: The parameters for fittings in Figure 7-6.....	172
Table 7-6: Fitting results for OH-MFB	180
Table 7-7: Fitting results for OH-Flame	183

List of Abbreviations

aTDC	after top dead center
A_f	flame front area
ASOI	after start of injection
bTDC	before top dead center
CAD	crank angle degree
CAI	controlled auto ignition
CCD	charge-coupled device
CO	carbon monoxide
CO ₂	carbon dioxide
DISI	direct injection spark ignition
DMF	2, 5-dimethylfuran
EGR	exhaust gas recirculation
ETH	ethanol
EVC	exhaust valve close
EVO	exhaust valve open
f	laminar burning flux
FWHM	Full width at half maximum
GDI	gasoline direct-injection
HC	unburned hydrocarbons
HCCI	homogenous charged compression ignition
HMF	5-hydroxymethylfurfural
ICE	internal combustion engine
IMEP	indicated mean effective pressure
ISO	isooctane
IVO	intake valve open
L_b	Markstein length
LHV	lower heating value
LIF	Laser induced fluorescence

m	turbulence intensity
MBT	maximum break torque
MF	2-methylfuran
MFB	mass fraction burned
MON	motor octane number
NO	nitrogen oxide
NO _x	nitrogen oxides
n _b	mole numbers of products
n _u	mole numbers of reactants
P	pressure
PDPA	phase doppler particle analyzer
PFI	port fuel injection
PLIF	Planar laser-induced fluorescence
PM	particulate matter
Re	Reynolds number
r _u	instantaneous flame radius
ROHR	rate of heat release
RON	research octane number
RPM	revolutions per minute
SI	spark ignition
S _L	laminar flame speed
SMD	Sauter mean diameter (D ₃₂)
S _n	stretched laminar flame speed
S _s	laminar flame speed
T _b	adiabatic flame temperatures
TDC	top dead center
T _u	initial temperatures
THC	hydrocarbon emissions
We	Weber number
Y _{dil}	mass fraction of the diluent
α	stretched rate

δ	surface tension
δ_l	flame thickness
λ	relative air to fuel ratio
μ_l	laminar burning velocity
ρ_b	burned mixture densities
ρ_u	unburned mixture densities
Φ	equivalence ratio

List of Publications

1. **An optical study of DMF and Ethanol combustion under dual-injection strategy;** Changzhao Jiang, Xiao Ma, Hongming Xu, Steve Richardson; SAE Technical Paper: 2012-01-1237
2. **In-cylinder optical study on combustion of DMF and DMF fuel Blends;** Xiao Ma, Changzhao Jiang, Hongming Xu, Steve Richardson; SAE Technical Paper: 2012-01-1235
3. **Laminar burning characteristics of 2-methylfuran compared with 2,5-dimethylfuran and isooctane;** Xiao Ma, Changzhao Jiang, Hongming Xu, Shijin Shuai, Haichun Ding; *Energy Fuels*, 2013, 27 (10), pp 6212–6221
4. **Laminar burning characteristics of 2-methylfuran and isooctane blend fuels;** Xiao Ma, Changzhao Jiang, Hongming Xu, Haichun Ding, Shijin Shuai; *Fuel* 116(2014)281-291
5. **Ultra-High speed imaging and OH-LIF study of DMF and MF combustion in a DISI optical engine;** Xiao Ma, Hongming Xu, Changzhao Jiang, Shijin Shuai; *Applied Energy* 122 (2014):247-260
6. **Investigation of the spray characteristics of DMF-isooctane blends using PDPA;** Po-wen Tu, Changzhao Jiang et al.; SAE Technical Paper 2014-01-1408.
7. **Evaluation of the spray characteristics of the furan bio-fuels under elevated back pressure and temperature;** Changzhao Jiang, Haichun Ding, Po-wen Tu et al.; Prepared to submitted.

Chapter 1

Introduction

1.1 Background

Recently, the use of fossil fuels has caused several issues which arouse extensive concerns among the public and fuel researchers. The first concern is that the diminishing oil reserve cannot fulfill the increasing oil consumption for very long. The world oil consumption rate has been continuously increasing since the middle of the 1980s, due to the rapid increasing demand from developing countries especially China (Energy Statistic, 2014). Following this trend, unless some effect is made to slow down the speed of this consumption, the reported oil reserve will be exhausted in half a century (Energy Statistic, 2014). The second concern is the global warming effect due to the increasing proportion of CO₂ in the air. The global warming effect can cause many disastrous consequences which include global temperature increase, species extinction and sea level rise. In order to ensure the supply of liquid fuels and to balance the CO₂ level in the atmosphere, sustainable alternative fuels should be found and put into use by fuel researchers; research in this key area is urgently needed.

Several solutions have been proposed by the researchers. Hydrogen is considered as a clean and sustainable alternative for gasoline and diesel. Its abundance, high energy density by mass and zero CO₂ emissions make it attractive. However, the main obstructions for using hydrogen as a vehicle fuel are the safety issues and the

infrastructure needed for refilling. The strict requirements for hydrogen storage and the necessary new hydrogen refill points make it impossible put into widespread use in the short term.

Battery powered vehicles seem to be another solution. Electric vehicles generate no emissions at all and it is very easy to find a plug which allows the battery to be charged. The success of Tesla motors (Tesla Motors, 2014) is proving that there is a promising future for the battery powered vehicle in the market. However, the aforementioned problems still remain unsolved from the author's perspective: the electricity needed for the electric vehicles is mainly generated by thermal power plants and thermal power plants mainly consume coal to generate energy. In this way, a large amount of CO₂ is still emitted into the atmosphere. Also, due to the limitation of the transfer efficiency between the power plug and the car battery, the use of electric vehicles is not really clean.

Currently, the most extensively used short term solution is bio-ethanol. In many countries, ethanol is added into gasoline in order to slow down the speed of using fossil fuel and to balance the amount of CO₂ in the atmosphere. Its renewable nature and mature production method make it favorable. A large amount of research has been carried out on the use of ethanol as a fuel in the internal combustion engine. However, its limitation, which associated with its low energy density and high energy need in the production process, hinders its further development.

Therefore, it is very important to select bio-fuels that have high energy density, reliable high yield and high combustion efficiency. Amongst the possible candidates, the furan derivatives fit the role well and are rapidly becoming gasoline alternatives.

1.2 Research Outline

In order to commercialize bio-fuels, their spray behaviours should be examined and understood because they affect the combustion and emissions. Therefore, the research presented in this thesis gives detailed analysis on the bio-fuels' macroscopic spray characteristics (penetration length and cone angle) compared to ethanol and gasoline.

The microscopic spray characteristics, including the droplet size and the droplet velocity, are also studied. The sensitivity of these furan bio-fuels to the injection pressure, ambient pressure, and the ambient temperature is investigated.

The laminar burning characteristics are studied in order to understand the fundamental knowledge concerning the fuels' burning behaviour. The flame instabilities of the bio-fuels are analyzed and compared to those of isooctane.

The last part of this thesis examines the combustion of the bio-fuels in the optical engine using high speed imaging and OH-LIF. Correlations are made to present the relationship among the burning rate, the flame area and the OH signal. The effect of

engine load is also analyzed.

1.3 Objective and Approaches

The aim of this research was to investigate the spray and combustion characteristics of the two furan bio-fuels, DMF and MF, and compare their characteristics to the benchmarks, gasoline and isooctane. Several optical diagnostic techniques were used in order to measure these properties. This research can generate supporting information for engine designing and CFD modelling for the bio-fuels. The objectives include the following points:

1. To study the macroscopic spray characteristics of these bio-fuels in order to understand the differences between the bio-fuels and gasoline. The effects of injection pressure, back pressure, ambient temperature, and the fuel properties on the bio-fuels spray are also studied.
2. To investigate the fuel atomization characteristics and the influence of the test conditions on the droplet size and the droplet velocity.
3. To study the laminar flame propagation and the flame instability of the bio-fuels in a constant volume vessel.
4. To examine the turbulent flame propagation in the engine and compare the properties with various fuels including gasoline and ethanol.
5. To analyze the correlation between the laminar flame properties and the turbulent flame properties.
6. To analyze the possible effects of these bio-fuels being used in an engine.

1.4 Thesis Outline

This thesis is divided into eight chapters that contain the investigation into the spray and flames of the bio-fuels. A brief summary of each chapter is given below.

Chapter 1-Introduction

This chapter introduces the motivation and the main objectives of this study. The promising furan bio-fuels are introduced.

Chapter 2-Literature review

This chapter presents the review of the relevant literature. Firstly, the modern GDI engine and its related technologies are reviewed. Then, the second part introduces the bio-fuels used in spark ignition engines, especially the furan derivatives and then the review on spray characteristics of the GDI injector is given. The third part gives a review on spray characteristics of the GDI injector. Finally, an overview on the laminar flame propagation and in-cylinder flame propagation are presented in the next section; this includes the theory of both and the relationship between them.

Chapter 3-Experimental set up and techniques

This chapter includes the experimental facilities and the related techniques used in the study. Detailed descriptions are given of the facilities including the constant volume vessel, the fuel injection system, the optical engine and the high speed camera. The techniques used, which include high speed imaging, Schlieren photography and PDPA,

along with the related data analysis methods, are described.

Chapter 4-Macroscopic spray characteristics

The macroscopic spray characteristics, which mainly include the spray cone angle and the spray penetration, are examined with varied test conditions. The effect of the fuels, the injection pressures ambient temperature and the ambient pressure are analyzed.

Chapter 5 - Droplet size and velocity measurement

The effects of injection pressure, back pressure, the fuels properties and the vessel temperature on the droplet size and the velocity are examined using the PDPA technique. The comparison amongst the fuels is given and the potential of the bio-fuels is analyzed.

Chapter 6-Laminar flame characteristics of 2,5-dimethylfuran and 2-methylfuran

In this chapter, the laminar flame properties of the bio-fuels and air mixtures with varying initial temperatures (60°C, 90°C and 120°C) and equivalence ratios (0.6-1.1) at 0.1MPa initial pressure is studied using schlieren photography. The effect of these conditions on the stretched flame speed, unstretched flame speed, Markstein length, laminar burning velocity, flame thickness, density ratio and laminar burning flux of the fuel-air mixtures are discussed.

Chapter 7-Turbulent flame behaviour in the engine

The turbulent flame propagation speed, the burning rate, and the fluorescence signal are measured and correlated under varied engine loads. The comparison of these fuels is given and the potential of these fuels is discussed.

Chapter 8-Summary and future work

The main findings in the previous chapters are summarized in this chapter. Recommendations for future work are also given.

Chapter 2

Literature Review

The aim of this chapter is to review the literature related to the work in this thesis. It starts with a review of the modern GDI engine, which includes the mixture formation, the DISI combustion system, the GDI injector types and the engine-out emissions. The second part introduces the bio-fuels used in spark ignition engines, especially the furan derivatives and then the review on spray characteristics of the GDI injector is given. In this part the spray structure and break up theories are covered. Literature relevant to spray tip penetration, cone angle, spray droplet size and droplet velocities are discussed. Finally, an overview on the laminar flame propagation and in-cylinder flame propagation are presented in the next section; this includes the theory of both and the relationship between them.

2.1 Modern Gasoline Direct-Injection (GDI) Engines

2.1.1 GDI Engines Overview

The idea of gasoline direct injection dates back to the early 20th century. At that time, most of the work was focused on developing new aircraft piston engines with high power output and low fuel consumption for military uses (Zhao, 2009a). After the Second World War, this technology was transferred from aircraft engines to automotive engines. The first application of GDI on vehicles was introduced by Goliath and Gutbrod in 1952. Both companies' GDI systems were developed by

Bosch. Later, in 1955, Mercedes-Benz released the famous Mercedes-Benz 300SL, which was a sports car equipped with a GDI system developed by Bosch. In this period, the main aim of using GDI on a vehicle was to increase the performance of the vehicle through the charging cooling effect of direct fuel injection. In the 1970s, there was a short period when a large amount of research and development on GDI engines was carried out by Ford motor company and the American Motors Corporation (AMC) (Scussei, 1978). Ford developed a stratified-charge GDI engine called "PROCO" (programmed combustion). However, this project was soon cancelled because of the high cost and the high amount of NO_x emissions which could not meet the coming EPA (United States Environmental Protection Agency) limits. The AMC conducted research aimed to develop a Straticharge Continuous Fuel-Injection (SCFI) system in the early 1970s. In 1973, a road test on the prototype "Straticharge" engine was performed, but was stopped due to teething problems with the mechanical fuel control.

The real success of a GDI engine in a vehicle was achieved in the 1990s when Mitsubishi Motors introduced the Galant/Legnum 1.8L straight 4 into the Japanese market in 1996 (Iwamoto, 1997). Afterwards the other car manufacturers in Europe and Japan followed step by producing their own GDI engines or taking licenses from Mitsubishi. These engines adopted stratified operation at part load and low to medium speed; whereas homogeneous operation was used at high load and high speed. Until 2001, over one million GDI engines were manufactured by Mitsubishi.

However, with the stricter emissions' legislation after 2000, the fuel efficiency of the

engines became the second priority. For stratified lean-burn operations, the expensive and inefficient lean-burn NO_x aftertreatment has to be used in order to fulfill the emissions' legislation. As a result, GDI engines after 2001 were designed to operate only at homogeneous operation mode.

The later trend of the GDI engine development has been led by the Volkswagen (VW) and Audi group (Zhao, 2009b). They aggressively adopted turbochargers and superchargers in the GDI engines. The impressive TSI 1.4 litre GDI engine was able to produce 90kW/litre power density. The concept of engine downsizing, which means substituting the naturally aspirated engines by smaller displacement engines, became widely recognized and employed by the automotive manufacturers.

In recent years, the automotive industry faced new challenges not only due to the tougher emissions' legislation but also because of the need to reduce CO₂ emissions. The emissions of CO₂ attracted extensive concern due to their related greenhouse effect. So, the task for the automotive researchers was to increase the efficiency of the engines. The stratified lean-burn combustion was returned to the market as BMW introduced the efficient updated straight six-cylinder gasoline engine in 2007 (Schwarz, 2006). In summary, the current focus of GDI engine development was put on engine downsizing, which employed homogenous charge operation with boosting; the fuel economy and the emissions' benefits were gained simultaneously.

The future trend of GDI engine development is still ambiguous, but the aim of the development is clear: to achieve reductions in both CO₂ emissions and pollutant emissions. There are a few techniques available: advanced valve actuation systems,

boosting and premixed and diluted low temperature combustion including CAI/HCCI operation.

2.1.2 Mixture Formation and Operating Modes in the Gasoline Engine

According to how mixtures are prepared for combustion in the cylinder, gasoline engines can be classified into three types: the Carburetter injection, the port fuel injection (PFI) and the GDI. The features of the three types of mixture formation are shown in Figure 2-1. Due to the highly evaporable nature of gasoline, it is very convenient to generate homogenous flammable mixtures outside the cylinder using a Carburetter. Therefore, for a long time, the main method for mixture formation in a vehicle engine was to install a Carburetter on the main manifold. The work of a Carburetter relies on Bernoulli's principle: the faster the air moves, the lower the static pressure. As shown in Figure 2-1 a, the diameter of the throttle is smaller at the location of the Carburetter. When air flows through the Carburetter throttle, it speeds up and leads to the decrease of local pressure. The fuel is then sucked into the throttle and breaks into small droplets under the high speed air flow. The droplets are then vaporized; thus the mixture is formed and is taken into the cylinder. The carburetter provides a way to control the air/fuel ratio for the mixture. However, its mechanism makes it hard to control the air/fuel ratio accurately under varying working conditions. With the stringent emissions' legislation all over the world, a Carburetter is seldom used on vehicles now.

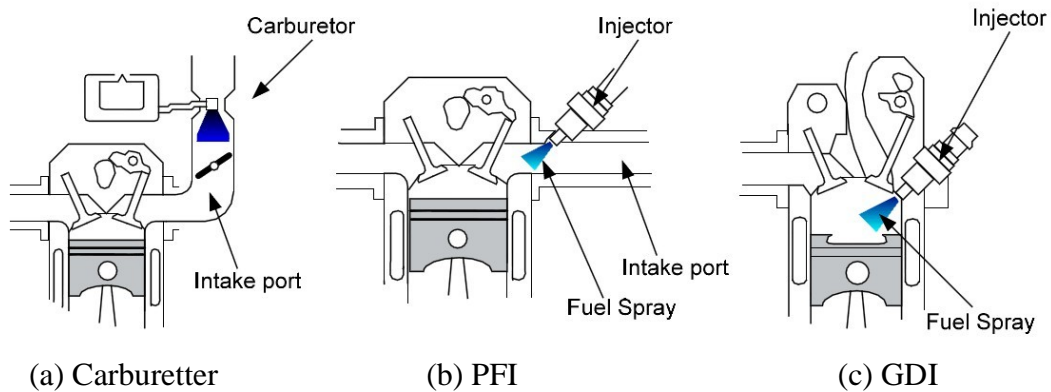
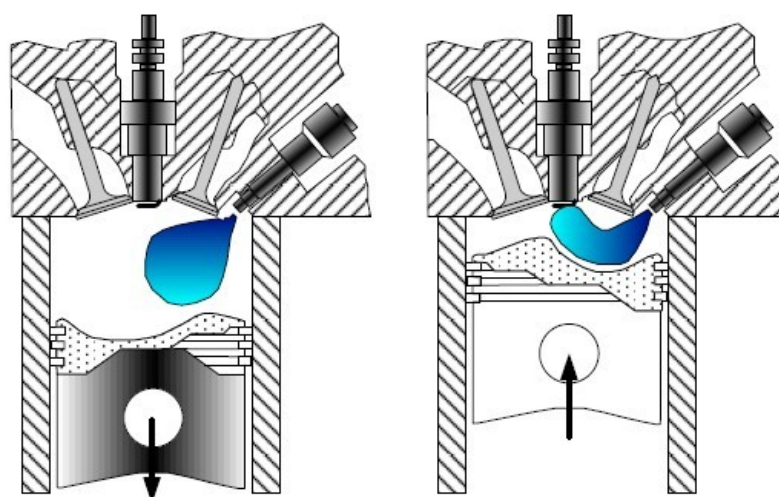


Figure 2-1: Mixture formation in gasoline engines (Celik, 2010)

The implementation of port fuel injection (PFI) was applied later in gasoline engines. In the PFI system, the fuel is pressurized by a pump to around 0.3MPa and then injected into the pre-vaporizing chamber by an injector to be vaporized. In the intake stroke, the air-fuel mixture will be inhaled into the cylinder. Then, in the compression stroke the mixture can be ignited. Compared to a Carburettor, the advantages of port fuel injection are improved volumetric efficiency, more accurate control of the equivalence ratio and more uniform fuel distribution. Thus, the PFI system was widely used on vehicles' engines. However, the PFI system also has its drawbacks. Its response during cold start and load change is not good. In order to precisely and instantly control the amount of fuel into the cylinder and further improve the fuel economy, the gasoline direct injection (GDI) system was developed.

For a GDI engine, there are two operating modes: homogeneous operation and stratified-charge operation (Figure 2-2). In the homogeneous operation, the fuel injection usually happens at the early intake stroke, which ensures the full mixture of the fuel and the air due to the long time interval between the injection and the ignition (as shown in Figure 2-2a, the fuel is injected at the intake stroke). This is similar to

the port fuel injection (PFI) where fuel and air are mixed uniformly. At high engine load, homogeneous (stoichiometric) operation has to be used in order to provide enough power to the engine. However, at low load, stratified operation could be applied to the engine due to its advantages of the unthrottled operation. Unthrottled stratified operation can largely reduce the pumping loss and heat loss, which accounts for a large proportion of the lost work in the engine operation. In order to realize stratified operation in an engine, the fuel (or a proportion of the fuel) should be injected in the compression stroke and transported near to the spark plug to form a flammable mixture, which could be ignited by the discharge (as shown in Figure 2-2 b). Thus, even the global air-fuel ratio in the combustion chamber is leaner than the ignitable limit; the discharge can ignite the mixture due to the relatively rich region near the spark plug. Ideally, for the stratified operation, a GDI engine should operate with the throttle fully open. The load of the engine is solely controlled by the amount of fuel injected.



(a) Homogeneous operation (b) Stratified-charge operation

Figure 2-2: Operating modes in gasoline engines (Celik, 2010)

2.1.3 The Direct-Injection Spark-Ignition (DISI) Combustion System

In order to achieve stratified operation in the engine, three types of combustion concept were proposed and designed: the wall-guided, the air-guided and the spray-guided combustion systems (Figure 2-3).

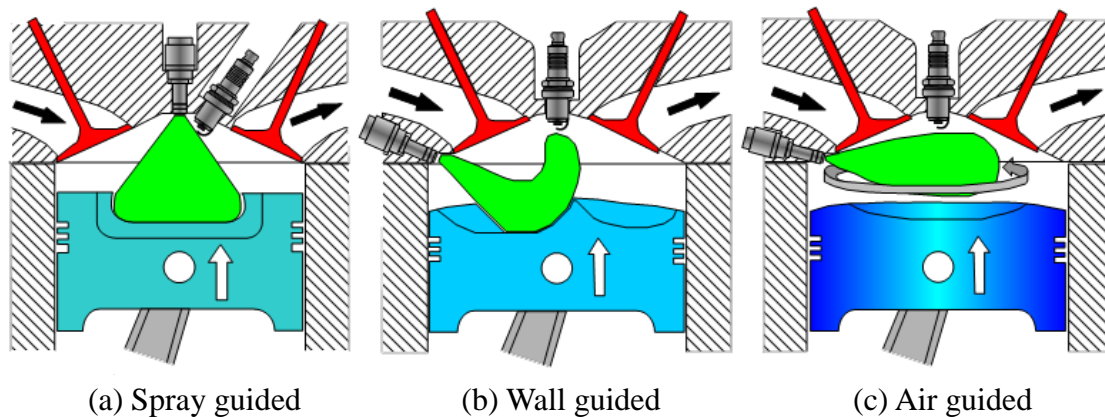


Figure 2-3: The direct-injection spark-ignition combustion systems(Celik, 2010)

The first generation stratified operation engines mainly employed the wall-guided combustion concept. As shown in Figure 2-3 b, this kind of engine has a specially designed piston crown bowl which acts as the guiding “wall”. The injector is placed on the side of the engine opposite to the wall. After the injection, the fuel is transported to the spark plug by the guidance of the wall. The flow in the engine usually supports the transportation of the mixture towards the spark plug. The initial idea of the first generation stratified charge engine is to create a stratified mixture in the combustion chamber so that the fuel economy of the engine could be increased. However, it suffers from its problems. The first problem is related to its design features: the direct contact of the spray jet and the piston leads to a high level of deposit on the piston and unburned hydrocarbons in the exhaust gas. Furthermore, the

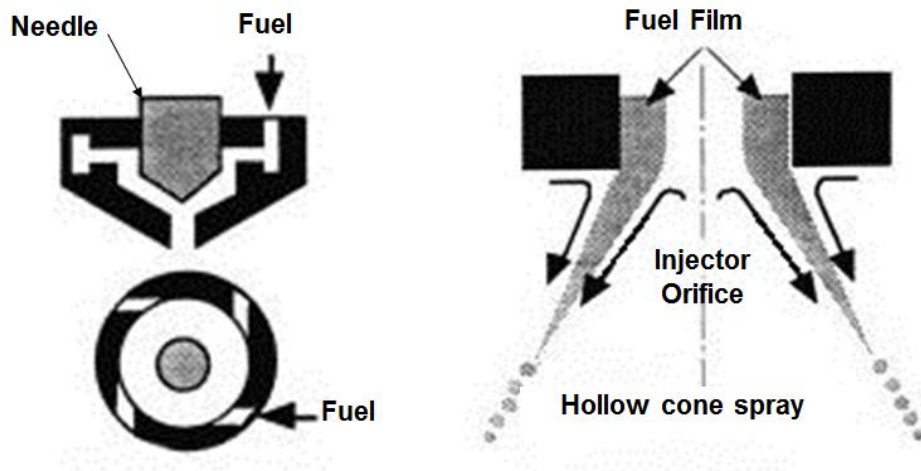
coordination of the ignition timing and the spark timing along a wide range of engine operating conditions is very difficult, because the transportation of the fuel is highly dependent on the in-cylinder flow and the flow intensity and pattern varied with the change of operating conditions.

The air-guided combustion system (shown in Figure 2-3 c) is a different type of first generation gasoline direct injection system. Compared with the wall-guided combustion system, the air-guided system utilizes charge movement to mix the fuel and the air; which avoids contact of the spray jet and the piston crown. This design eliminates the fuel deposit on the piston. However, in order to achieve the specific charge movement needed for transporting the mixture to the spark plug, the volumetric efficiency will be reduced to create the swirl and tumble required; therefore, the performance is affected.

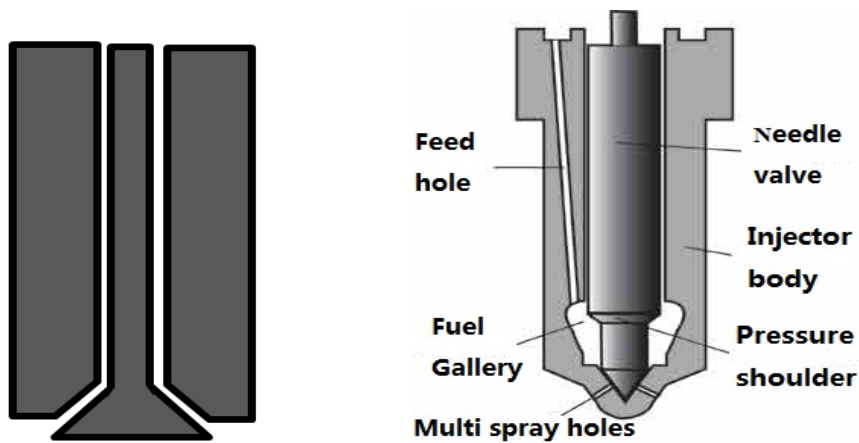
The later developed second generation combustion systems solved the previous problems on the first generation combustion systems. As shown in Figure 2-3 a, the configuration of the spray-guided combustion is significantly different from the wall-guided and air-guided combustion system: its injector is placed in the middle of the pentroof chamber rather than on one side of the cylinder. This feature ensures that when the spark plug discharges, an ignitable mixture could be predictably prepared around the spark plug across a wide engine speed/load range, because the transportation of the fuel is mainly reliant on the spray itself. Thus, research should be carried out in order to figure out the spray pattern of this type of GDI injector under different back pressure and flow conditions.

2.1.4 Types of GDI Injectors

The fuel injector is a very important component for the GDI engine in that it should be able to realize both homogenous charge combustion and stratified charge combustion in the engine cylinder. For the homogeneous charge operation, a well-atomized and evenly distributed fuel spray is needed at low in-cylinder pressure under early injection strategy. Whereas for the stratified charge operation, a well-atomized, compact and repeatable fuel spray is needed at pressurized in-cylinder pressure under late injection strategy. Fast mixture formation and controlled stratification should be achieved under various engine conditions. In order to fulfill these requirements, three kinds of GDI injectors are designed, as shown in Figure 2-4.



(a) Swirl injector



(b) outward-opening injector

(c) multi-hole injector

Figure 2-4 : Three kinds of GDI injectors (Zhao, 2009c)

The swirl injector, as shown in Figure 2-4 a, is designed for the first generation wall-guided combustion system. Its features contain an inwardly opening pintle and a single exit orifice. When the pintle moves and opens, the fuel comes out from the orifice; then a hollow-cone spray is formed and spreads quickly. However, the spray pattern of the swirl injector is significantly affected by the injection pressure, the back pressure and the injector temperature. Furthermore, during the late injection of the stratified charge operation, the hollow-cone spray will collapse due to the elevated

ambient density. A narrow spray with an increased penetration will occur. Thus, it is quite difficult to optimize the stratified charge operation over a wide range of operating conditions due to the changing spray pattern.

The solenoid-actuated multi-hole injector and the piezo-electrically actuated outward-opening injector, as shown in Figure 2-4, are developed for the GDI engine, in order to attain the spray-guided stratified charged combustion in the cylinder at part load and improve the engine performance at full load. The outward-opening injector possesses several advantages. Firstly, the blocking of the injector nozzle by the accumulated deposit can be avoided due to the movement of the outward opening pintle. Secondly, the liquid sheet of the spray can be controlled by the pintle stroke. This means that the spray angle, spray penetration and the droplet size can be controlled to some extent. Thirdly, the small opening and closing time of the piezo-electric actuation allows a much shorter opening period. Moreover, more fuel can be injected at full pintle lift. In summary, the piezo-electrically actuated outward-opening injector is capable of providing repeatable actuation dynamics, large fuel flow rate and multiple injections at one cycle, which are favorable for the development of the GDI engines. In principle, the solenoid-actuated multi-hole injector can produce any spatial fuel distribution pattern by varying the number of the holes, the angles of the spray jet and the offset from the injector axis. However, due to the requirement of fuel atomization, a relatively high injection pressure (e.g. 150 bar) is need. Furthermore, deposit can accumulate on the injector tip and blocks the small holes of the injector.

2.1.5 Engine-out Emissions

The most harmful and worrying emissions exhausted from vehicle engines are carbon monoxide (CO), unburned hydrocarbons (HC), nitrogen oxides (NO_x) and particulate matter (PM). Legislations have been put into place worldwide to limit the amount of these emissions. Emissions of CO, HC and NO_x are determined mainly by the status of the engine combustion. A combustion of rich mixture is usually the cause of CO concentration because there will be incomplete combustion; due to lack of oxygen, carbon atoms are oxidized to CO rather than CO₂. For lean mixtures, CO could also be produced due to dissociation and incomplete combustion. In this case, the concentration of CO would increase with the decrease of the combustion temperature. Unburned hydrocarbons include unburned fuel, intermediate product resulting from incomplete combustion, lubricant oil and its dissociated and oxidized components. These emissions come from flame quenching, crevices effect and oil film. The formation of NO_x is due to the reaction between nitrogen and oxygen under high temperature. The reaction could be explained by the Zeldovich mechanism (Stone, 2012a). Two factors are required for the generation of NO_x: the presence of oxygen and a high combustion temperature. The concentration of NO_x would be highest for the combustion of a slightly rich mixture, due to high temperature and a relatively high concentration of oxygen. There are three sources for PM emissions: sulfates, lead and organic particulates (including soot). The sulfur content in the fuel could be oxidized to SO₂ during the combustion and again be oxidized by the exhaust catalyst

to SO₃; which could then further combine with water at ambient temperatures to form a sulfuric acid aerosol. The amounts of sulfate emissions depend on the sulfur content in the fuel. The fuel lead content generates lead compounds and it damages the three way catalyst. Thus, nowadays unleaded gasoline is used. The soot emissions result from the combustion of a rich mixture; such as the rich combustion of a SI engine and the combustion of the rich zone in a CI engine. Usually, the soot emissions of CI engines are much higher than SI engines. Overall, the emissions' level of a GDI engine is determined by the combined effect of the mixture formation and the operational parameters' both of which are highly relative to this research.

2.1.6 Advanced GDI Engine Technologies

Throughout the history of the internal combustion engine (ICE), the main efforts of automotive research have been placed on reducing fuel consumption and the pollutant emissions. The gasoline engine has played an important role in achieving these goals. In particular, the developments on the GDI engine's technologies offer many solutions to the future possibilities of the internal combustion engine. The "downsizing" concept, which utilizes a supercharger or turbocharger so that a smaller displacement engine can generate power comparable to a bigger displacement naturally aspirated engine, reduces the throttle loss and forces the engine to operate at a high efficiency range on the engine map. This concept can largely reduce the fuel consumption and in the meantime does not deteriorate the emissions. An engine with exhaust gas recirculation (EGR) can largely reduce the NO_x emissions. A GDI engine with auto

ignition combustion (HCCI or CAI) can achieve fuel economy and a good emissions' level at the same time, due to its fast burn and low combustion temperature. This technology might be used in the low to medium load range in order to save fuel. At high load, another combustion mode would be used. The lean boost GDI engine might be another possibility, due to the future legislation on CO₂. With the second generation GDI injector, there would be repeatable and controllable spray in the combustion chamber. This technology could further reduce the fuel consumption compared to the "downsizing" concept. It also improves the knocking limit and the transient response.

2.2 Bio-fuels for Spark Ignition Engines

The use of bio-fuels in spark ignition engines brings benefits on balancing CO₂ emissions and improving fuel security. It can also have environmental and economic benefits. Currently, ethanol is the only large scale used bio-fuel because of its mature production method and favorable performance and emissions from the engine. The high tolerance of ethanol towards knock can improve the thermal efficiency and torque output (Nakama, 2008). In 2007, 80% of the world's bio-fuel used was ethanol (OECD, 2008). However, ethanol fuelled engines suffer from bad cold starts and high fuel consumption (Chen, 2011). Moreover, an argument exists regarding to the fact that the consumption of grain in the production process of ethanol would increase food prices and thus create food shortages, particularly for the poor (Russell, 1980 and Kenneth, 2007).

The use of methanol is another choice for bio-fuel. Research shows that low methanol blends only require minor engine modifications (Kowalewicz, 1993) but still produce a similar performance compared to gasoline (Liu, 2007 and Wei, 2008). Nevertheless, similarly to ethanol, the low energy density of methanol impedes its use in high blends.

The two gasoline alternatives 2-methylfuran (known as MF) and 2,5-dimethylfuran (known as DMF) are heterocyclic compound derivatives of furan. Their new mass production method was found by several research teams independently (Roman, 2007, Luque, 2008 and Zhao, 2007). It is this method which makes them possible for future commercial use. Using two main oxygen removal steps, fructose can be converted into MF and DMF: in the first step, three oxygen atoms are removed through dehydration in order to produce 5-hydroxymethylfurfural (known as HMF); in the second step, two oxygen atoms are further removed from HMF through dehydration. In this process, MF and DMF are produced. Due to the fact that fructose is abundant in bio-mass, MF and DMF can be considered as sustainable bio-fuels.

The properties of MF and DMF are what made them attractive. The research octane number (RON) of MF and DMF are 103 and 101, respectively. The high octane numbers means that the two fuels have good knock resistance and thus could be used at higher compression ratio in order to achieve higher combustion efficiency. The latent heat of vaporization of MF (358.4kJ/kg) and DMF (332kJ/kg) are similar to gasoline (373kJ/kg). Moreover, the energy densities of MF (28.5MJ/l) and DMF (29.3 MJ/l) are very high and quite close to that of gasoline (31.9MJ/l). Compared to

ethanol (energy density 23.43 MJ/l), the widely used bio-fuel in the market, MF and DMF contains more energy.

DMF is a promising biofuel candidate which attracted the attention of the researchers earlier. The author's group is the one of the first groups that studied the performance of MF and DMF as an alternative fuels in the engine. Zhong et al. (2010) investigate the engine performance of DMF in a single cylinder DISI engine compared with gasoline and ethanol. They concluded that the engine performance and emissions of DMF were very similar to those of gasoline. Tian et al. (2010a) studied spray characteristics of DMF using PDPA and their work showed that the spray characteristics of DMF were very much similar to that of gasoline compared with ethanol. Daniel et al. (2011) compared the engine performance and emissions of DMF, gasoline and ethanol under fuel-specific ignition timing and gasoline maximum break torque (MBT) ignition timing in a direct injection spark ignition (DISI) single cylinder engine. Wu et al. (2011) studied the dual-injection strategy on a single cylinder DISI engine fueled with gasoline blended with DMF, ethanol. These engine studies suggest that DMF produced competitive combustion and emissions qualities compared to gasoline. Rothamer et al. (2012) investigated the knocking propensity of DMF-gasoline blends compared to ethanol-gasoline blends, which indicated that the blend fuel with 10% DMF provided the best performance. Zhang et al. (2013) studied the combustion and emissions of DMF addition on a diesel engine. It was found that DMF addition has little effects on CO and THC emissions, whereas 40% DMF addition could reduce soot emissions to nearly zero.

As for the study of MF, only a few publications are available. Wang et al. (2013) examined the engine performance, PM, regulated emissions, and unregulated emissions of MF, DMF, gasoline and ethanol. It was found that even though MF and DMF have similar chemical structures, the combustion characteristics of them were significantly different. MF has higher indicated thermal efficiency compared to DMF and gasoline due to its fast burning rate and knock suppression ability. The impact of MF on mixture formation and combustion was examined in a DISI Engine by Thewes (Thewes, 2011). They found that the initial evaporation of 2-methylfuran is quicker than ethanol due to the low boiling temperature and high vapor pressure. The NO_x emission of MF combustion is high due to its high adiabatic flame temperature. The auto-ignition characteristics of MF in a SI engine were studied by Ohtomo (Ohtomo, 2011). In this study, it was proved that the auto-ignition suppression of MF was almost equal to that of ethanol and larger than toluene although the auto-ignition delay of pure MF was shorter than that of ethanol and toluene. A detailed chemical kinetic modeling study of MF oxidation was established and compared to the experimental results by Somers (Somers, 2013). The model was proved capable of precisely reproducing the experimental results as a function of both equivalence ratio and temperature.

Knowledge of the spray and flame propagation are essential for the future commercialization of any new fuel. Until now, no detailed investigation on the spray and flame propagation of these furan derivatives has been conducted. Thus it is necessary for this research to be carried out.

2.3 Spray Characteristic of the GDI Injector

As mentioned previously, for a GDI engine the spray-guided combustion system is favoured for future GDI engine development; due to its advantages in the control of the fuel distribution and reduction of the exhaust emissions. Two types of injectors are designed for the spray-guided combustion system: the multi-hole injector and the outward-opening injector. In this thesis, the research is focused on the spray of the furan bio-fuels using a multi-hole injector. The spray characteristics, including the macroscopic and microscopic characteristics which can largely affect the performance and emissions of an engine, are discussed in this section.

2.3.1 Spray Structure and Break Up

A typical spray structure is shown in Figure 2-5, which illustrates the important parameters that are used to describe and evaluate a spray. These parameters include the spray cone angle, the break-up length, the spray penetration and the droplet size distribution. After coming out through the nozzle hole (this is usually accomplished by lifting the needle valve for the case of the multi-hole injector), the fuel starts to interact with the ambient air. It pushes air away from its path and in the meantime entrains the surrounding air into the spray and becomes turbulent. The length of the continuous liquid column is called the break-up length (Hiroyasu, 1990). Then, the liquid fuel starts to disintegrate into droplets or detached columns. The spray becomes

wider as more air is entrained and more fuel is atomized into small droplets. The spray tip velocity decreases in this process and the evaporation of the fuel continues throughout the whole process of the injection and even after the injection.

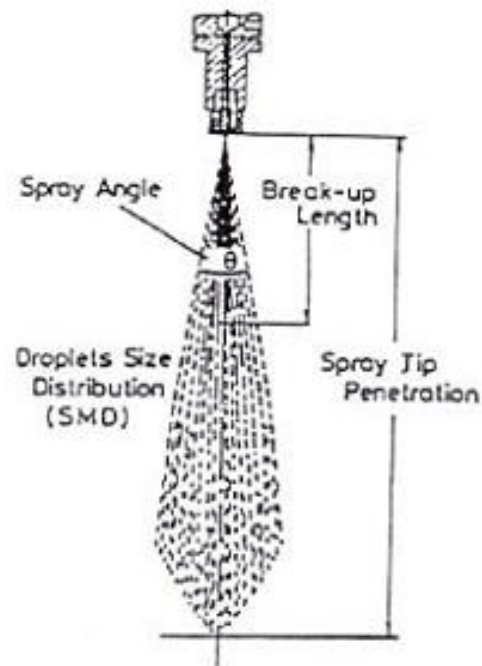


Figure 2-5: Spray structure (Hiroyasu, 1990)

The break-up or disintegration of a spray jet is of vital importance to the further development of the spray. The break-up mechanisms can be divided into five regimes according to the jet velocities (Hiroyasu, 1985). Figure 2-6 shows the jet stability curve which indicating the change of the break-up length with the increase of the jet velocity. Five regimes can be found from this figure: A: the dripping regime, B: Rayleigh regime, C: the first wind-induced regime, D: second wind-induced regime, E: atomization regime.

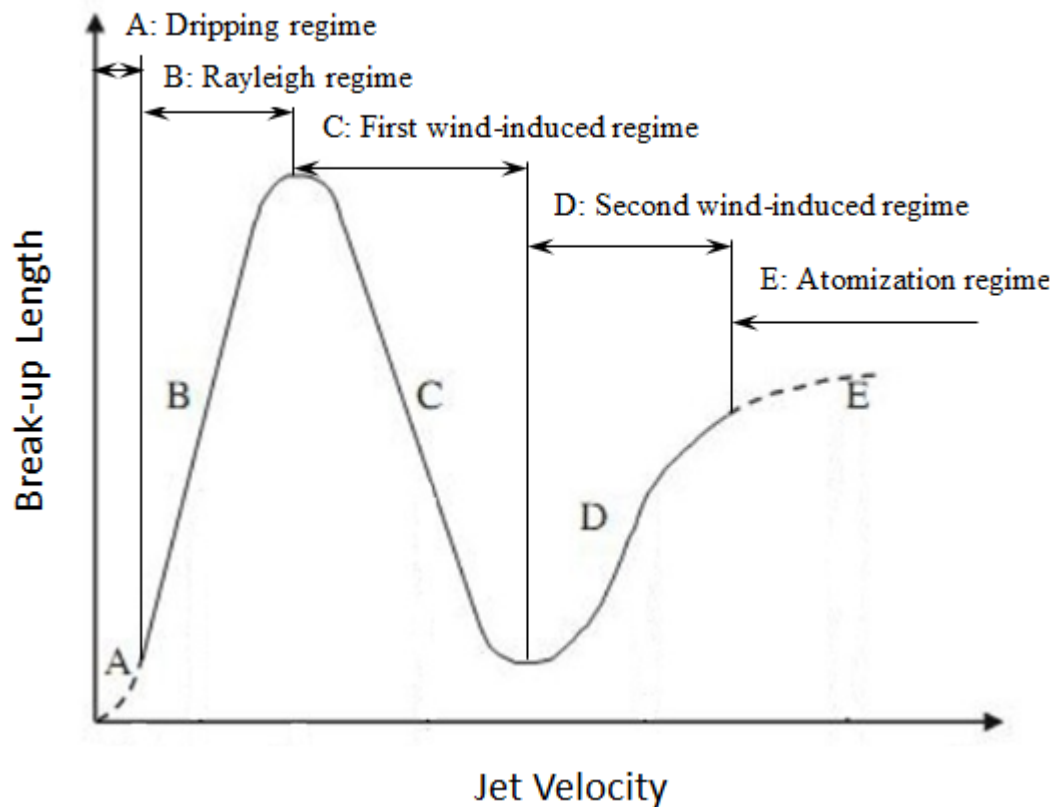


Figure 2-6: Jet stability curve (Hiroyasu, 1985)

When the jet velocity is very low, a continuous liquid column cannot form and fuel can only be emitted from the nozzle of the injector. Thus this regime is called the dripping regime. The next regime is called the Rayleigh regime; in which the break-up is caused by the axis-symmetric instabilities and a droplet is produced when the perturbation becomes equal to the jet radius. As the jet velocity increases, the liquid column enters a regime called the first wind induced regime. In this regime, the surface wave perturbation is still quite axis-symmetric but begins to be assisted by the ambient air; thus the droplet diameter is slightly smaller than in the Rayleigh regime. The next regime is called the second wind-induced regime; where the disintegration of the jet is caused by the radial component of velocity resulting from the turbulent flow in the injector nozzle. The radial velocity can overcome surface tension and

assist the break-up of the jet. The characteristic length of the initial surface perturbations produced by the turbulent fluctuations is proportional to the integral length scale of turbulence. Gas is the driving agent of the turbulent fluctuations' unstable growth because of the shear force between gas and liquid. The perturbation is restricted by surface tension forces and liquid viscous forces. In the atomization regime, the spray is completely atomized at the nozzle exit (Lefebvre, 1989) and the onset of the break-up is strongly influenced by the liquid flow inside the nozzle and the presence of turbulence. The resulting droplet sizes in this regime are much smaller than in the other regimes and the gasoline engine mixture formation can be represented solely by the atomization process (Basshuysen, 2009).

Two non-dimensional numbers, the Weber number (We) and the Reynolds number (Re), have been created as the characteristic numbers for the break-up of a liquid (Lefebvre, 1989). These two non-dimensional numbers are used to estimate the effect of the external aerodynamic force and the inertial force of the liquid on the liquid break-up.

The Weber number indicates the ratio of the external disruptive aerodynamic force to the surface tension force (Lefebvre, 1989). It can be expressed by:

$$We = \frac{\rho D u_d^2}{\sigma} \quad (2-1)$$

Where:

ρ is the liquid density (unit: kg/m^3); D is the droplet diameter (unit: m); u_d is the droplet relative velocity (unit: m/s) and σ is the surface tension of the liquid (unit: N/m).

The Reynolds number represents the ratio of inertial force to viscous force of the liquid (Lefebvre, 1989). The equation for it is:

$$Re = \frac{\rho u_d L}{\mu} \quad (2-2)$$

Where: ρ is the liquid density (unit: kg/m^3); μ is the dynamic viscosity (unit: $\text{kg/m}^*\text{s}$); u_d is the droplet velocity (unit: m/s) and L is the nozzle diameter (unit: m).

Except these two non-dimensional numbers, the Ohnesorge number (Oh) is also commonly used to define the ratio of internal viscous forces to surface tension forces.

$$Oh = \frac{\sqrt{We}}{Re} \quad (2-3)$$

2.3.2 Spray Tip Penetration and Spray Angle

Both the spray tip penetration and the spray angle have significant influence on the engine performance and emissions. The influence of the spray tip penetration on combustion is obvious: if the penetration length is too long, the spray jet would easily impinge on the piston top or the cylinder wall causing an increase of the HC emissions and a decrease of the combustion efficiency; if the penetration length is too short, then the fuel cannot be adequately delivered to the far end of the combustion chamber which leads to improper mixing and therefore would increase the emissions. The influence of the spray angle on the mixture preparation is different: better mixing could be achieved with larger spray angle. The spray angle affects the axial and radial fuel distribution for the GDI engine.

Many studies on spray penetration have been carried out and correlations based on

experimental data can be found in literature (Hiroyasu, 1985, Smallwood, 2000, Klein-Douwel, 2009, Heywood, 1988 and Lefebvre, 1989). The liquid spray penetration is affected by several variables (Smallwood, 2000): the nozzle diameter; the nozzle length/diameter ratio; the injection pressure; the ambient gas density; the ambient gas temperature; the fuel viscosity; the fuel surface tension and the fuel temperature. In general, a fuel with high viscosity and surface tension under high injection pressure and low ambient gas density tends to have longer spray penetration. The spray angle definition is not unanimous for all researchers; some use isosceles triangles which have the same area and height as the entire or half of the spray to define the spray angle (Kang, 2003); others define the spray angle by connecting the spray width at a certain axial position to the starting point of the spray (Lefebvre, 1989, Farrel, 1996, Dodge, 1992). Usually, a fit line is used on the spray contour to illustrate the spray angle (Pastor, 2001, Delacourt, 2005). A number of parameters affect the spray angle. The spray angle increases with gas/liquid density ratio and decreases with the nozzle length/diameter ratio (Reitz, 1979). The spray angle increases with a decreasing fuel viscosity and the jet divergence begins at the nozzle exit if the fuel viscosity is below a certain level (Heywood, 1988).

2.3.3 Droplet Size

After break-up, the liquid column of a spray disintegrates into countless small droplets. The droplet size and size distribution largely influence the evaporation of the fuel in the engine cylinder and further on influence the combustion and emissions.

The studies of the droplet mean diameter and the droplet size distribution reveal the spray quality and are of great importance to the analysis of the fuel properties and the injection system. In order to evaluate and describe the droplet size in the automotive field, the Sauter mean diameter (SMD) is often used and the definition is:

$$D_{32} = \frac{\sum N_i D_i^3}{\sum N_i D_i^2} \quad (2-3)$$

Where N_i is the amount of droplets in class i and D_i is the diameter of class i . In this study, Sauter mean diameter (SMD) is used for all the analysis on droplet sizes of the fuels.

2.4 Laminar Premixed Flame and Turbulent Premixed Flame

The laminar premixed flame and the turbulent premixed flame have a large number of applications in commercial and industrial devices. Examples of laminar premixed flame applications include gas ranges, heating appliances and Bunsen burners and the most widely used application for the turbulent premixed flame is the spark ignition engine. In this chapter, the characteristics and related theories of the laminar premixed flame and the turbulent premixed flame will be discussed. The effect of the equivalence ratio, temperature, initial pressure and fuel property on the laminar flame will be illustrated. The dependence of the turbulent flame's velocity on the flow and the mixture properties will be examined.

2.4.1 Laminar Flame Propagation

The laminar premixed flame and its theories are important because it is widely used in many applications; even more importantly, it is a prerequisite to understanding the turbulent flame. The most essential characteristics of a laminar premixed flame can be represented by its laminar flame speed and the flame thickness. The laminar flame speed and the flame thickness are influenced by a number of factors including the equivalence ratio, the initial temperature, the initial pressure and the fuel properties.

The dependence of the laminar flame speed (S_L) on the temperature and pressure for methanol, isooctane, indolene and air mixtures over a range of temperatures and pressures are experimentally determined by Metghalchi and Keck (Metghalchi, 1982):

$$S_L = S_{L,ref} \left(\frac{T_u}{T_{u,ref}} \right)^\gamma \left(\frac{p}{p_{ref}} \right)^\beta (1 - 2.1 Y_{dil}) \quad (2-4)$$

Where the subscript ref refers to reference conditions defined by $T_{u,ref}=298K$; $p_{ref}=1atm$; T_u is the initial temperature; p is the initial pressure and Y_{dil} is the mass fraction of the diluent. The temperature and pressure exponents, γ and β , are functions of the equivalence ratio (Φ):

$$\begin{aligned} \gamma &= 2.18 - 0.8(\Phi - 1) \\ \beta &= -0.16 + 0.22(\Phi - 1) \end{aligned} \quad (2-5)$$

The relationship between the laminar flame speed (S_L) and the flame thickness (δ_l) can be expressed using (Bradley, 1998):

$$\delta_l = 2\alpha / S_L \quad (2-6)$$

in which α is the thermal diffusivity.

It can be seen that the laminar flame speed and the related flame thickness have strong temperature dependence and relatively weak pressure dependence. These dependences expressed by the equations can be used to estimate the laminar flame speed and the flame thickness of various fuel-air mixtures at different temperatures and pressures.

Except for very rich mixtures, the influence of the equivalence ratio on the laminar flame speed (S_L) is actually the influence of the equivalence ratio on the flame temperature (Turns, 2011a). Therefore, the laminar flame speed will increase from lean mixtures to slightly rich mixtures and then decrease with the increase of the equivalence ratio. From equation 2-6, it can be seen that the flame thickness is proportional to $1/S_L$. Thus, an inverse trend for the flame thickness, which it minimizes at slightly rich conditions, can be expected and observed because the laminar flame speed peaks at slightly rich conditions.

The property of a fuel affects the laminar flame speed and the flame thickness as well. The work of Barnett et al. (1957) studied and compared the flame velocities of C2-C6 alkanes (single bonds), alkenes (double bonds) and alkynes (triple bonds) using the laminar flame speed of propane as the reference. It was found that the trend of the laminar flame speeds of the C3-C6 hydrocarbons roughly followed a function of the flame temperature. The laminar flame speeds of the C2 group, ethylene (C₂H₄) and acetylene (C₂H₂), were higher than the C3-C6 group. The case of pure hydrogen is quite different: its laminar flame speed was several times higher than the hydrocarbon fuels. For instance, its laminar flame speed was 210 cm/s at an equivalence ratio of

1.0 and initial pressure of 0.1 MPa whereas under the same conditions the laminar flame speeds of propane and methane were 44 cm/s and 40 cm/s, respectively (Turns, 2011c).

2.4.2 Turbulent Flame Propagation in Spark Ignition Engines

The combustion process in a homogeneously charged SI engine is usually divided into three periods (Stone, 2012b):

First period: the initial burning period - after discharge of the spark plug, a small flame kernel is initiated. Before the kernel is big enough to be affected by the turbulence, the flame is considered as laminar burning. The first few percent of the mass fraction burned corresponds to this period.

Second period: the turbulent period - in this period, the volume of the flame is comparatively large. With small unburned fractions entrained into the flame front, the mixture burns fast.

Third period: the final burning period - this period is also called the “termination period” or the “burn-up period”. Due to the slowdown of the fluid motion and the reduced temperature in the cylinder, the residual mixture in the cylinder burns out slowly.

Among these three periods, the turbulent burning period is of great importance because it is the main combustion period which largely affects the performance and emissions of the engine. However, compared with laminar flame propagation, the turbulent flame propagation in a spark ignition engine is more complex; not only the

mixture properties, but also the flow in the engine affects the turbulent flame speed.

The definition of turbulent flame by Stephen R Turns is (Turns, 2011d):

“For an observer travelling with the flame, we can define a turbulent flame speed, S_t , as the velocity at which unburned mixture enters the flame zone in a direction normal to the flame.”

The turbulent flame speed (or global consumption speed) for all turbulent flames is commonly expressed as follows (Turns, 2011d):

$$S_t = \frac{\dot{m}}{\bar{A}\rho_u} \quad (2-7)$$

where S_t is the turbulent flame speed (unit: m/s); \dot{m} is the reactant flow rate (unit: kg/s); ρ_u is the unburned gas density (unit: kg/m³) and \bar{A} is the time-smoothed flame area (unit: m²). In a real situation, the calculation of a turbulent flame speed is challenging due to the difficulty in determining the flame area, which usually has a complex shape and thus causes ambiguity.

Although the definition of the turbulent flame speed is expressed by equation 2-7, a large number of phenomenological combustion models have been developed by the researchers in order to predict and describe the turbulent combustion process especially in the SI engine. The turbulent combustion model developed by Tabaczynski et al. (1977) gives a prediction of turbulent combustion. His combustion model considers the influence of the turbulence in the cylinder and the laminar flame

speed of the fuel. It is assumed that the flame propagates with an entrainment process and within the entrainment region burning happens at a rate controlled by turbulence parameters. The mass entrainment rate is described by:

$$\frac{dm_e}{dt} = \rho_u A_f (\mu + S_L) \quad (2-8)$$

where m_e is the mass entrained into the flame front; ρ_u is the unburned charge density (unit: kg/m³); A_f is the flame front area (unit: m²); μ is the turbulence intensity (unit: m/s); S_L is the laminar flame speed (unit: m/s).

From this equation, it can be seen that the turbulent flame speed in an engine cylinder is largely affected by the turbulence intensity and the local laminar flame speed. As discussed in section 2.4.1, the laminar flame speed is influenced by the local equivalence ratio, the local temperature and the local pressure and the fuel properties. The turbulence intensity is assumed to be proportional to the mean piston speed. Therefore, the combined effects of the in-cylinder conditions and the property of the fuel determine the turbulent flame speed.

2.5 Summary

In summary, this chapter discussed the development of the GDI engine including a short history; mixture formation type of GDI compared with a Carburetter and PFI; the operating modes and the combustion concepts of the GDI engine. Then the emission legislations and the GDI engine technologies were presented.

The second part introduced the background knowledge of leading bio-fuels on the market, including the use of ethanol and methanol. The properties of the furan

derivatives, DMF and MF, were presented and the related research of these bio-fuels is introduced.

The third part of this literature review discussed relevant knowledge about the spray of the GDI injectors and the flame propagation in the vessel and in the GDI engine. The structure and the break-up of a spray were reviewed. The related parameters which could be used to evaluate the spray, including the spray tip penetration, spray cone angle, droplet size and droplet velocities, were discussed. The laminar flame propagation and the turbulent flame propagation were then discussed. The parameters which affect the laminar flame propagation were summarized and considered. The turbulent flame propagation model developed by Tabaczynski was presented and the links between the laminar flame and the turbulent flame were discussed.

Through the literature, the main motivation of this thesis, which was to investigate the spray and combustion of the furan alternatives, was introduced and explained.

Chapter 3

Experimental Set up and Techniques

The aim of this chapter is to present the experiment facilities and the related data acquisition techniques used in the study. The facilities included the constant volume vessel, the fuel injection system, the high speed Phantom camera, the intensifier, the Schlieren system, the optical engine, the PLIF laser, and the PDPA system.

3.1 Spray Image Acquisition System

Using high speed imaging, the macroscopic spray characteristics of the bio-fuels under various back pressures, injection pressures and vessel temperatures were evaluated. The spray images of the bio-fuels were acquired by using the high speed camera and they were analysed by MATLAB code. Detailed description of the experiment system and the data analysis will be given in this part.

3.1.1 System Configuration

The experimental setup for the high speed image acquisition of the macroscopic spray is shown in Figure 3-1. The injector was installed on the top of the vessel and a 45° mirror was placed under the vessel in order to allow the camera to capture the spray images via the window in the bottom. The temperature and pressure in the vessel were controlled. The devices used in this system, including the constant volume vessel, the

camera, the fuel injection system and the temperature control system will be described in the following sections.

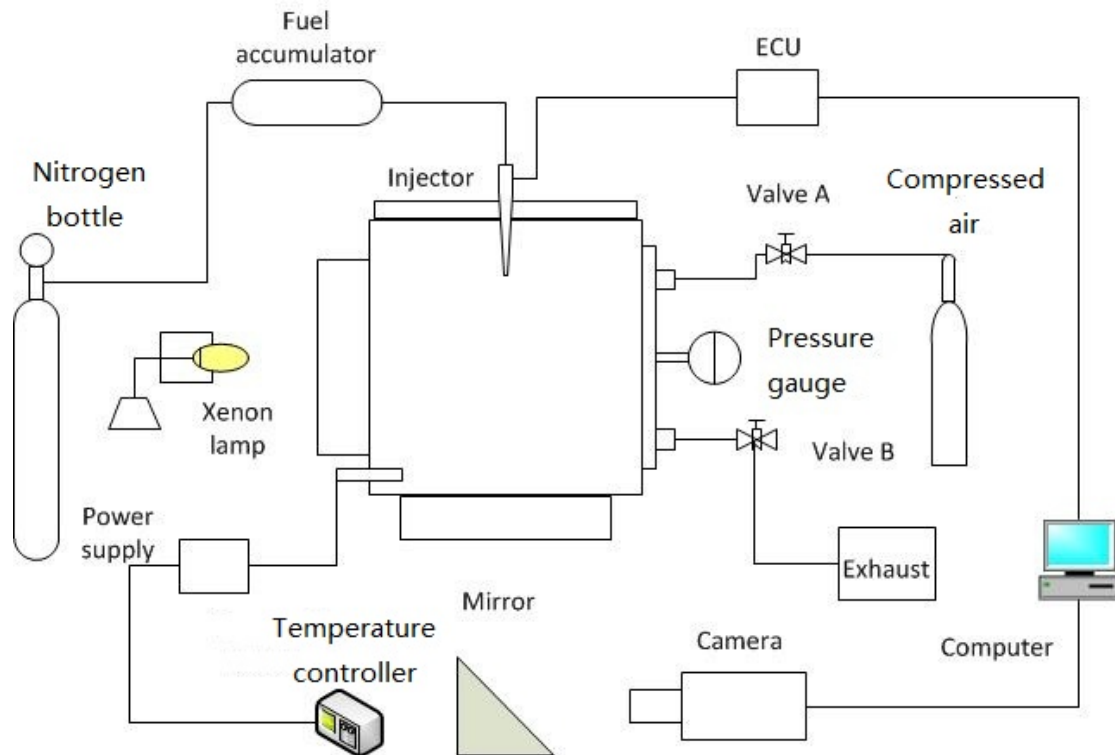


Figure 3-1: High speed image acquisition system for spray in the vessel

3.1.2 Constant Volume Vessel

Many tests in this study were carried out in a constant volume vessel (e.g. the Schlieren test, macroscopic spray test and the PDPA test). As shown in Figure 3-2, this black cubic constant volume vessel contained several optical windows which had optical access diameters of 100mm and lids which connected to tubes, solenoid valves and safety valves. The optical windows and the lids were interchangeable. So in different experiments, the setting could be changed according to the needs of each experiment. Eight heating units were placed in the eight corners of the vessel. Each of

them provided 250 watts of power and the vessel could be heated up to 120°C. A Bosch AJ133 injector was installed on the top lid of the vessel. This injector was controlled by a Bosch ECU. The safety valve, which released the pressure in the vessel when it was higher than 0.7 MPa, was placed on one of the lids. A TC-direct thermocouple was used to measure and control the temperature in the vessel. The accuracy was within 1 degree. The tubes and the solenoid valve were used to intake fresh air and exhaust the mixture inside the vessel. The solenoid valves were controlled by the TTL pulse signals.

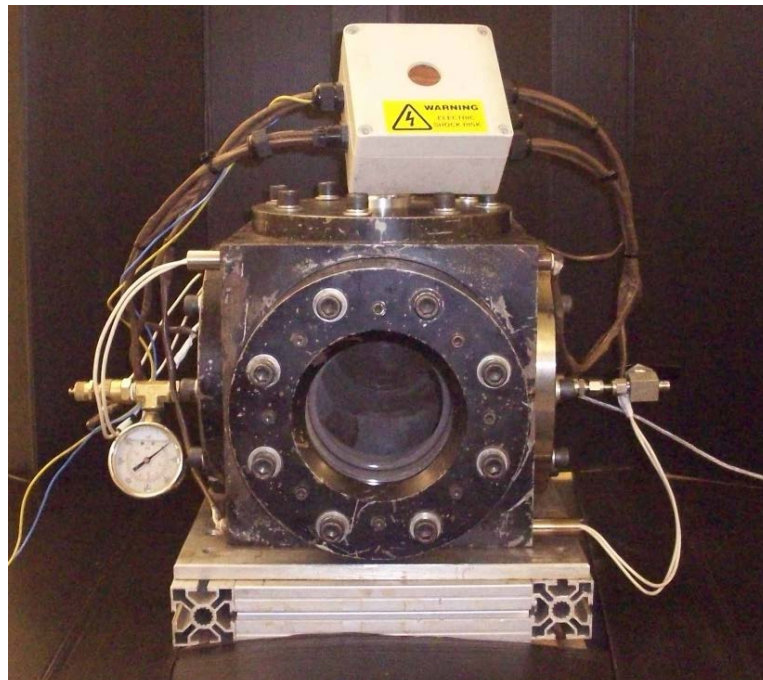


Figure 3-2: Constant volume vessel with heating units in 8 corners of the vessel

3.1.3 Fuel Injection System

In this study, the fuels were supplied by the fuel accumulator and injected by a multi-hole GDI injector. The injection amount, timing and frequency were precisely controlled by the computer through an ECU, as shown in Figure 3-1. The GDI

injector is shown in Figure 3-3. Before any test, the fuel was pumped into the fuel accumulator and then pressurized by the high pressure nitrogen bottle; the injection pressure was controlled by varying the pressure of the nitrogen gas. In the high speed imaging spray test, the injection and the camera were synchronized by the computer.



Figure 3-3: The multi-hole GDI injector

3.1.4 CCD Camera (Intensifier)

Figure 3-4 shows the Phantom V710 ultra-high speed camera and the HAMAMATSU high speed intensifier. Table 3-1 shows the specification of the camera and the intensifier. The Phantom V710 camera was used throughout this work. In the macroscopic spray characteristic study, it was used to capture the spray images. The frame rate used was 18 kHz and the resolution was 608x600. In the Schlieren test, it was used to capture the laminar flame images. The frame rate was 10 kHz and the resolution was 800x800. In the turbulent flame measurement, it was used to record the in-cylinder flame of the bio-fuels. The frame rate was also 10 kHz and the resolution was 800x800.



Figure 3-4: High speed camera coupled with the intensifier

Table 3-1: Specification of the camera and the intensifier

Phantom V710 Camera	
Resolution	Up to 1280x800
Sample rate (fps)	Up to 1,500,000
Colour expression, gradations	Monochrome 8 bit and 12 bit
Storage	16GB
HAMAMATSU Intensifier (C10880-03F)	
Maximum gated rate	10 kHz
Minimum gating time	20ns
Response time	10ns

In the spray test and the Schlieren test, there was no need to use the intensifier, because the light was relatively strong. However, for the in-cylinder flame recording and the LIF image recording, it was necessary to use the intensifier. Figure 3-5 shows the recorded images with and without the intensifier. It is obvious that the intensifier could make the weak flame light “visible” to the camera.

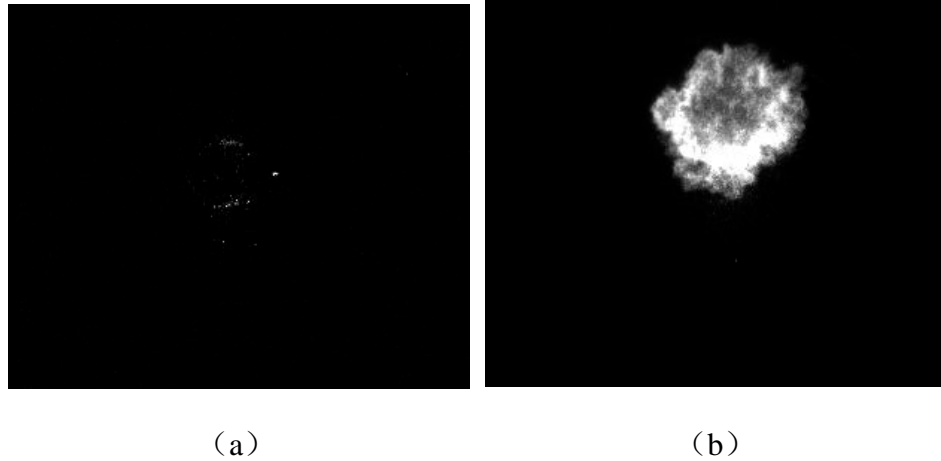


Figure 3-5: Flame image in the cylinder (a) without the intensifier (b) with the intensifier (IMEP=4.5bar, $\lambda=1$)

3.2 PDPA system

PDPA is a non-intrusive method which can be used to measure the droplet size and droplet velocity at a particular point of a spray jet. In this work, the PDPA system was used to measure the droplet size and velocities of the bio-fuel injection under different back pressures, ambient temperatures and injection pressures. A typical PDPA system is shown in Figure 3-6. It comprises a laser, transmitting optics, photon detectors and signal processors. The laser beam goes through the transmitting optics and is divided into a pair of intersected beams. Thus a fringe pattern (the measurement volume) is created. When droplets travel through the measurement volume, laser light will be scattered and the photon detectors will capture these light signals. The associated temporal and spatial information of the droplets are then analyzed by the signal processor and recorded by the computer. It should be note that Figure 3-6 is only used to describe the PDPA system working theory rather than indicating the geometry of the PDPA system used in this study. The configuration of the PDPA system used in

this study is shown in Figure 3-7 and detailed description on the droplet size and velocity measurement can be found in section 3.5.2.

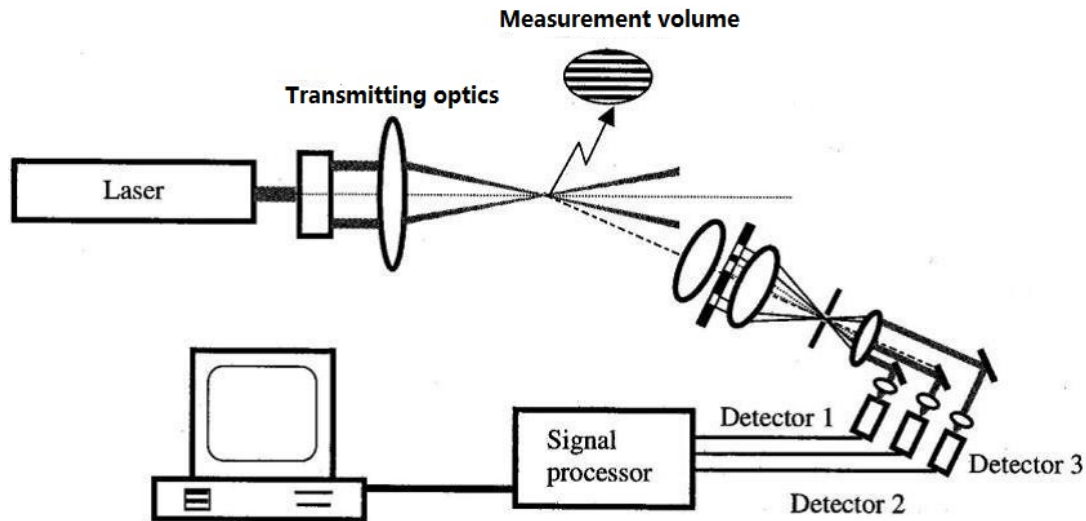


Figure 3-6: PDPA system working theory (Zhao, 2001)

3.2.1 System Introduction

The schematic of the PDPA system used in this work is shown in Figure 3-7. The entire PDPA system, including the transmitting optics and the detectors, were fixed on a 3D traverse system. The traverse system allowed the measuring point to move 3 dimensionally in the space and the accuracy was within 0.01 mm. In order to make the measurement under varied back pressures and ambient temperatures, a combustion vessel was used as the test field (described in chapter 3.1.2). The heating units installed in the 8 corners of the vessel were used to change the temperature. A compressed nitrogen bottle was connected to the vessel in order to vary the vessel pressure. The pressure in the vessel was monitored by a pressure gauge. The fuel spray was controlled by the fuel injection system described in chapter 3.1.3. The injector used was the AJ133 injector.

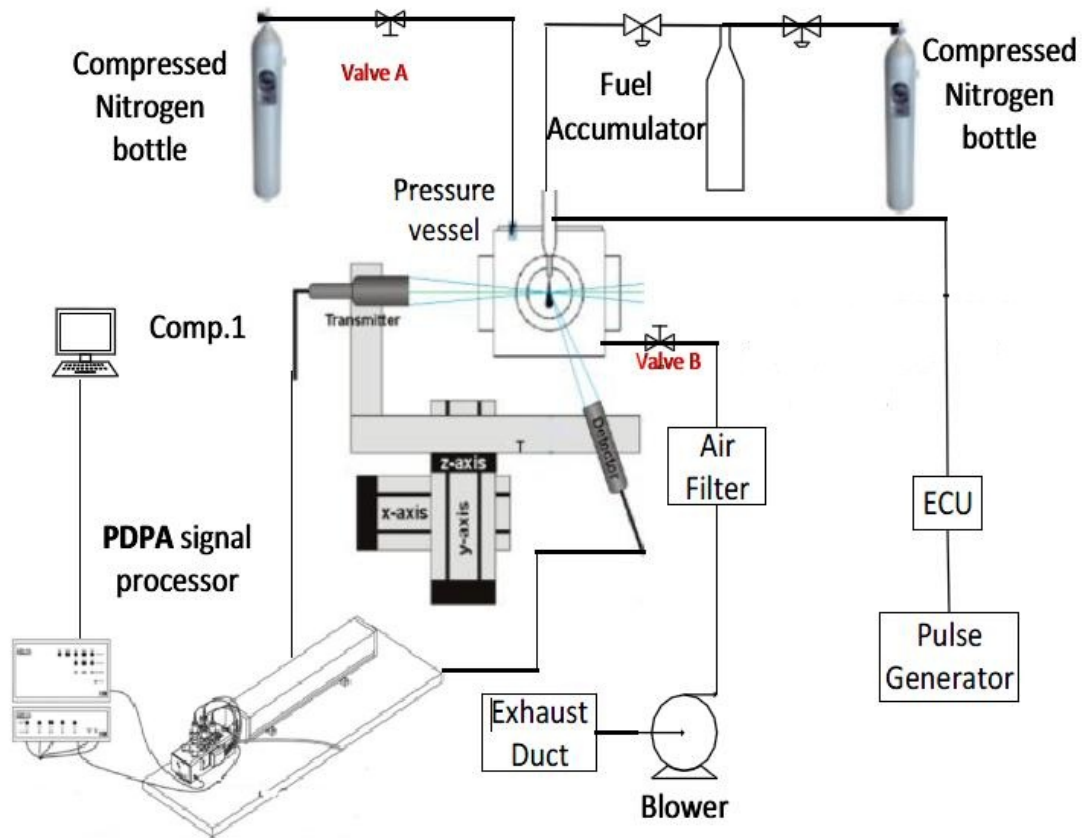


Figure 3-7: PDPA system used in this study

In the beginning of each test, the test matrix which contained spatial information of the spray jet was input into the PDPA control and processing software, called BSA flow. The measurement was taken at each point and terminated at the point when either the measuring time reached the set maximum time (usually 60s or 90s) or the recorded point reached the set maximum point (usually 50,000 points). The fuel injection, the PDPA processor and the air sweep were synchronized and controlled by the signals produced by the pulse generator. While measuring, fuel was injected into the vessel at a rate of 2 Hz for three times and then it rested for 1.5s to allow fresh nitrogen gas to enter the vessel. The fuel injection pulse width was fixed at 1ms. The BSA flow software recorded the droplet information for 5ms after every pulse. The

statistical data for both the droplet size and the droplet velocity was then analysed by the software. After the measurement was finished on all the spatial points, the data was output and the appropriate graphs were plotted.

3.3 Schlieren System

3.3.1 Schlieren System Overview

Figure 3-8 shows the sketch of the schlieren system used in this work. The constant volume vessel, which was described in Chapter 3.1, was used for this Schlieren test. In order to install the Schlieren system in a small space in the optical lab, the Z-type Schlieren setup was used. A lens and pin-hole group was coupled with a 500W xenon lamp to form the point light source. The light from the point light source was then guided to the first concave mirror by a small flat mirror. After reflecting from the concave mirror, the divergent light was converted into parallel light. The parallel light travelled through the two oppositely placed quartz windows on the vessel to form the test field. The other concave mirror was placed on the other side of the vessel to converge the parallel light into a point light again. A knife edge was used to cut the point in order to form the Schlieren graph. The high speed phantom camera, which was synchronized with the spark timing, then captured the image during the burning period at a resolution of 800x800 and a sample rate of 10 KHz.

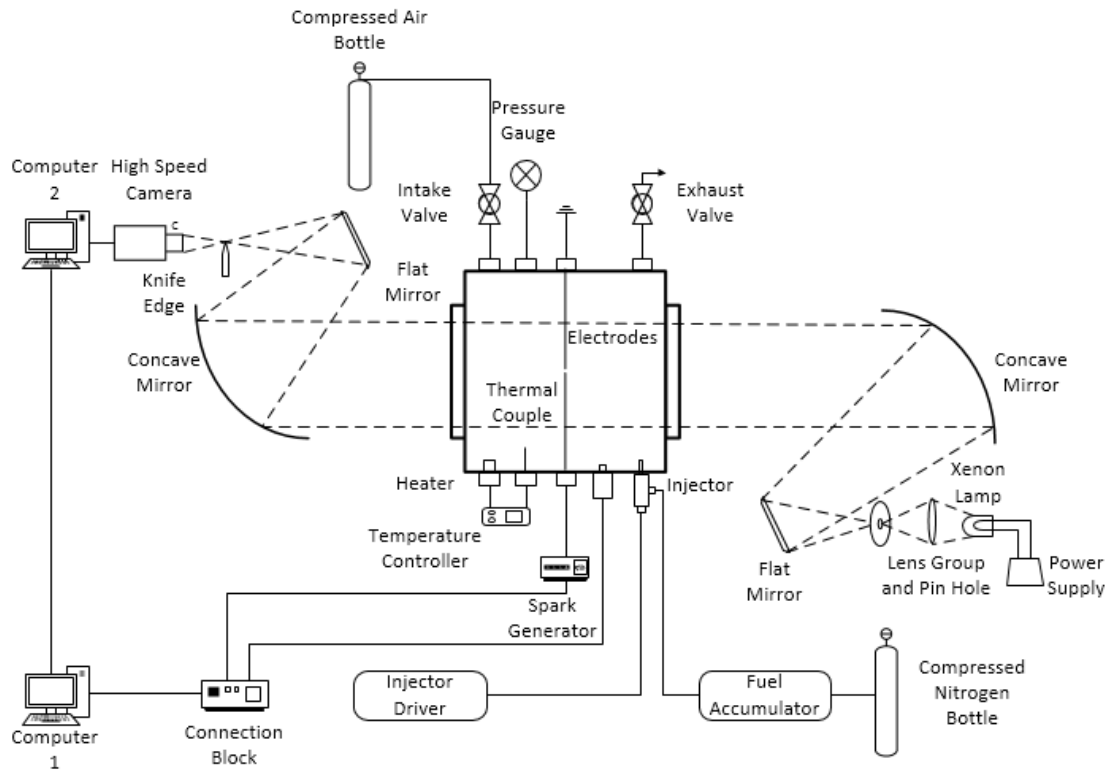


Figure 3-8: Schlieren system setup (Ma, 2013)

In the beginning of each test, both the intake and exhaust valves were opened to allow the burned mixtures to be scavenged by the compressed air. Then, the intake valve was closed whereas the exhaust valve was still open until the temperature in the vessel rose to the set temperature. After the stabilization of the temperature, all the valves were closed and thus the vessel was sealed. Then the fuel was injected via the aforementioned AJ133 injector. The equivalence ratios were precisely controlled by the amount of fuel injected into the vessel. The AJ133 injector was calibrated before the Schlieren experiment and the pre-calibrated data were used to determine the injection durations and pulses needed in order to achieve certain equivalence ratios in the vessel. After the injection, the vessel was left undisturbed for several minutes to achieve homogeneous air-fuel mixtures and a near quiescent condition. A signal was sent to start the electrode discharge and to trigger the camera recording

simultaneously. In this way, the flame propagation which was initiated by the electrode discharge was recorded by the high speed camera. After the combustion, the recorded images were transferred to the computer to be stored and the vessel was flushed with compressed air so that the test could be started again. The Schlieren test for the three fuels (MF, DMF, Isooctane) were performed at three temperatures elevated from 60°C to 120°C and equivalence ratios varied from 0.6 to 1.4 under an initial pressure of 0.1 MPa. At each test condition, the test was repeated 3 times and the analysis was based on the averaged data. The data analysis, including the image processing and the calculation of the parameters is discussed in section 3.5.3.

3.4 Optical Engine and PLIF Laser

In this work, high speed imaging tests and PLIF tests were conducted in an optical engine in order to evaluate the combustion of the bio-fuels. The optical engine used for the experiments was a single cylinder DISI engine (also equipped with PFI) which was based on a Jaguar engine. The PLIF laser used was a Dantec dye laser (TDL90) which was pumped by a Brilliant B Nd Yag laser. The CCD camera and the image intensifier used in both experiments are described in section 3.1.4. In the following sections, the optical engine, the PLIF laser and the related data processing technique are introduced.

3.4.1 Single Cylinder Optical Engine

The 4-stroke single cylinder optical engine is shown in Figure 3-9. This 0.562 L single cylinder engine direct-injection spark-ignition (DISI) engine was developed by Ford/Jaguar. The extended piston was specially designed to provide optical access from the bottom via a transparent quartz piston window. A 45° mirror was installed to allow the camera to capture the spray and combustion images inside the combustion chamber. As shown in Figure 3-9, two white water pipes were connected to the steel liner in order to provide water coolant.

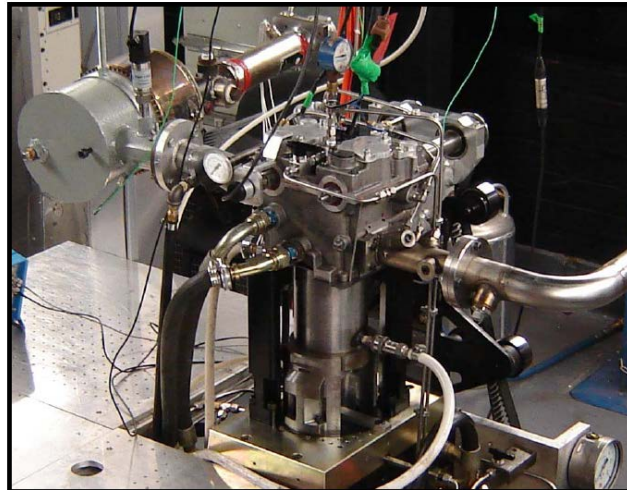


Figure 3-9: Single cylinder optical engine

This single cylinder engine had four valves including two intake valves with a diameter of 36mm and two exhaust valves with a diameter of 30 mm. The cylinder head was designed with a 13° pentroof and a centrally mounted spark plug. The injector was installed near the spark plug. The bore and stroke of this engine are 89 mm and 90.3 mm respectively and the engine compression ratio was 11:1. The system was directly installed on a cast-iron test bench which means that no counter-balance was required on the crankshaft. More details of the engine can be found in section

3.4.2.2.

3.4.2 Engine Test Facility (High Speed Imaging) Overview

The schematic of the engine test facility is shown in Figure 3-10. Several main parts were involved in the investigation: the optical engine, the camera, the engine control system. Each of them is discussed in detail in the forthcoming sections.

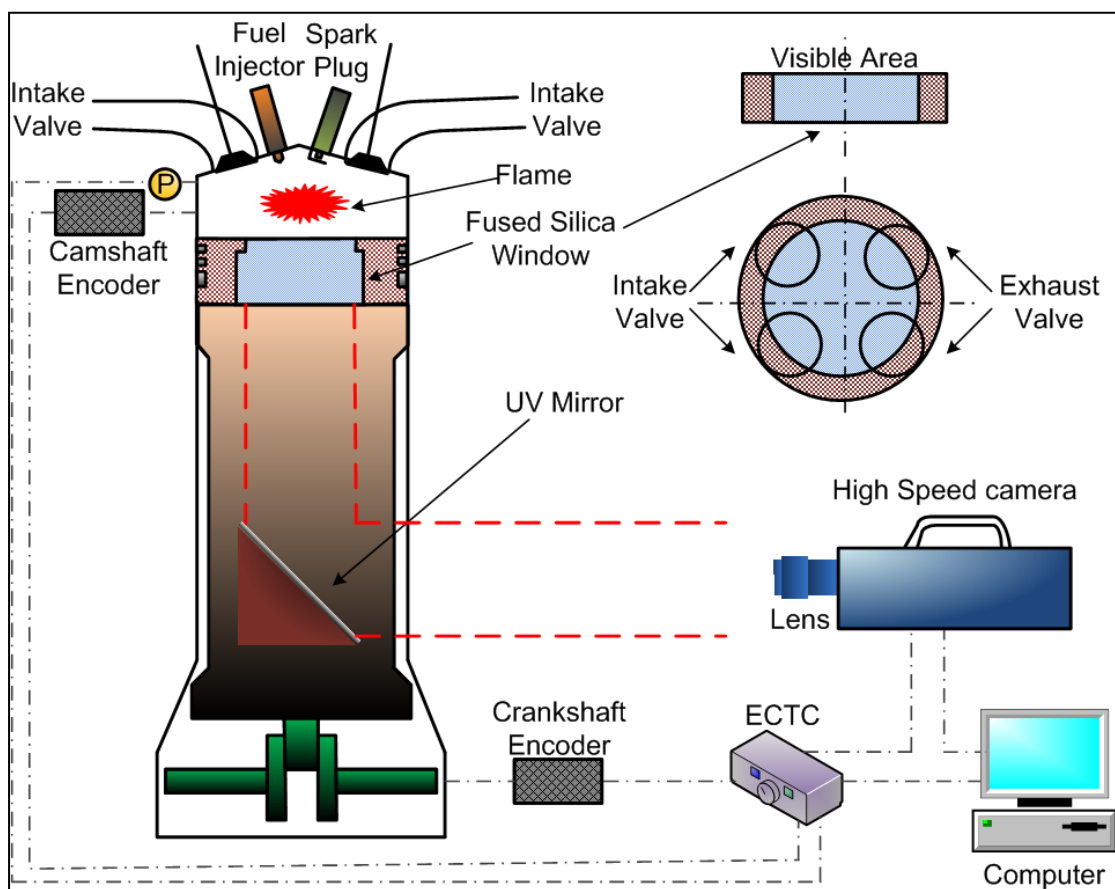


Figure 3-10: Schematic of the optical engine, instrumentation and acquisition systems

3.4.2.1 Dynamometer and Electric Motor

The optical engine crankshaft was motored by an electrical motor and coupled with an eddy dynamometer supplied by Trans-drive. This dynamometer worked under three phase, 340 volt electric power and could maintain a constant speed or constant engine load at motoring or firing conditions. The speed of the engine could be manually controlled on the engine control box which had a digital indicator on it.

3.4.2.2 Engine Specification

The specification of the optical engine is shown in Table 3-2. It was a 4 stroke single cylinder engine developed from a Ford/Jaguar V8 engine. The displacement of the engine was 0.562 L and the clearance volume was 0.0562 L. The connecting rod length was 148.9 mm. The engine had two exhaust valves and two intake valves and the spark plug was installed in the centre of the cylinder. The injector was installed near the spark plug, as shown in Figure 3-10.

Table 3-2: The optical engine specification

Parameter	Value
Engine head type	Jaguar V8
Cycle	4-stroke
Bore	89 mm
Stroke	90.3 mm
Displacement	0.562 L
Clearance volume	0.0562 L
Geometric Compression Ratio	11:1
Connecting Rod length	148.9 mm
Number of Intake Valves	2
Number of Exhaust Valves	2
Intake Valve Lift	10.5 mm
Exhaust Valve Lift	9.3 mm
Intake Camshaft Duration	250 CAD
Exhaust Camshaft Duration	250 CAD

For current work, all the tests were performed at an engine speed of 1200 rpm due to the requirement of using the PLIF laser. In order to synchronize the PLIF laser with the engine, at every cycle, a signal was given to the timing box at a specific crank angle (this timing of the signal could be varied on the control software). The frequency of the PLIF laser was fixed at 10 HZ. Thus, the frequency of the signal given by the engine control software was only 10 HZ, which gave the engine a speed of 1200 rpm. In order to make it convenient to analyse, the high speed imaging test for turbulent flame was also performed at an engine speed of 1200 rpm.

The engine valve timing was set as following: the intake valve opens (IVO) at 16° bTDC and exhaust valve closes (EVC) at 36° aTDC. The maximum intake and exhaust valve lifts occurred at 109° aTDC and 89° bTDC, respectively.

3.4.2.3 Direct Injection System and Fuel Supply

The engine could operate under both high pressure GDI (150 bar) and low pressure PFI (3 bar). These two systems could operate separately or simultaneously. This investigation mainly focused on the GDI operation. An accumulator was used to store and pressurize the fuel. Before the engine was operated, high pressure nitrogen gas was connected to the bottom of the accumulator to apply the 150 bar pressure to the fuel. The fuel line was connected to the engine by the injector. A gauge was installed near the injector to monitor the injection pressure. The injection timing and injection duration was controlled by the engine control software, which is described in section 3.4.2.7. The injector used here was the Bosch AJ133 injector.

3.4.2.4 Ignition System

The in-cylinder charge was ignited by the discharge of the spark plug, which was placed in the centre of the pentroof combustion chamber. The ignition timing and coil discharge duration could be controlled by the engine control software. Variable spark timing could be achieved for different combustion strategies.

3.4.2.5 Pressure Recording and Coolant Temperature Control

The cylinder pressure was measured by a Kistler 6051A pressure sensor which was coupled with a Kistler 5011B charge amplifier. A LabVIEW program made by the previous researchers was used to record the pressure and indicate the load and COV.

The test facility contained a water heating and cooling circuit for the engine cylinder head and the liner. A K-type thermocouple was used to measure and control the water coolant temperature. In this investigation, the coolant temperature was set as 85°C. The oil heating and cooling system operated separately and the temperature was set at 85°C too.

3.4.2.6 Optical Piston and Cylinder Liner

The optical piston is shown in Figure 3-11. The flat piston top was made of quartz, which allowed light to travel through the piston. The diameter of the quartz window was 70 mm. However, the diameter of the visible area is only 60% due to blockage caused by the mirror fixture. Two sets of gas rings and one oil ring were mounted on the optical piston. The material of these rings was Torlon. A steel liner with water coolant connected on both sides was typically used for the combustion tests. A full stroke quartz liner could also be used to examine the spray from the side (shown in Figure 3-11 b). The inner diameters for both liners were all 90 mm. The thickness of the optical liner was 25 mm. A gasket was positioned between the liner and the cylinder head in order to seal the combustion chamber. In order to fix the liner on the cylinder head, the liner seat was raised up and kept in place by 20 bar of compressed nitrogen gas supplied by an additional nitrogen bottle.

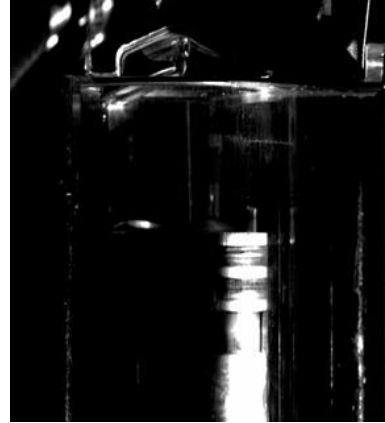


Figure 3-11: Optical engine piston and full stroke transparent optical liner on the single cylinder engine

3.4.2.7 Engine Control

The engine control system contained two main parts: the LabView software run by the control computer and the control box. As an integral system, they controlled the injection timing, injection pulse width, ignition timing (single injection and double injection could be achieved), coil charge time and the trigger timing. The control software (called Engine Timing Control System) was developed by the ICE Group, as shown in Figure 3-12. All the operational parameters mentioned above could be controlled in real-time using the software.

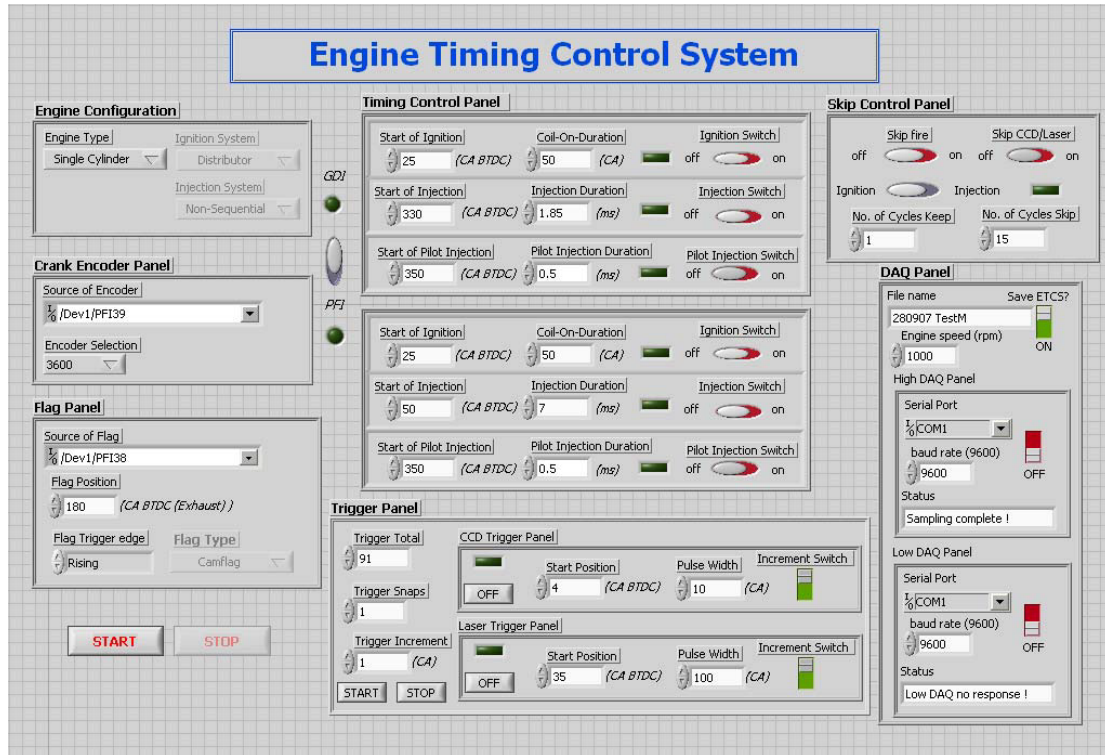


Figure 3-12: The engine timing control system control panel

The control box integrated the hardware needed for the engine operation. A NI PCI-6023E interface card was used to relay the signals from the computer to the engine in order to control it. This NI card was used to control the engine and process various parameters. The engine timing was defined by the crankshaft encoder. The crankshaft encoder, which was made by Kistler, provided 360 TTL signals every crankshaft revolution and determined the location of the piston in regards to the top dead centre (TDC). The whole system control including the spark timing, injection timing, trigger timing, and the pressure recording, depended on this signal.

3.4.2.8 Camera Setup

The camera used in the high speed imaging and the PLIF tests for combustion

diagnostics was the Phantom V710 high speed camera. In order to capture the relatively weak luminosity from the flame or the fluorescence, the Hamamatsu intensifier was used. Both of these devices were described in previous sections. The camera resolution used in both tests was 800x800 pixels. The frame rates of the cameras were 10,000 Hz and 10 Hz for the high speed imaging and the PLIF test, respectively.

Before each test, the camera needed to be accurately placed in order to avoid any flame image distortion. The lens needed to be focused at the top of the piston stroke so that high quality flame images could be achieved. In the PLIF tests, a special UV lens (described in chapter 3.4.3.4) was used to capture the 308 nm fluorescence. A narrow band (308 ± 8 nm) OH filter was installed on the lens to filter the chemiluminescence from the flame.

3.4.2.9 Time-box and System Synchronization

A time-box supplied by Dantec was used to synchronize the camera and laser system with the engine system. The timing of the camera and the laser was accurately controlled by the Dynamic Studio software provided by Dantec. The time-box had 8 BNC (Bayonet Neil-Concelman) connection points on the front panel which provided the TTL signal output to the laser, camera and intensifier. The timing of these devices could be accurately varied with an accuracy of 12.5 ns. On the back panel of the timing box, there were two BNC connection points: channel 1 and channel 2. The function of channel 1 was to start a recording cycle: when a signal is received, it

started a cycle in the software and recorded a number of images according to the setting of the user. The function of channel 2 was to enable a single image recording within a recording cycle: when it received a signal, the software enabled the recording of only one image. The input and output channels of the timing box enabled the synchronization to be made between the engine and the optical system including the laser, the camera and the intensifier. Thus, the spray and combustion images could be recorded at a specific crank angle according to the need of the researcher.

3.4.3 PLIF Laser

In this investigation, the TDL 90 dye laser, which was powered by the Brilliant B Yag laser, was used to generate the laser beam. Both of these devices were supplied by Dantec. As mentioned above, the control of the laser was implemented via control software called Dynamic Studio. The connection and timing of the system was achieved by the timing box. In the practical experiments, in order to convert the laser beam into a laser sheet, a beam expander was used.

3.4.3.1 PLIF Laser

The PLIF laser actually contained two main parts: the Brilliant B Yag laser and the TDL 90 dye laser. The Brilliant B Yag laser acted as a power source for the dye laser. By using different modules of harmonic, the wavelength of the emitted light from the Yag laser could be altered between 1064 nm, 532 nm, 355nm and 255nm. For these

tests, the second harmonic module was used thus the 532 nm light was generated by the Brilliant B laser. The energy of each pulse of laser was 400 mJ. The 532 nm laser beam was then guided to the dye cells in the dye laser in order to halve the wavelength to around 280 nm. In the meantime, the dye laser allowed the wavelength to be varied within a small range (276nm-284nm). Thus, the OH-LIF test could be performed using the dye laser.

3.4.3.2 Control Software

The Dynamic Studio, which was supplied by Dantec, controlled and synchronized the laser, the camera and intensifier with the engine. Internally in the software, the connection of the trigger cables for all the devices could be altered according the physical connection on the timing box. Therefore, the software knew where to send the trigger signal. The timing of each device thus could be controlled via the signal sequence sent from the timing box with an accuracy of 12.5 ns. Using this software, the settings of the devices connected to the timing box could also be changed (e.g. the gate time of the camera and the intensifier). Furthermore, the control panel of this software was capable of defining the camera speed and the number of images taken in one running cycle.

3.4.3.3 Beam Expander

In order to expand the laser beam into a laser sheet, a beam expander (also called sheet optics) was used in this study. The Dantec 9080X0841 beam expander, as shown

in Figure 3-13, produced a light-sheet with adjustable thickness and adjustable focus length, which enabled the generation of a laser sheet for PLIF and PIV. In the OH-LIF study particularly, the beam expander converted the laser beam with a diameter of 8 mm to a laser sheet with a width of 50 mm and a thickness of 1.5 mm.

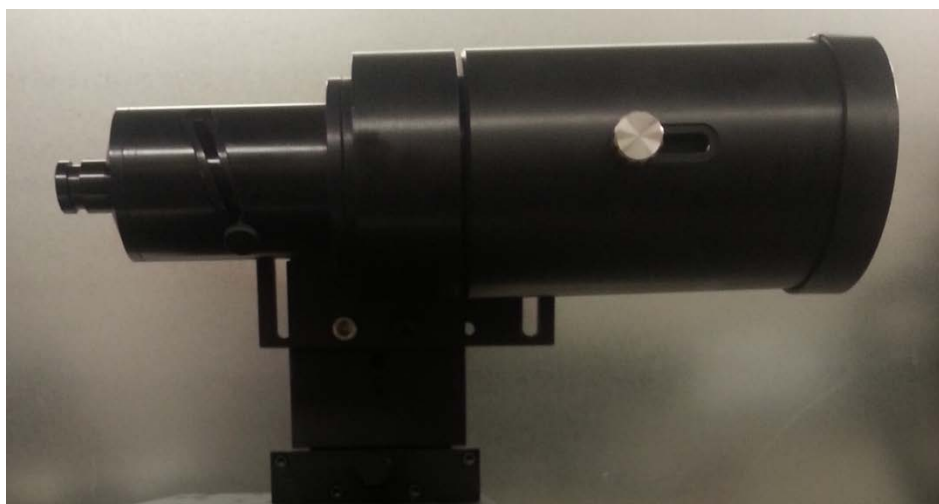


Figure 3-13: The beam expander for OH-LIF

3.4.3.4 UV Lens and Filter (OH-LIF)

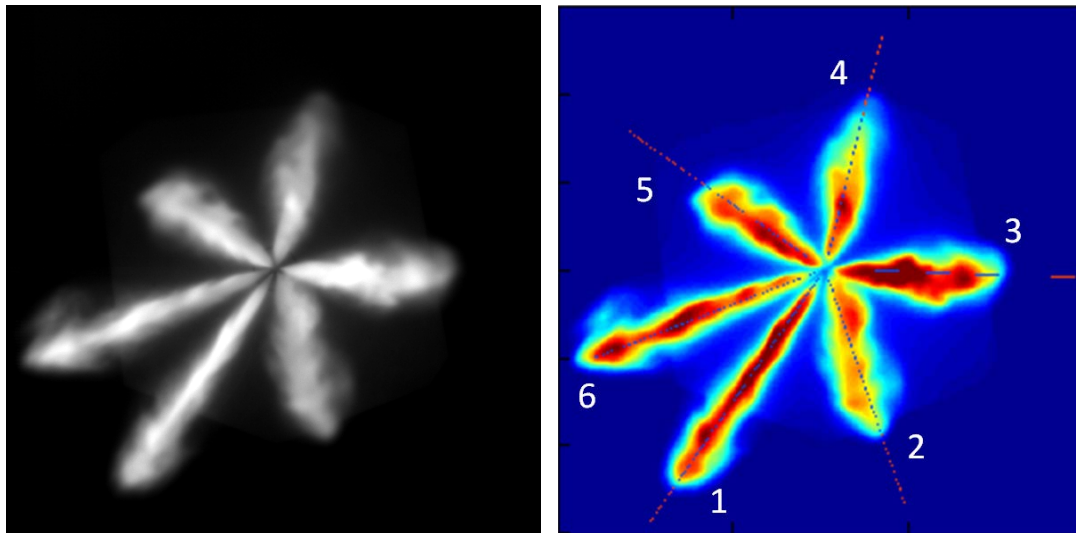
In order to perform the OH-LIF test, a special UV lens had to be used as the wavelength of the fluorescence light emitted from the OH radicals is around 308 nm which is out of the visible range (390 nm-700 nm) of the human eye and cannot be captured by an ordinary lens which is designed to capture light in the visible range. In this investigation, the Nikon 105 mm UV lens was used. The f number of the UV lens could be varied from 4.5 to 32. This lens allowed light in the range of 220nm-700nm to travel through. A light filter was installed on the lens to filter the light from other sources (e.g. the chemiluminescence from the flame). The filter had a

centre pass-through wavelength of 308 nm and a FWHM (Full Wave at Half Maximum) of 8 nm.

3.5 Data Processing

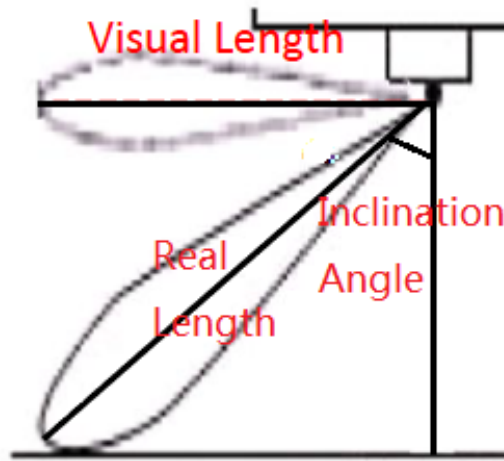
3.5.1 Spray Penetration Length and Cone Angle Measurement

The spray penetration length and the cone angle are essential parameters describing the macroscopic characteristics of the spray. In order to measure the spray tip penetration length, a MATLAB code was created to process the images recorded by the high speed camera. Figure 3-14 shows the method used to measure the spray tip penetration. Figure 3-14 a is the raw image taken by the camera; Figure 3-14 b is the image processed by the MATLAB code; Figure 3-14 c illustrates the transformation of the visual length to the real length. Figure 3-14 d shows the measurement of the spray cone angle.



(a)

(b)



(c)



(d)

Figure 3-14: Measurement of the spray tip penetration (a) Original image (b) Image processed by MATLAB code (c) Transformation from visual length to real length (d) Measurement of the cone angle

The MATLAB code measured the penetration lengths of the 6 jets by applying a measuring line on each jet, as shown in Figure 3-14 b. A threshold of 20% was applied in order to define the spray tip along the measuring lines. In order to simplify the analysis in this study, only jet 1 is used for comparison between fuels. The images for the injection were analyzed and numbers of pixels which represent the visual

penetration lengths were recorded. The real penetration length could then be calculated according to the inclination angle of the spray, as shown in Figure 3-14 c. The pixel/length ratio was measured and calculated before the test. The last step was to transfer the length from pixel to metric length. For this study of the macroscopic spray characteristics in this thesis, in order not to overcomplicate the analysis, only the penetration length and cone angle of jet 1 were used for further comparison.

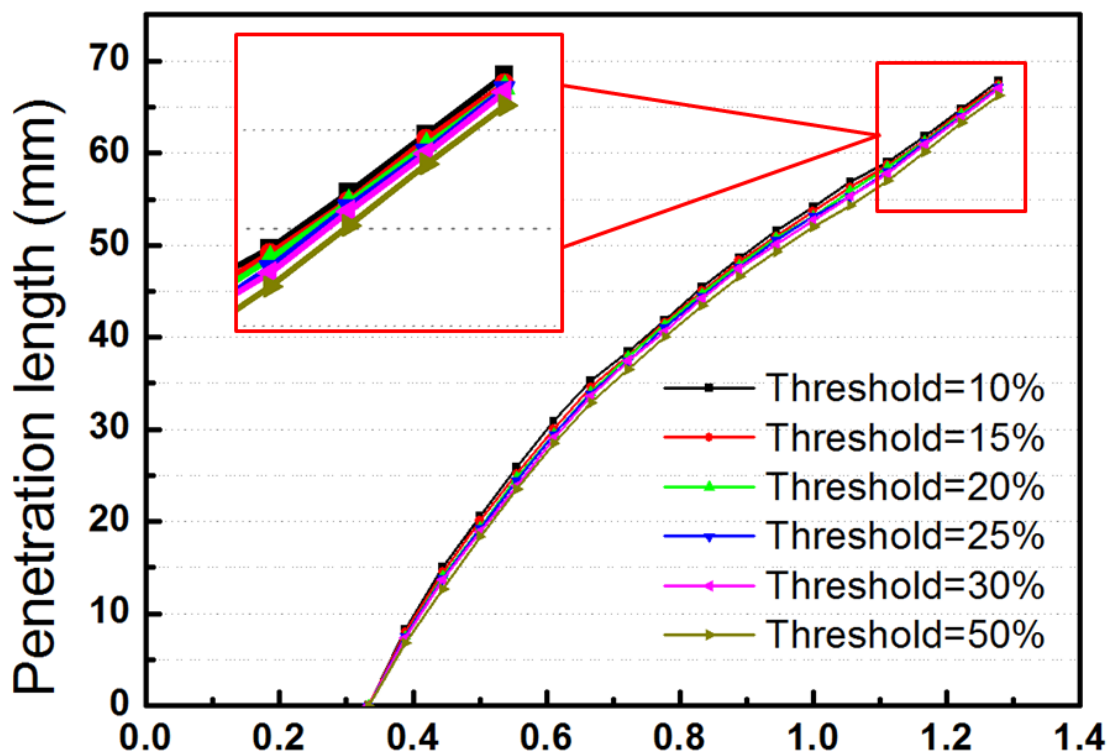


Figure 3-15: Effect of different thresholds on the penetration length measurement.

In order to obtain accurate penetration length using the MATLAB code, a large numbers of thresholds were tested on different sets of spray images. Figure 3-15 shows an example of the sensitivity analysis of the threshold on the penetration length measurement. The penetration lengths (jet 1) of MF spray under 150 bar injection pressure and 1 bar back pressure at room temperature of 20°C were measured using different threshold ranging from 10% to 50%. It can be seen that the penetration

length shortened if a higher threshold was applied to the measurement. However, the influence of the threshold on the penetration length measurement for current methodology was not very big. For instance, differences between the penetration length measured with 10% threshold and the penetration length measured with 50% was only around 4%-5% at the end of the injection. Also, the difference between 15% threshold and 25% threshold at the end of the injection is only around 1%. The threshold was chosen to be 20% because the author found that a 20% threshold can very clearly indicate the boundary of the spray at other directions (not only on this measuring line). For the macroscopic spray characteristics analysis in this study, this threshold number, 20%, was applied on all the measurements to ensure that same criteria were used for the spray measurement of different fuels.

The cone angle represents the quality of the mixture formation. In this study, the cone angles for all the jets were measured in the end of the spray duration. As shown in Figure 3-14 d, two fitting lines were plotted following the boundary of the maximum spray contour. The measured angle was defined as the spray cone angle.

3.5.2 Droplet Size and Velocities Measurement

The PDPA measurement in this thesis is conducted on jet 1 (Jet number shown in Figure 3-14) as well. In order to explain the principle of the droplet size and velocity measurement, the schematic of light incident on a droplet has been provided in Figure 3-15. As shown in the figure, when the light rays (from the transmitter) are incident on the spherical droplet, part of the light is reflected from the external surface of the

sphere (called reflected light), while the other part of the light is refracted and then goes into the droplet sphere. Again, this part of light is reflected and refracted on the inner surface of the droplet sphere. This refracted light on the inner surface is called the first-order refracted light. The rays which reflected from the inner surface and refracted in the opposite part of the inner surface are called the second-order refracted light. The rays which are incident on different positions of the droplet sphere have different phase difference when they are received by the signal detector due to the difference of the light path. This phase difference is associated with droplet diameter and thus is used to determine the droplet size.

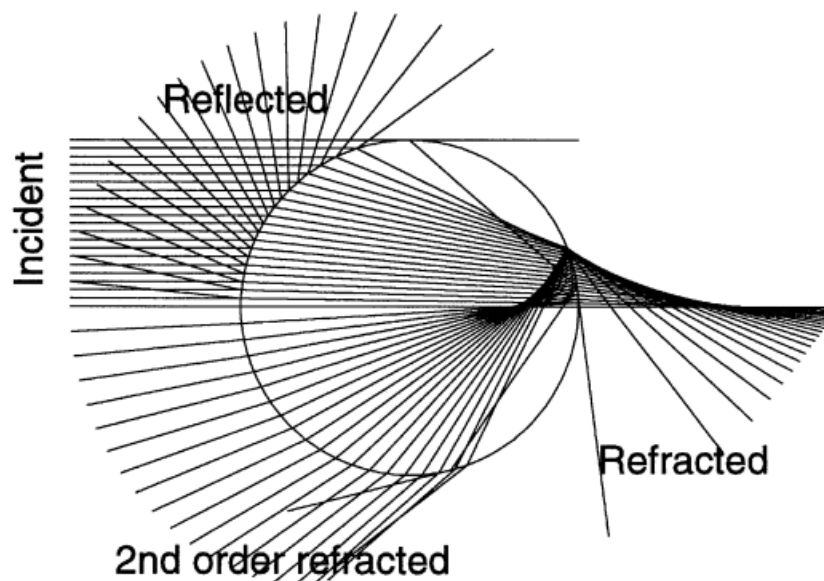
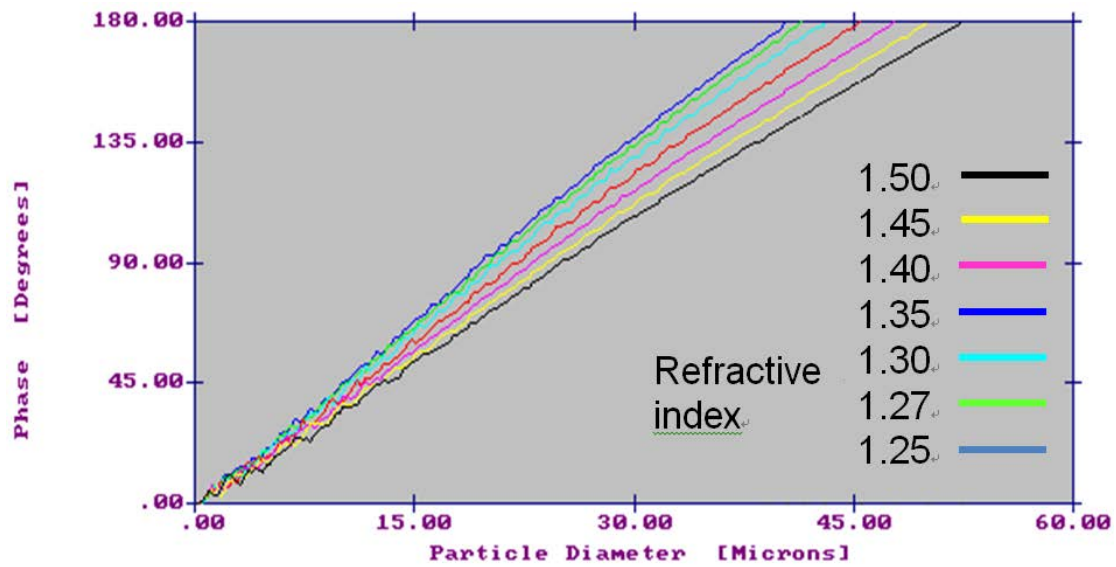


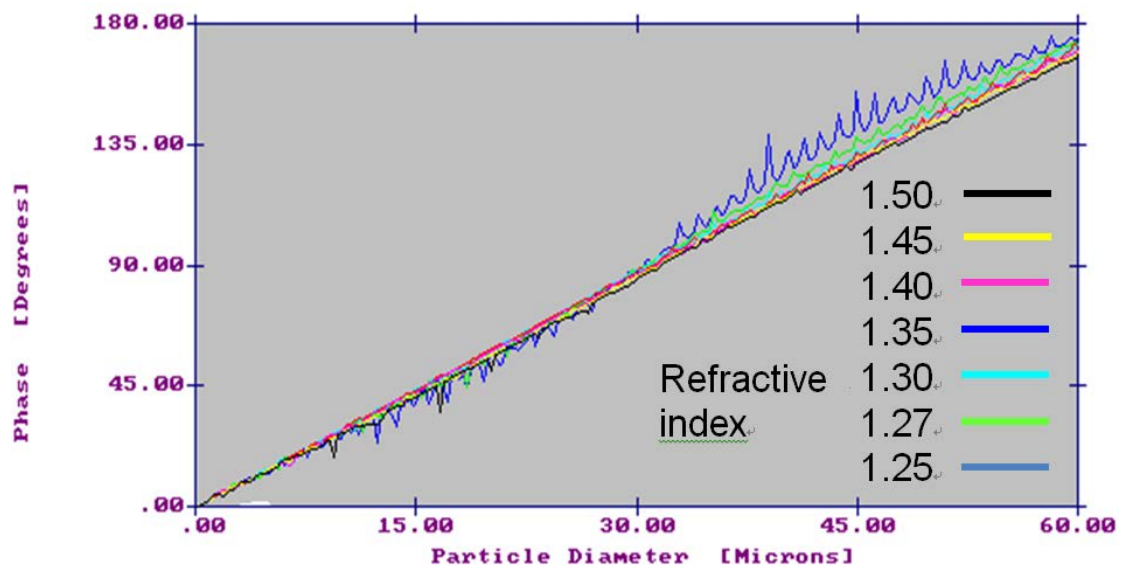
Figure 3-15: Scattering modes of a set of rays incident on a liquid droplet (Dantec-Dynamics, 2006)

For the PDPA system used in this study, the angle between the transmitter optics and the receiver is 70° , as shown in Figure 3-7. This is different from the configuration used in other researchers' research, which the refracted light is collected at 30° toward

the incident light. There are several reasons for this configuration to be adopted by the Dantec system. The first reason is the phase/refractive index response linearity. For the 70° scattering geometry, the phase/refractive index relationship is linear for different droplet sizes, whereas the 30° scattering geometry suffers from poor phase linearity for droplet size smaller than 10 microns. Thus it increases the ambiguity in determine droplet sizes at the 30° scattering geometry. The second reason is the sensitivity of the measurement towards the refractive index. Pitcher et al (1990) examined the sensitivity of droplet size measurement to refractive index change. Figure 3-17 shows the phase/droplet size relationships for 30° and 70° scattering geometry measured by them. It can be seen from this figure that for the 70° scattering geometry, despite the change of refractive index from 1.27 to 1.45, a single phase/droplet size factor is applicable (For their PDA system, it is 5.01° per micron). However, for the 30° scattering geometry, the phase/droplet size factor varies from 5° per micron (refractive index of 1.22) to 4° per micron (refractive index of 1.45).



(a)



(b)

Figure 3-17: Effect of refractive index changes on PDA phase factor (a) 30° scattering geometry (b) 70° scattering geometry (Picher, 1990)

In current study, the vessel temperature is elevated to 60°C and 90 °C to allow the effect of ambient temperature on the fuel spray to be examined. However the refractive indices of the fuels droplets will change in the high temperature environment. Thus, errors may occur during the tests because all the refractive indices

used in this study are the refractive indices for the fuels at room temperature. In order to estimate the level of the possible droplet size measurement errors result from the change of environment temperature, it is necessary to know the effect of the temperature on the refractive indices. However, refractive data for fuels at elevated temperature are scarce. Thus, the Eykman equation, as shown in Table 3-3, is used to estimate the refractive indices at elevated temperature. The Eykman equation is an empirical equation derived for hydrocarbons. It generally produces good estimation of the refractive index based on the density change of a fuel. The variation of the refractive index, n , of the fuels with density, ρ , and temperature, T , is indicated in the table.

Table 3-3: Calculation of the refractive index under different temperatures.

Ekyman equation: $(n^2-1)/(n+0.4)=\text{Const} * \rho$						
Fuel	20 °C		60°C		90 °C	
	ρ (kg/m ³)	n	ρ (kg/m ³)	n	ρ (kg/m ³)	n
MF	913.2	1.43	868.0	1.41	829.8	1.39
DMF	889.7	1.44	852.8	1.42	819.2	1.40
Isooctane	691.9	1.39	660.5	1.37	633.2	1.36
Ethanol	789.0	1.36	747.7	1.34	714.1	1.32
Gasoline	744.6	1.40	713.46	1.38	692.4	1.37

From this table, it is known that the refractive indices of all the fuels are in the range of 1.22 to 1.45 between the temperature of 20°C and 90 °C. As it is discussed before, for the 70° scattering geometry, a single phase/droplet size factor could be used for the PDA system to calculate the droplet diameter. According to Pitcher's work on the 70°

scattering configuration (Picher, 1991), the corresponding error over the refractive index range of 1.22 to 1.45 ranges by using a single refractive index for instrumental phase factor calculations is within 1%. Thus, the author is confident that although all the refractive indices used in this study are the refractive indices for the fuels at room temperature, the systemic error due to the change of refractive indices at an elevated temperature environment is minimal.

There are also other good reasons for the author to use the 70° scattering configuration in this study. The test is performed in the vessel. However, the front window towards the laser transmitter on the vessel is not big enough to allow the refractive light to be collected at 30° angle. Thus, a 70° scattering geometry allows the receiver to collect the light from the side window. Thus, for the current test 70° scattering geometry is the best choice.

3.5.3 Schlieren Image Processing

In this study, the schlieren test on each point is repeated for 3 times and the averaged results are used for further analysis. The same repetition times and methodology are broadly adopted in other literatures on laminar flame study in the vessel (Broustail, 2011, Vukadinovic, 2013, Wu, 2012, Jerzembeck, 2009, Gu, 2010). In order to detect the flame boundary from the Schlieren images, a MATLAB code was developed. Firstly, the original images were rotated 45 degrees to avoid the vague which the electrodes may create in defining the flame boundary (The light intensity gradient cannot be detected due to the blockage of the electrodes). Then, the radii of the flame sphere were measured by detecting the change of the gray scale value from four

directions as shown in Figure 3-18. The radii measured from the four directions were averaged in order to reduce errors which may occur in the measurement process. In other researchers' work, the flame radii are usually measured at the vertical direction rather than the current 4 directions. However, due to the non-spherical of the flame, the two methods might generate different measurement results. In order to justify the current method, the author measures the flame radii (between 6mm and 18mm) from the vertical direction and compares them with the current results. At around 6mm, the flame radii measured from vertical direction are about 5%-7% larger than the current measurement. As the flame expand to a radius of 7mm to 8 mm, the difference between these two decreases to around 3% to 4%. When the flame radius is bigger than 9mm, the difference further drops to 2%. As the flame becomes larger, the difference between these two methods decreases to 1%. It can be seen that as the flame volume becomes larger, the flame becomes spherical and the measurement from all directions becomes similar. Due to these measurement error in the current methodology, the current calculated unstretched flame speed is around 1%-2% lower than it should be. In the following part, the formulas used for the calculation are given.



Figure 3-16: Laminar flame radius detection.

In the analysis, only the photos with flame radii between 6mm and 18mm were used in order to avoid the effect of spark energy disturbance (Bradley, 1998, Huang, 2006), pressure increase due to the burning (Zhang, 2008), and space confinement (Burke, 2009). The research of Bradley et al.(1998) and Huang et al.(2006) show that the flame speed would not be influenced by the spark energy if the flame radius is greater than 6 mm. Also, the study of Burke et al. (2009) shows that the effect of the space confinement on the flame propagation could be ignored when the flame radius is less than 0.3 times of the chamber radius. The chamber radius used in this study is around 60 mm. Thus, it is reasonable to analyze the flame radii less than 18 mm (60 mm*0.3=18 mm).

The laminar flame speed S_n (unit: m/s) was calculated as:

$$S_n = dr_u/dt$$

Where r_u (unit: m) is the flame radius and t (unit: s) is the time after the spark. After obtaining the stretched flame speed, the stretch rate α (unit: s^{-1}) could be calculated as:

$$\alpha = 2S_n/r_u$$

The linear relationship between the stretch rate α and the laminar flame speed S_s (unit: m/s) can be used to obtain the Markstein length and the laminar flame speed:

$$S_n = S_s - L_b \cdot \alpha$$

where L_b (unit: m) is the Markstein length and S_s (unit: m/s) is the laminar flame speed. S_s was calculated by extrapolating S_n to stretch rate of 0. L_b is the negative value of the gradient of the curve obtained when flame propagation speed is plotted against the stretch rate.

The laminar burning velocity u_l (unit: m/s), is deduced from the following equation:

$$\mu_l = S_s \cdot \rho_b / \rho_u$$

where ρ_b (unit: kg/m³) represents the burned mixture densities and ρ_u (unit: kg/m³) represent the unburned mixture densities. Using the conservation of mass equation, the ratio of the burned mixture density (ρ_b) to the unburned mixture densities (ρ_u) could be found. The formula can be expressed as following:

$$\rho_b / \rho_u = V_u / V_b = n_u T_u / n_b T_b$$

In this equation, n_u (unit: mol) and n_b (unit: mol) are numbers of moles of the reactants and the products in the combustion vessel; T_u (unit: K) and T_b (unit: K) are the initial temperatures and the adiabatic flame temperatures, respectively. The software HPFLAME (Turns, 1996), which incorporated the Olikara & Borman equilibrium routines (Olikara, 1975), was used to determine the adiabatic flame temperature at different initial temperatures and equivalence ratios. The input file for this software requires the fuel definition by providing the number of carbon, number of hydrogen, number of oxygen and number of nitrogen atoms of the fuel molecule.

Other parameters are also needed: the equivalence ratio, a guess for the adiabatic flame temperature, the initial pressure and the reactant's enthalpy. Using these parameters, the reactants' enthalpy could be easily calculated. Then, this software utilizes the fact that the reactants' enthalpy equals to the products' enthalpy (first-law of thermodynamics) to calculate the products' constant-pressure adiabatic flame temperature.

The flame thicknesses under different test conditions were calculated via the following equation:

$$\delta_l = v / \mu_l$$

where v (unit: m^2/s) represents the kinematic viscosity of the air/fuel mixture.

The Laminar burning flux, f (unit: $\text{kg}/\text{m}^2\text{s}$), which is the eigenvalue of the flame propagation, is calculated using:

$$f = \mu_l * \rho_u$$

3.5.4 Combustion Image Processing

An in-house developed MATLAB program was used to process the images. The raw image data were read into the computer in sequences and background subtraction was applied in every cycle followed by noise signal removal through median filtering. Images were converted to binary images and the boundary of the flame shape was identified by the software. In order to let the MATLAB program define the boundary accurately, different thresholds were tried and compared, as shown in Figure 3-19. With a lower threshold applied to the analysis, the flame boundary tended to be larger

because the dark part was reckoned as the flame. When a higher threshold was applied, only the bright parts of the flame could be detected. Through trial and error, the author believed that 16% was appropriate for the analysis. As it can be seen from Figure 3-19, when a threshold of 16% was applied, the boundary of the flame was neither bigger than it should be nor smaller than it should be. Therefore, for all the flame image analysis, a threshold of 16% of the peak grayscale value was applied.

Threshold	Raw image	Binary image	Image boundary
5%			
10%			
16%			
20%			
30%			
40%			
50%			

Figure 3-19: Imaging processing using different thresholds.

After detection of the flame boundary, the average flame front propagation speed between two adjoining images could then be estimate using the following equation:

$$V=\Delta S/(L\Delta t)$$

where ΔS is the augmentation of the flame area; Δt is the time interval between the two images; and L is the length of the flame boundary. Because the interval between 2 adjacent images was extremely short and thus the increment of L in the later image was negligible, the flame boundary length L could be treated as a constant in one calculation. The process of the 2D flame speed calculation is shown by Figure 3-20 which is based on an ensemble average. When part of the flame front went beyond the window scope, only the visible flame front boundaries could be used to calculate the flame front propagation speed.

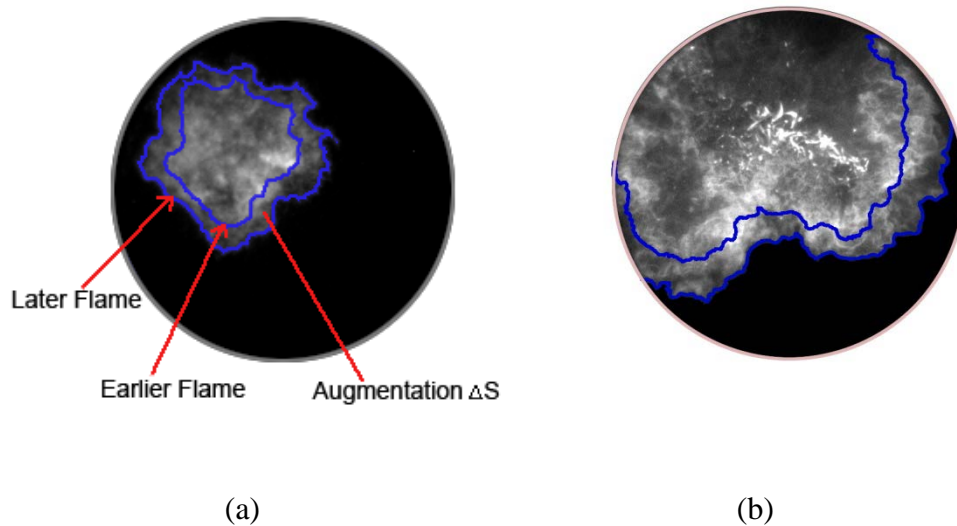


Figure 3-20: Flame speed calculation (a) Normal condition (b) Flame partly beyond the window range

3.5.5 OH-LIF

Figure 3-21 is a schematic of the visible area through the piston window used for both flame and LIF imaging. The coloured region indicates the area illuminated by the laser sheet. The boundary areas of the laser sheet where the energy is weak have been removed from the measurement, leaving an available width of 50 mm (as mentioned before, the thickness is 1.5 mm). The laser sheet is projected into the engine cylinder at 9 mm below the spark plug via a small side window on the optical engine. The images were captured at a resolution of 800x800, covering the whole combustion window. For each crank angle, 200 images from continuous stable cycles were acquired in the OH-LIF tests. Before the engine experiment, an open flame burner was used to tune the UV laser wavelength to find OH's absorption line near 283 nm, which lead to the strongest LIF emission. The engine was operated at 1200 rpm which allowed the synchronization of engine cycle with the laser's frequency. The laser fired at certain crank angles set by the control system. For a whole cycle observation, the measuring points started from 15°CA BTDC to around 40 °CA ATDC, with an interval of 3°CA at the early stage of the measurement and 5°CA at the late stage. An energy meter was used to observe the laser energy during the experiment.

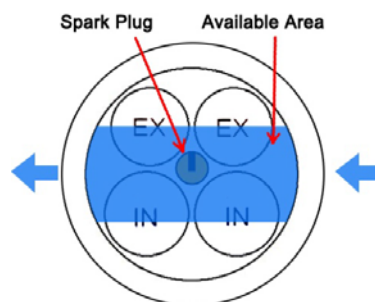


Figure 3-21: The schematic graphic of the piston window and the laser sheet region

It is known that temperature and pressure conditions have significant impacts on quantum yield and the quenching effect (Schulz, 2005, Verbiezen, 2007, Zhao, 2012 and Zhao, 1998). In this study the area of OH distribution was only taken as an indicator of combustion development. As the laser energy was high enough to overcome any significant absorption attenuation, the main correction needed for the images was the laser energy correction applied with the energy meter recording. After background subtraction and removing the region outside the laser area, the images were corrected and binarized using a threshold which was obtained from an evaluation of all the averaged data and confirmed by a test covering 20 groups of the pictures. In the image processing of all the sequences, the threshold was set to be 20% of the brightest point. As it can be seen from Figure 3-22, if the threshold was higher than 20%, then not all the area which has OH signal could be detected. Also, if the threshold was lower than 20%, the cavities inside the OH area could not be distinguished clearly. Thus, the threshold of 20% was applied so that the cavities inside the OH area could be distinguished while the loss of boundary information was minimized. After this step, binary images could then be used to calculate the pixel number of the LIF signal area and the average results, which provide information of OH radical distribution.

Threshold	Raw image	After correction	Binary image
10%			
15%			
20%			
25%			
30%			
40%			

Figure 3-22: Image processing for OH-LIF using different thresholds.

3.5.6 Heat Release Analysis

The in-cylinder pressure is very important for understanding the combustion behavior. One of the main reasons is because it could be used to calculate the heat release rate and the related mass fraction burned (MFB). In this study, the net heat release rate ($dQ/d\theta$) is calculated using the method described in an internal combustion engine handbook (Stone, 1999).

$$\frac{dQ}{d\theta} = \frac{\gamma}{\gamma - 1} P \frac{dV}{d\theta} + \frac{1}{\gamma - 1} V \frac{dP}{d\theta}$$

In this equation, γ is the heat capacity ratio (c_p/c_v); P (unit: Pa) is the instantaneous in-cylinder pressure; V (unit: m^3) is the instantaneous volume of the combustion chamber and θ (unit: $^\circ$) is the crank angle.

After the calculation of the heat release rate, MFB then could be calculated by integrating the heat release rate:

$$MFB = \frac{\int_{\theta_s}^{\theta_i} \frac{dQ}{d\theta} d\theta}{\int_{\theta_s}^{\theta_e} \frac{dQ}{d\theta} d\theta}$$

3.6 Experiment Uncertainty Analysis

3.6.1 Uncertainty in the Macroscopic Characteristics of the Spray

The uncertainty in the macroscopic characteristics analysis is mainly caused by several issues. The first cause of the uncertainty is the shot to shot variation of the spray. The shot to shot variation may affect the measure of the penetration length and

the spray cone angle. It is caused by the turbulent and irregularity of the spray-air interface. In order to avoid the shot to shot variation, the spray imaging tests are repeated 5 times and the averaged results are used for the analysis. The other factor which might cause error for the measurement is the pixel ambiguity. The Matlab code used for the penetration length measurement can only define pixel in the form of integer. So there might be a ± 1 pixel error in any measurement. This 1 pixel error equals to 0.2 mm of error in the real measured length.

3.6.2 Uncertainty of the PDPA System

There are several reasons which might affect the measurement accuracy in the PDPA tests. Firstly, the phase difference could cause uncertainty. The PDPA detector has certain tolerances for the phase detection and thus the precision of the measurement is affected. The second affecting factor is the droplet sphericity. As shown in Figure 3-6, the PDPA system has 3 detectors which give 2 pairs of phase differences. The phase difference for each pair provides the information about the curvature over a certain arc of the droplet surface. Thus, 2 pairs of diameters are obtained. If the droplet is spherical, the measured diameters will be the same. However, if the droplet is not spherical, the difference between the 2 diameters will be large. If the diameter difference is larger than a certain limited set by the software, the measurement of the droplet diameter would be rejected and therefore error will occur. The third affecting factor is the trajectory effect which is attributed to the Gaussian intensity distribution. In the measurement, the first-order refraction is adopted as the scattering mode. In the

measuring volume, the reflection on the particle may become the dominant signal due to much higher light intensity. As discussed in section 3.5.2, a 70° scattering geometry is used in current setup. At this angle, the reflection light is not very strong. Thus, the dominant signal is the refractive light. The possible error which might occur is very small. The fourth factor which might affect the accuracy of the measurement is the environment temperature change in the heated vessel. The change of the temperature leads to the change of the refractive index. The calculation of the droplet diameter depends on the refractive index thus a shift of the refractive index might cause error on calculation. Section 3.5.2 discusses the sensitivity of the refractive index to the temperature and the sensitivity of the phase/drop size factor to the refractive index in details. It can be seen that the effect of the temperature change on the drop size measurement is within 1%.

3.6.3 Uncertainty of the Laminar Flame Measurement

Several factors may affect the laminar flame measurement: the initial temperature, the initial pressure, the purity of the fuel and the measurement of the flame radius from the images. In this study, the initial temperature is measured by a temperature sensor with an accuracy of 1°C . The initial pressure is kept 1 bar (0.1MPa) via connecting the vessel with ambient air before the test. The purities of the fuels are 99%, 99% and 99.9% for MF, DMF and isooctane, respectively. As described in Chapter 3.5.3, the laminar flame radii are measured from 4 directions of the flame to ensure the accuracy. Also, a repetition of 3 times is carried for each test and the averaged data is used for

further analysis. The root mean square deviation (RMSD) for different measurement is generally less than 2%. However, at some extreme test points, the RMSD could be 5% to 7%. As mentioned in chapter 3.5.3, due to non-spherical flame shape, the current calculated unstretched flame speed is around 1%-2% lower than it should be.

3.6.4 Uncertainty of the Turbulent Flame Measurement

The methods of the turbulent flame measurement, including the high speed imaging and the OH-LIF, are described in Chapter 3.5.4 and Chapter 3.5.5. The main factor which may affect the measurement of the turbulent flame properties is the cycle to cycle variation. In order to avoid the variation, 100 cycles of pressure data is recorded and used for the analysis. 30 cycles of combustion images are recorded at each test point and the averaged results are used in order to obtain the flame area, flame velocity. For the OH-LIF test, 200 images are record used for further analysis.

3.7 Summary

In summary, this chapter highlighted the experimental test facility and the relevant data processing methods used in this work. Firstly, the spray image acquisition system, including the constant volume vessel, the fuel injection system and the high speed CCD camera, was introduced. The second part introduced the PDPA system setup. Then the Schlieren test facility was presented. Following that, the single cylinder and the PLIF laser used in this work were described in detail. The fifth part introduced the data processing methods for the spray images, the PDPA results, the Schlieren images,

the engine combustion images and the OH-LIF images. The last part analyzed the possible experiment uncertainty which might occur in the study.

Chapter 4

Macroscopic Spray Characteristics

This chapter investigates the macroscopic spray characteristics of MF and DMF in comparison to ethanol, isooctane, and gasoline using high speed imaging. The effects of injection pressure, back pressure and ambient temperature on the spray penetration length (S) and spray cone angle (θ) are evaluated. Specifically, the flash boiling phenomenon of some of the fuels are discussed.

4.1 Introduction

The majority of the work in the direct-injection spray investigations published up to this present date are concerned with diesel injectors. Very few research investigations are about the gasoline direct-injection injectors, especially the multi-hole injectors. Thus the motivation of this work is to produce rare fundamental knowledge of the sensitivity of spray development of the multi-hole gasoline injector towards the change of the ambient conditions (injection pressure, back pressure and vessel temperature) and the fuels chemico-physical properties.

4.2 Test Conditions and the Properties of the Fuel

The test conditions are shown in table 4-1. Multiple factors are considered in order to gain a comprehensive understanding of the GDI multi-hole injector spray. The

bio-fuels, MF and DMF, are tested and compared with isooctane, ethanol and gasoline in order to understand the effect of the fuel properties on the spray. The injection pressures in this test are 50 bar, 100 bar and 150 bar, which are typical injection pressures for a GDI engine. The back pressures used in this test is 1 bar, 3 bar and 7 bar. The ambient temperatures (vessel temperature) are set to be 20°C, 60 °C and 90 °C. The injection duration for all the tests is 1 ms. The camera used here is the Phantom V710 camera.

Table 4-1: Test conditions for the high speed spray imaging test

Test Conditions	
Test fuels	MF, DMF, Isooctane, Ethanol, Gasoline
Injection pressures	50 bar, 100 bar, 150 bar
Back pressure	1 bar, 3 bar, 7 bar
Ambient temperatures	20°C, 60 °C, 90 °C
Fuel temperatures	20 °C,
Injection duration	1 ms
Camera setting	Phantom V710 @ 18,000 Hz
Camera Resolution	608x600 pixels

In order to discuss comprehensively on the spray characteristics, the fuel properties of the five fuels are presented in Table 4-2. Various chemico-physical properties of the fuels are included. These data will be referred in the following discussion.

Table 4-2 : Properties of the test fuels

	MF	DMF	ISO	Ethanol	Gasoline
Chemical formula					C ₂ -C ₁₄
H/C ratio	1.2	1.333	2.25	3	1.795
O/C ratio	0.2	0.167	0	0.5	0
Gravimetric oxygen content (%)	19.51	16.67	0	34.78	0
Density @ 20 C (kg/m ³)	913.2 ^b	889.7 ^a	691.9	789	744.6
Research Octane Number (RON)	103 ^b	101.3 ^c	100	108.6	96.8
Motor Octane Number (MON)	86 ^b	88.1 ^c	100	89.7	85.7
Stoichiometric air-fuel ratio	10.05	10.72	15.13	8.95	14.46
LHV (MJ/kg)	31.2 ^b	32.89 ^b	44.3	29.7	42.9
LHV (MJ/l)	28.5 ^b	29.3 ^a	30.66	23.43	31.9
Heat of vaporization (kJ/kg)	358.4 ^b	332	307.63	841	373
Initial boiling point (°C)	64.7 ^d	92 ^d	99 ^d	78.37 ^d	32.8
Surface tension@ 20 °C (N/m)	24.58*10 ⁻³ _d	26.02*10 ⁻³ _d	18.77*10 ⁻³ _d	24.04*10 ⁻³ _d	21.58*10 ⁻³ _d
Dynamic Viscosity@ 20°C (kg/m*s)	0.396*10 ⁻³ _d	0.515*10 ⁻³ _d	0.502*10 ⁻³ _d	1.18*10 ⁻³ _d	0.501*10 ⁻³ _d

a Measured at the University of Birmingham, 2010.

b NREL/TP-5400-50791. (Janet, 2011)

c (Wang, 2013)

d Yaws' Handbook of properties of the chemical elements (Yaws, 2011)

4.3 High Speed Imaging Results

The macroscopic spray characteristic, which is affected by many parameters including the ambient conditions, injector nozzle geometry, and the fuel properties, is important due to its guiding function to the engine combustion chamber design, engine calibration and validation of the engine modelling. The following sections present the analysis of the spray penetration and the spray cone angle under different test conditions.

4.3.1 Effect of Fuel

Figure 4-1 presents the spray images of the five fuels under 150 bar injection pressure at 1 ms ASOI. The first column of the images is taken under 20°C vessel temperature at back pressure of 1 bar. The second column of the images is taken under 20°C vessel temperature at back pressure of 7 bar. From these spray images, the general characteristics of the spray formation could be seen. At the nominally conditions (20°C ambient temperature, 1bar back pressure), the five fuels show similar spray forms. As the ambient pressure goes higher to 7 bar, their spray penetration lengths become shorter. The five fuels also exhibit similar form of spray at this condition as well.

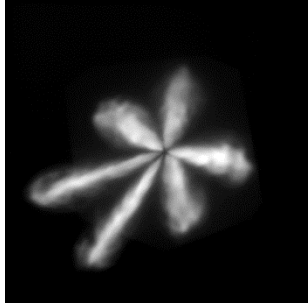
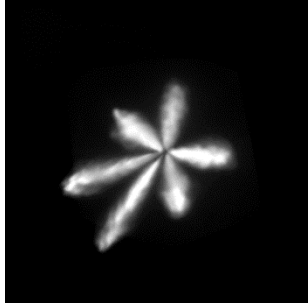
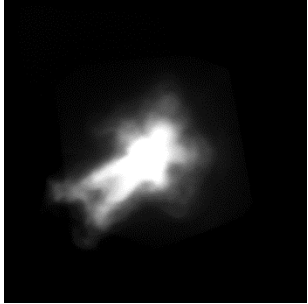
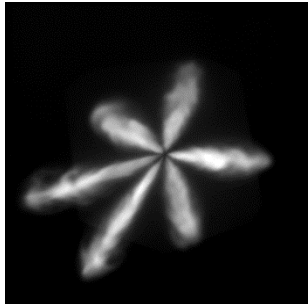
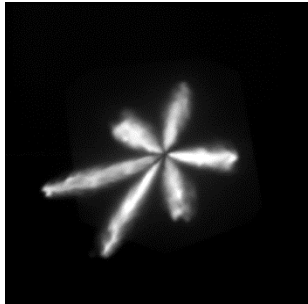
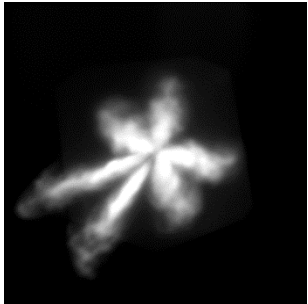
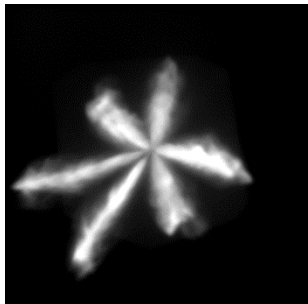
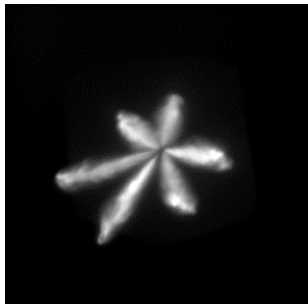
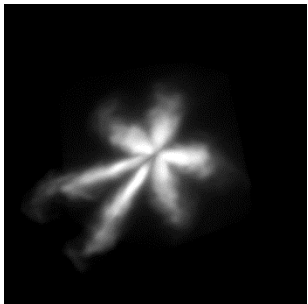
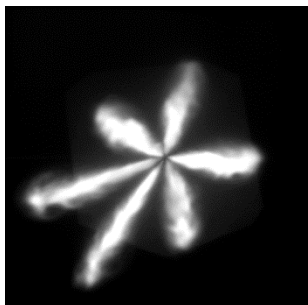
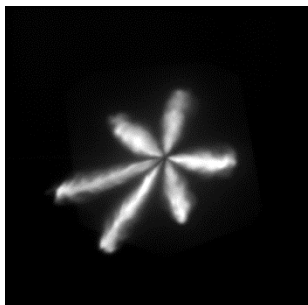
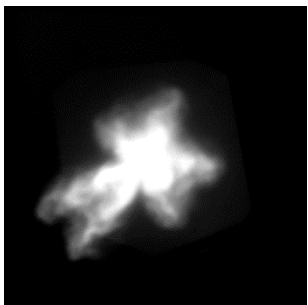
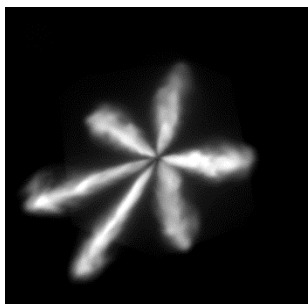
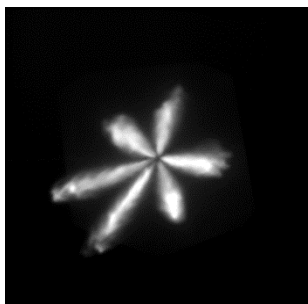
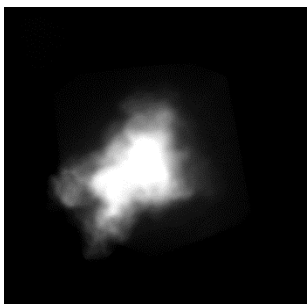
Fuels	1 bar	7 bar	90 °C
MF			
DMF			
ISO			
ETH			
Gasoline			

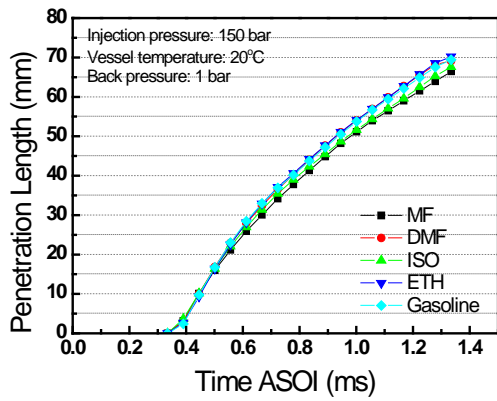
Figure 4-1: Spray of the five fuels under different ambient conditions (1ms ASOI).

Table 4-3: Vapour pressures of MF, DMF, Isooctane and Ethanol at different temperatures.

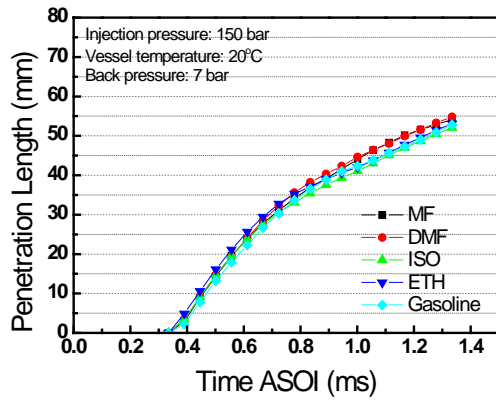
Vapor pressure (bar)	20 °C	60 °C	90 °C
MF	0.194	0.870	2.151
DMF	0.048	0.313	0.920
Isooctane	0.066	0.286	0.774
Ethanol	0.066	0.482	1.560

Data from: Yaws' Handbook of properties of the chemical elements (Yaws, 2011)

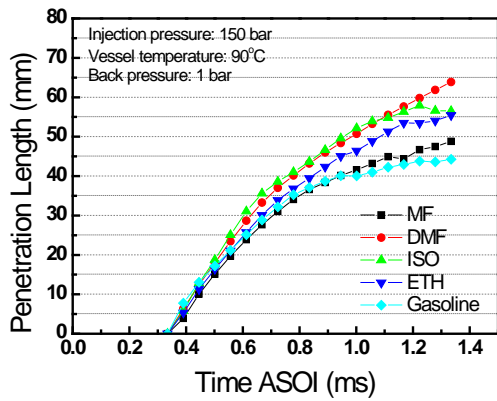
The third column in Figure 4-1 shows the spray images of the 5 fuels under vessel temperature of 90°C and back pressure of 1 bar. In order to understand the “collapse” of the spray forms, Table 4-3 presents the vapor pressures of different fuels at three temperatures. It could be seen that at 60°C, none of the fuels' vapor pressure is higher than the back pressure (1bar). When the temperature goes to 90°C, the vapor pressures of MF and ethanol are significantly higher than 1bar. Thus the “collapse” of the sprays of those two fuels could be expected. Also, it could be not that the vapor pressure of MF (2.151 bar) is higher than ethanol; therefore the “collapse” of MF is more severe than that of ethanol on the image. The vapor pressure of gasoline (produced by Shell) at 20°C is around 0.3 to 0.9 bar (Shell, 2011), which is much higher than any of the other 4 fuels. It could be reasonable deduced that gasoline has a much higher vapor pressure than other fuels at 90°C. Thus the “collapse” of gasoline is the most severe than the other fuel injections at 90°C, as shown in Figure 4-1.



(a)



(b)



(c)

Figure 4-2: Penetration length of different fuels under 150 bar injection pressure (a) ambient temperature 20°C, ambient pressure 1 bar (b) ambient temperature 20°C, ambient pressure 7 bar (c) ambient temperature 90°C, ambient pressure 1 bar

The fuel properties, including the density, viscosity, surface tension, boiling point and the latent heat etc., significantly affect the spray evolution. These parameters are closely related to the spray penetration length and the spray cone angle. Figure 4-2 shows the spray penetration of the five fuels under different conditions: (a) 150 bar injection pressure, 1 bar ambient pressure and 20°C ambient temperature (b) 150 bar injection pressure, 7 bar ambient pressure and 20°C ambient temperature (c) 150 bar injection pressure, 1 bar ambient pressure and 90°C ambient temperature. It can be seen from Figure 4-2 (a) that the spray penetration length of ethanol, DMF and

gasoline almost overlapped with each other (ethanol is a little higher than the other two). The penetration lengths of MF and isooctane were lower than the other three fuels. It appears that viscosity played a very important role regarding the penetration lengths of different fuels. The viscosity of MF was the smallest which means the MF liquid column could be easier to break up. Thus its penetration length was the shortest. Details about the droplet sizes of MF and other fuels can be found in chapter 5.

As the back pressure increased, a deceleration could be seen for all fuels at 0.8 ms after start of injection, as shown in Figure 4-2 (b). The final penetration (when the injection stopped at about 1.3 ms after start of injection) under 7 bar back pressure was 22%-24% shorter than the final penetration under 1 bar back pressure. In addition, the penetration lengths of different fuels behaved differently at a higher back pressure. The penetration lengths of MF and DMF were almost the same, having longer penetration lengths than that of isooctane, ethanol and gasoline. As the back pressure increased, the drag force from the air increased which caused deceleration. The penetration of the spray jet after SOI was mainly supported by the inertia of the fuel; fuel with higher density can penetrate longer than the others. Thus MF and DMF had longer penetration lengths under high back pressure conditions compared with other fuels.

When the ambient temperature was 20°C, the spray penetration lengths of all the five fuels were quite close. However, when the ambient temperature was elevated to 90°C, the differences between different fuels were dramatic. At a short period after the spray starts, the spray penetration lengths of the five fuels were quite close. After about 0.15

ms after the appearance of the spray, obvious divergence could be seen. Generally, the penetration length of MF was the longest, followed by isooctane and then ethanol; MF was shorter than these three and gasoline was the shortest. These trends resulting from the elevated temperature are associated with their boiling points. When the ambient temperature was higher than the boiling point of the fuel, the spray collapsed, meaning that the fuel column evaporated at the vicinity of the injector tip. That is why isooctane (boiling point 99°C) and MF (boiling point 92°C) had the longest penetration lengths, followed by ethanol (boiling point 78.4°C) and then MF (boiling point 64.7°C) and finally gasoline (boiling point 32.8°C).

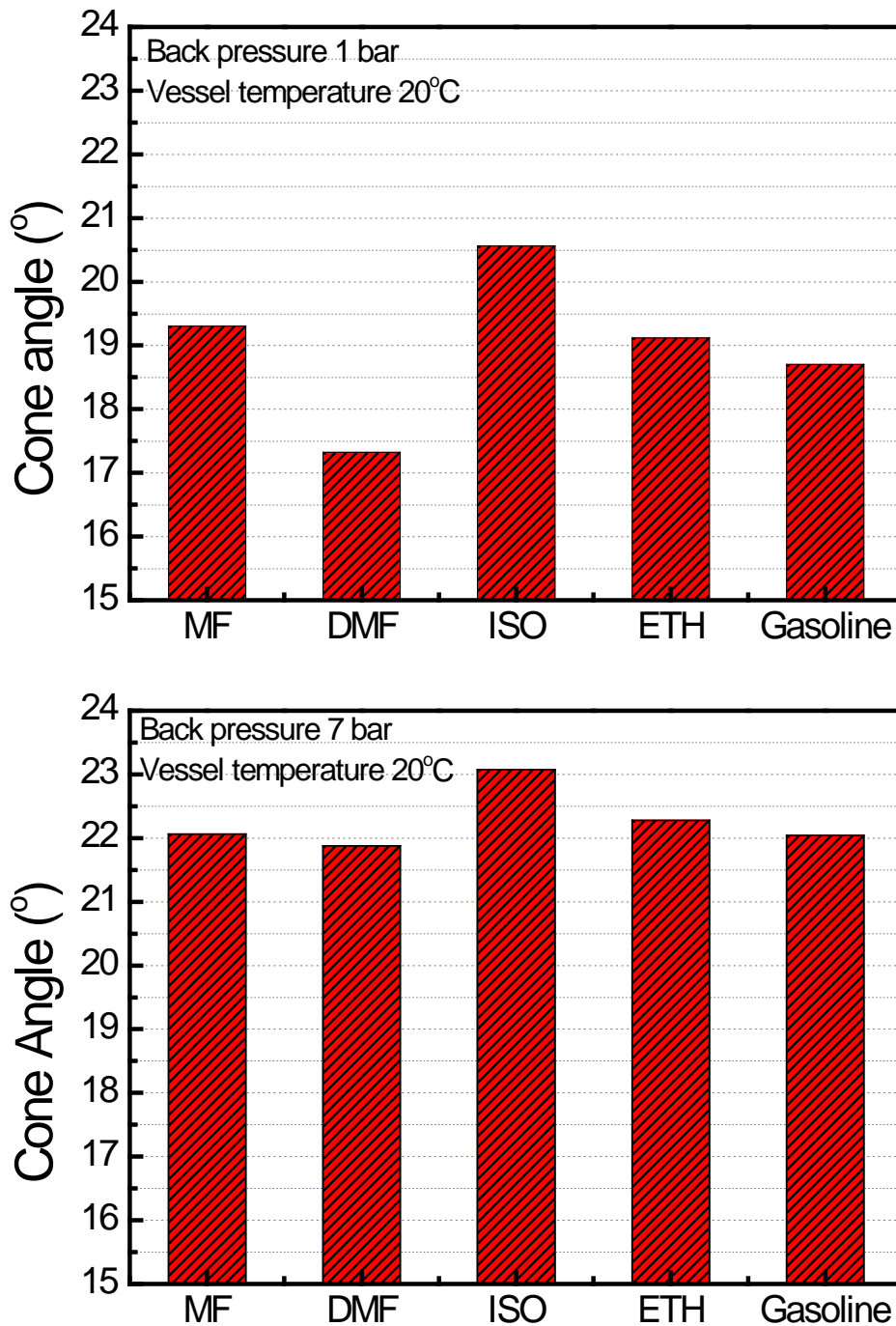


Figure 4-3 : Spray cone angle of different fuels under 150 bar injection pressure (a) ambient temperature 20°C, ambient pressure 1 bar (b) ambient temperature 20°C, ambient pressure 7 bar

Figure 4-3 shows the spray cone angle of different fuels at different ambient conditions. It can be clearly seen from Figure 4-3 (a) that isooctane had the biggest

spray cone angle followed by MF, ethanol and then gasoline. DMF had the smallest spray angle. This can be explained by their surface tension. Isooctane had the smallest surface tension at 20°C, whereas ethanol and MF were relatively larger. DMF had the highest surface tension. That is why isooctane had the largest spray cone angle whereas DMF had the smallest spray cone angle. Gasoline is a mixture of a wide range of hydrocarbon compounds, so it did not quite follow the trend of the single component fuels such as MF and DMF. When the back pressure increased from 1 bar to 7 bar, the spray cone angles of all the fuels increased as shown in Figure 4-3 (b). The density of the ambient gas increased as the pressure increases, and the increased density resulted in a higher drag on the spray which promoted the spray break up. Thus bigger spray cone angles were observed under higher back pressures. It is also noticed that when the back pressure was higher, the differences of the cone angles between DMF and other fuels became smaller.

4.3.2 Effect of Injection Pressure

Figure 4-4 presents the spray images of MF, DMF and gasoline under injection pressure of 50 bar, 100 bar and 150 bar. Generally, the sprays of the three fuels exhibit similar increasing trend when the injection increases. Also, it can be seen that the spray cone angles of the plumes increase with the increase of the injection pressure. The increased injection pressure promotes the increase of the penetration length and in the meantime improves the air/fuel mixture. Figure 4-5 shows the effect of injection pressure on the spray penetration of MF and DMF compared to gasoline at

equivalent injection pressures. From the statistical data, the influences of the changing injection pressure can be seen more clearly. For MF, DMF and gasoline, the effect of injection pressure on the penetration length was the same. At higher injection pressures, the penetration length was longer. The curves of the penetration lengths versus time of DMF at the three injection pressures (50 bar, 100 bar and 150 bar) were almost the same as those of gasoline. However, for MF, shorter penetration lengths were observed. This is mainly due to the difference in dynamic viscosity between MF and the other fuels. Gasoline and DMF have similar viscosities, which are 0.501×10^{-3} kg/m*s and 0.515×10^{-3} kg/m*s, respectively, whereas MF has a much smaller viscosity (0.396×10^{-3} kg/m*s). At 50 bar injection pressure, the penetration length of MF was similar to that of gasoline. This is because as the injection pressure was lowered; the deceleration of the fuel due to the drag force became obvious. As discussed before, fuel with higher inertia had a longer penetration length. Thus, under the combined effect of the dynamic viscosity and fuel density, the penetration length of MF at 50 bar had a similar penetration length compared to gasoline.

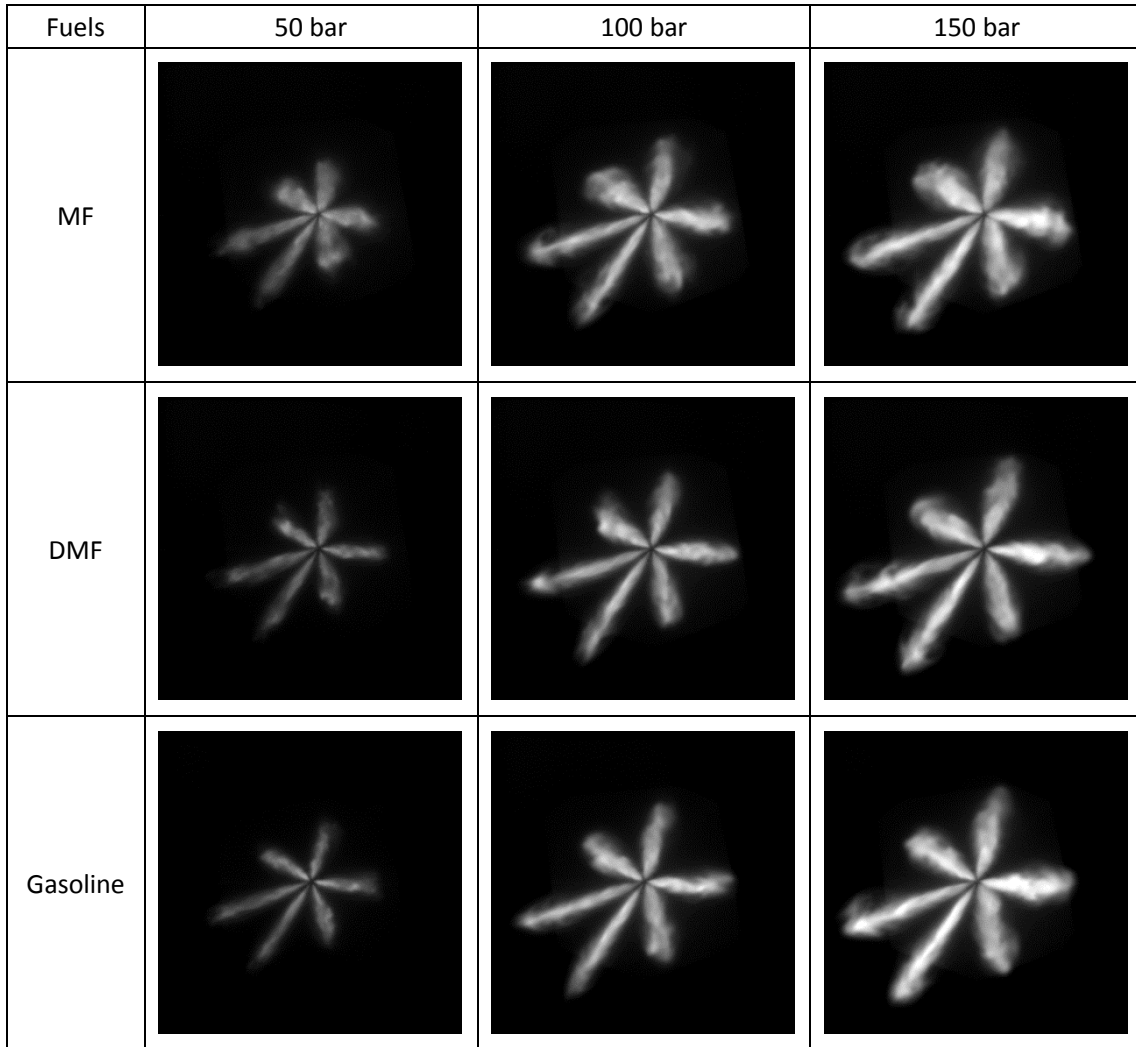


Figure 4-4: Spray of MF, DMF and gasoline under three injection pressures (1 ms ASOI)

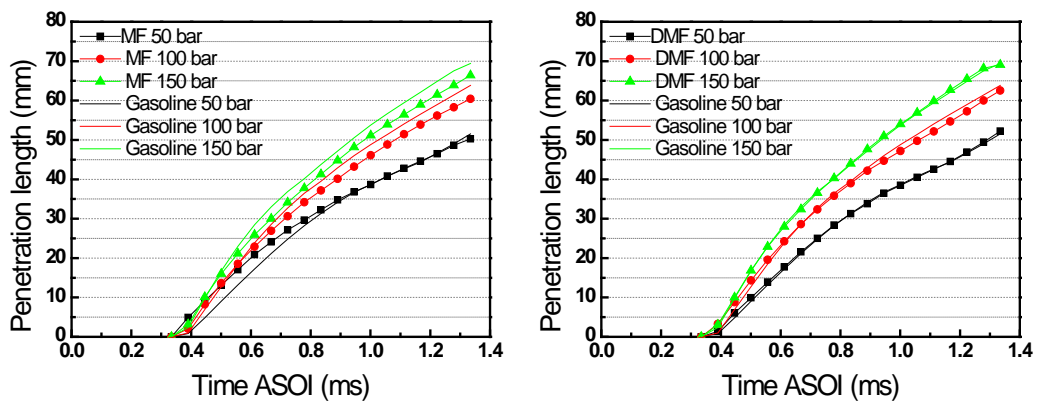


Figure 4-5: Penetration length of MF and DMF under different injection pressures compared with gasoline (ambient temperature 20°C, ambient pressure 1bar)

The spray cone angles of MF and DMF compared with gasoline under different injection pressures are shown in Figure 4-6. As the injection pressure increased, the spray cone angle increased due to better atomization of the spray. Almost all the spray cone angles were within the range of 15 to 20°. The differences between MF, DMF and gasoline were rather small. However, it still can be seen that the spray cone angles of MF were bigger than DMF and gasoline at the same injection pressures. DMF and gasoline had similar spray cone angles at the same conditions.

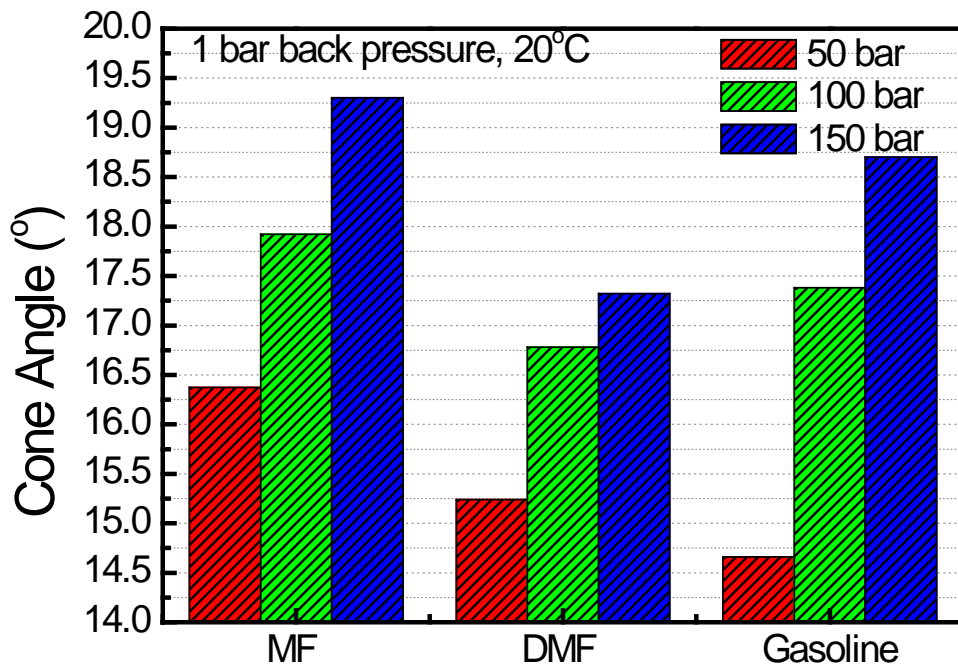


Figure 4-6: Spray cone angle of MF and DMF under different injection pressures compared with gasoline

4.3.3 Effect of Ambient Pressure

Figure 4-7 shows the spray images of MF, DMF and gasoline under different back pressures. With the increase of the back pressure, the spray plumes of the three fuels decrease due to the increased air drag force resulting from the increased air density. It can be seen that in terms of penetration length and spray cone angle, the three fuels are very similar under these three back pressures. However, it is very hard to judge whether there is any small difference between different sprays of the fuels. More details could only be found from the statistical data. The effects of the injection pressure on the spray penetration of MF and DMF compared to gasoline under 150 bar injection pressure are presented in Figure 4-8. For MF, DMF and gasoline, their spray penetration lengths decreased as the back pressure increased. The higher gas density applied higher drag on the spray. However, the behaviors of the fuel sprays towards the increased gas density were different. For MF, when the back pressure was 1 bar, its penetration length was lower than gasoline. When the back pressure was 3 bar, the penetration length of MF and gasoline were almost the same. As the back pressure further increased to 7 bar, the penetration length of MF was higher than that of gasoline under this condition.

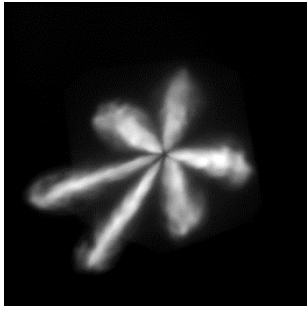
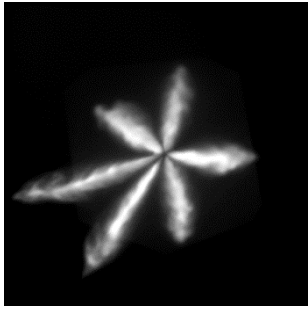
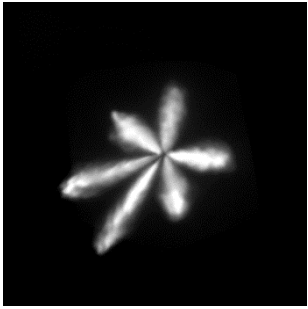
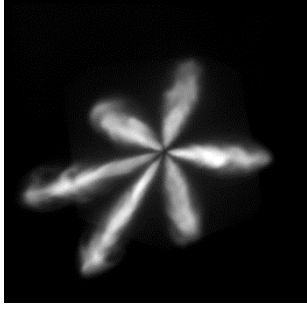
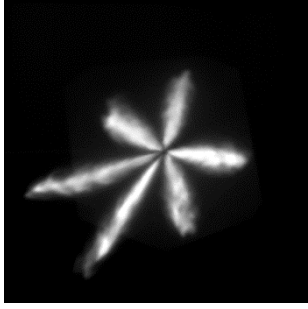
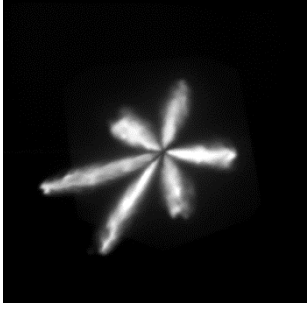
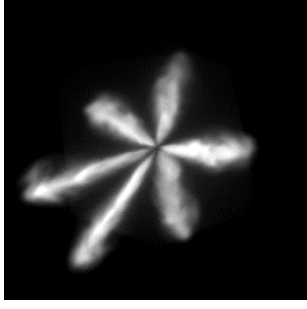
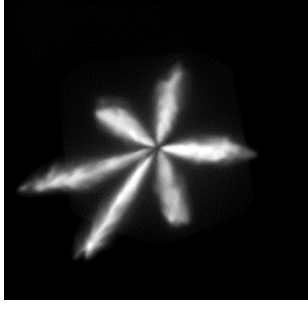
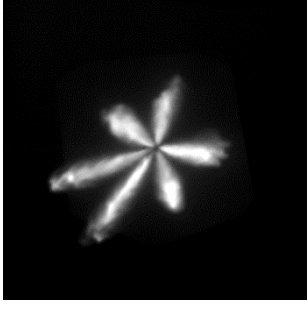
Fuels	1 bar	3 bar	7 bar
MF			
DMF			
Gasoline			

Figure 4-7: Spray images under different back pressure (1ms ASOI)

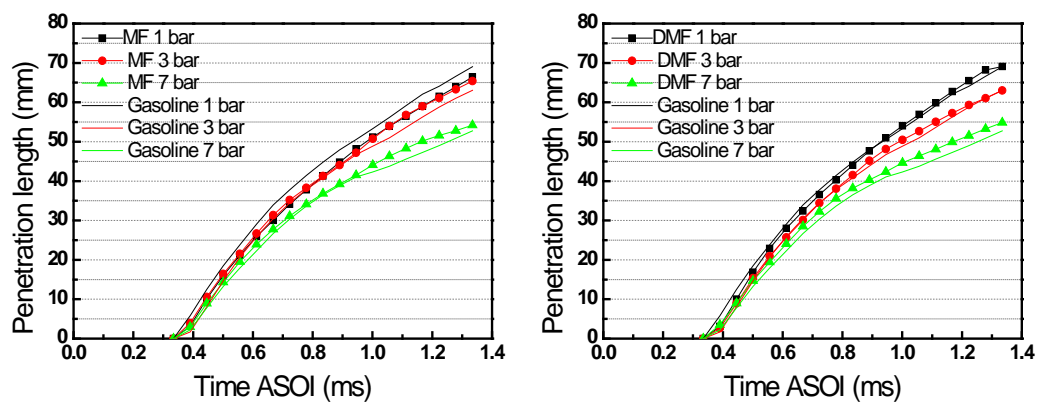


Figure 4-8: Penetration length of MF and DMF under different ambient pressures compared with gasoline (ambient temperature 20°C, injection pressure 150 bar)

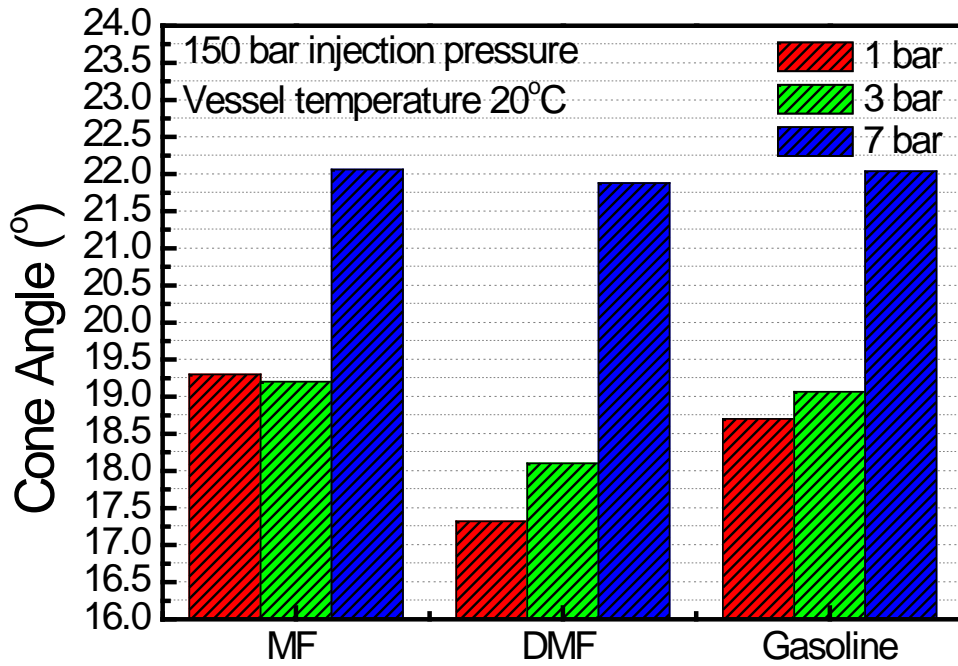


Figure 4-9: Spray cone angles of MF and DMF under different ambient pressures compared with gasoline

The Spray cone angles of MF and DMF under different ambient pressures compared to gasoline are shown in Figure 4-9. As the back pressure increased, the spray cone angles of the three fuels increased. As mentioned before, this was due to the higher drag of the air which promoted the break-up of the spray. At the back pressure of 1 bar, the differences between the cone angles of MF, DMF and gasoline were relatively higher. When the back pressure rose to 7 bar, the cone angles of three fuels become very close (almost all of them are 22°). At lower back pressures, the surface tension was playing an important role in affecting the cone angle. At higher back pressures, other properties, such as the viscosity and density, started to affect the cone angle.

4.3.4 Effect of Ambient Temperature

The penetration lengths and cone angles of MF, DMF and gasoline under elevated ambient temperatures (20°C, 60°C, 90°C) were also measured and compared to gasoline. Figure 4-10 shows the spray images of the three fuels at three ambient temperatures. With the vessel temperature increase from 20°C to 60°C, an increase on the cone angle could be observed. At this temperature, none of the sprays fully collapse because the temperature does not reach to the fuels' flash boiling point at this pressure (as shown in Table 4-3). Thus the penetration lengths of the three fuels are not significantly affected. When the vessel temperature increases to 90°C, the spray forms of MF and gasoline collapse while DMF still maintains its spray form due to its lower vapor pressure at this temperature. From the images, it could be seen that as the fuel spray collapse the 6 jets mixes together. The penetration length of the spray decrease dramatically. For DMF, the effect of the elevated temperature on the penetration length is not so significant in the absence of spray collapse.

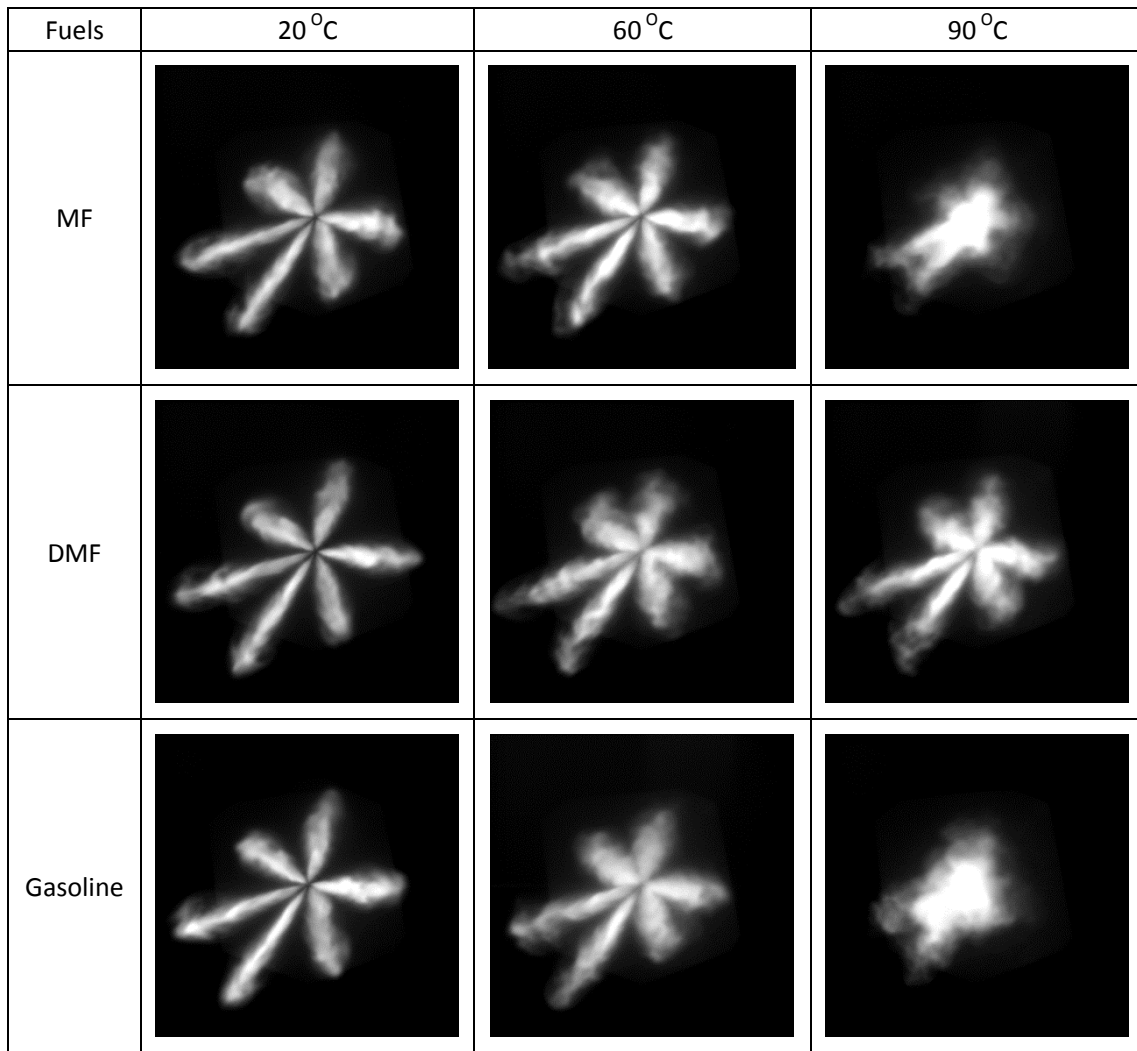


Figure 4-10: Spray images at different vessel temperatures (1 ms ASOI)

Figure 4-11 shows the penetration length of MF and DMF compared to gasoline under 1 bar ambient pressure and injection pressure of 150 bar. Generally, the increases of the temperature lead to a decrease of the penetration length. The increases might not be very significant. For example, the penetration lengths of MF under 20°C and 60°C ambient temperatures were almost the same and the penetration length of DMF under 60°C and 90°C ambient temperatures overlapped with each other. The same trend can be seen for gasoline spray penetration length under 20°C and 60°C ambient temperatures. However, when the temperature reached the boiling point of the fuel,

the spray collapsed which lead to a significant decrease of the spray penetration. The boiling points of MF and DMF are 64.7°C and 92°C, respectively, as shown in table 4-2. The spray of MF and gasoline collapsed at a temperature of 90°C and the spray of DMF did not collapse at any of the temperatures due to its high boiling point. As a result, the penetration length of MF and gasoline dramatically decreased when the ambient temperature reached 90°C. For DMF, the effect of the temperature on its penetration length was relatively quite small.

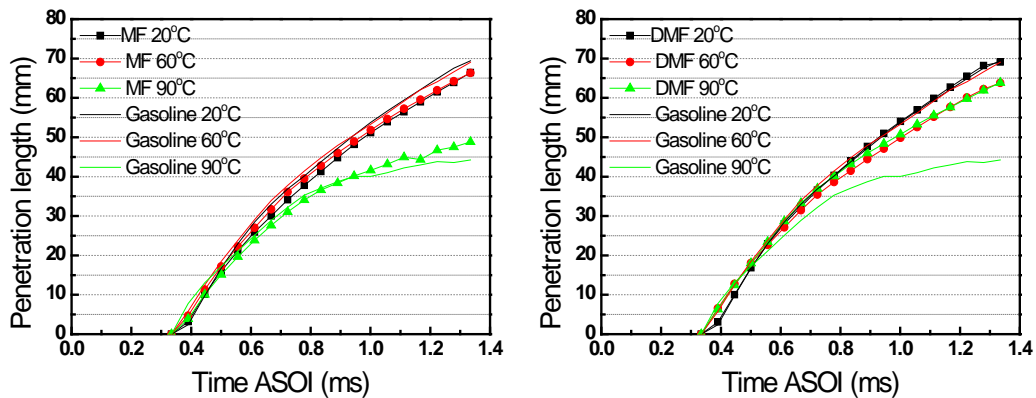


Figure 4-11: Penetration length of MF and DMF under different ambient temperatures compared with gasoline (ambient pressure 1 bar, injection pressure 150 bar)

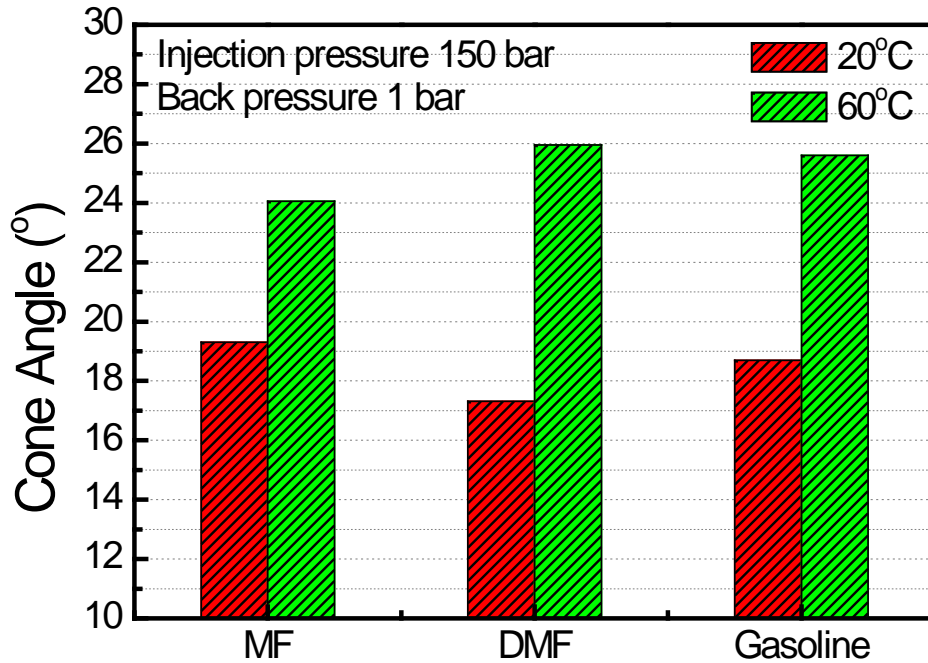


Figure 4-12: Spray cone angle of MF and DMF under different ambient temperatures compared with gasoline

The spray cone angles of MF and DMF under 20°C and 60°C temperatures at an ambient pressure of 1 bar and injection pressure of 150 bar are shown in Figure 4-12.

Due to the evaporation of the fuel sprays at 90°C, the sprays of the 6 jets overlapped with each other thus the measurement of the cone angle could not be conducted.

Therefore, only the data for 20°C and 60°C is given in this figure.

4.4 Summary

This chapter investigates the macroscopic spray characteristics of MF and DMF compared to ethanol, isooctane, and gasoline using high speed imaging. General observations of the spray images are presented. The penetration length and the spray cone angle are calculated. The following conclusions are drawn:

1. General observation:

- The five fuels show very similar spray form at the nominal conditions (150bar injection pressure, 20°C ambient temperature, 1bar back pressure). As back pressure goes up to 7bar, the spray jets become much shorter. Under ambient temperature of 60°C, the spray jets of all fuels exhibit wider spray cone angles. However, the penetration lengths are not significantly affected because there is no “spray collapse” at this ambient temperature. For MF, ethanol and gasoline, the spray forms have “collapsed” at ambient temperature of 90°C and back pressure of 1bar. For DMF and isooctane, there is no sign of spray collapse due to their lower vapour pressures.

2. Spray penetration and cone angle:

- When changing the ambient conditions, the order of the penetration lengths of the fuels could change dramatically due to their fuel properties which affect the penetration length. For example, at nominal conditions, the spray penetration lengths of DMF and gasoline are very similar. However, when the ambient temperature goes up to 90°C, the penetration length of DMF is much longer than that of gasoline due to the gasoline spray’s “spray collapse”.
- Compared to gasoline, MF has a shorter penetration length at different injection pressures (20°C ambient temperature, 1 bar back pressure) whereas the penetration length of DMF was almost the same as the penetration length of gasoline. This behavior occurred because DMF and gasoline have similar dynamic viscosities which are higher than that of MF.

- As the back pressure increased, the effect of the density became very important. Fuels with higher density, such as DMF and MF, had longer penetration lengths under high back pressures due to the higher momentum of the spray jet. The penetration length of MF was shorter than that of gasoline at an injection pressure of 150bar and a back pressure of 1bar. However, as the back pressure increased to 3bar and 7bar, the penetration length of MF was longer than that of gasoline due to its higher density.
- When the ambient temperature increase to 60°C, the penetration lengths of fuels (MF, DMF and gasoline) slightly decrease in the absence of “spray collapse”. As the ambient temperature further increase to 90°C, the collapse of the spray leads to dramatic decreases of the penetration length. At this ambient temperature, the sequence of the penetration length for the 5 fuels was the reverse sequence of their boiling point. The penetration length of a fuel at higher ambient temperature is highly affected by its boiling point.
- For single component fuels, surface tension plays an important role in affecting the spray cone angle. At the nominal conditions, isooctane had the biggest cone angle because it has the lowest surface tension. The cone angles of MF, ethanol and gasoline were quite close to each other and the cone angle of DMF was the smallest.

Chapter 5

Droplet Size and Velocity Measurement

The aim of this chapter is to evaluate atomization of the bio-fuels in terms of droplet size and velocities. Using PDPA, the effect of the measuring point, injection pressure, back pressure and ambient temperature on the droplet size and the droplet velocity are investigated.

5.1 Introduction

A bio-fuel's potential to be used on a vehicle's engine is largely determined by its properties. Among these properties, the atomization characteristics are very important as they directly affect the combustion of a fuel in the engine. A previous study (Tian, 2010a) has revealed the atomization characteristics of DMF and its blends under 1 bar ambient pressure. Some other studies have also been carried out to investigate the atomization of other bio-fuels (Aleiferis, 2013, Gao, 2007 and He, 2008). However, the atomization of MF and DMF under varied back pressure and ambient pressure has not been fully studied. This work studies the atomization of MF and DMF under various conditions. The comparisons of different bio-fuels and the benchmark gasoline are also given in terms of droplet size and droplet velocity. In order to support the discussion, the histogram of the droplet distribution, the Weber number, the Reynolds number and the Ohnesorge number are also presented.

5.2 Test Conditions and calculation of

5.2.1 Test conditions

The test conditions of the PDPA test in this study are shown in Table 1. The test was performed under different injection pressures, back pressures and different ambient temperatures. Measurements were taken at 30mm, 40mm, 50mm and 60mm distance from the injector tip, because the liquid column does not yet fully break up at the 20mm position. At each position, the measurement would terminate when either the measurement time reaches 90 seconds or 50,000 droplets are acquired.

Table 5-1: Test conditions for PDPA test

Test Conditions	
Test fuels	MF, DMF, Isooctane, Ethanol, Gasoline
Injection pressures	50 bar, 100 bar, 150 bar
Back pressures	1 bar, 3 bar, 7 bar
Ambient temperatures	20°C, 60 °C, 90 °C
Injection duration	1 ms
Measuring points	30mm, 40mm, 50mm, 60mm from the nozzle

5.2.2 Calculation of the non-dimensional numbers

The Weber number is calculated from formula $W_b = \rho u^2 d / \delta$; the Reynolds number is calculated from formula $Re = \rho u d / \mu$ and the Ohnesorge number is calculated from $Oh = We^{1/2} / Re$. Detailed description on the formulas of the three non-dimensional numbers can be found in Chapter 2.3.1. In this study, the jet velocity (u) at the exit of the nozzle is calculated from the high speed imaging data. It is assumed that the droplet diameter (d) at the exit of the nozzle equals to the nozzle diameter and the nozzle diameter for the GDI injector used in this study is 0.2 mm. The other parameters including the liquid density (ρ), surface tension (δ) and the dynamic

viscosity (μ) can be found in Table 4-2.

5.3 Results and Discussion

5.3.1 Spray Structure against Time

Typical diagrams of the droplet diameter and velocity distribution against time are shown in Figure 5-1. The measurement is made under ambient temperature (20°C) and pressure conditions using gasoline under 150 bar injection pressure (nominal conditions). An injection duration of 1 ms is chosen and the measurement is carried out at a distance of 40 mm from the injector nozzle. After the injection, the spray reached the measuring point of the PDPA system after a short period of time. This time is called the injection delay and it is the sum of the solenoid delay of the injector and the spray travelling time. In order to compare the differences of different fuels under different conditions, the averaged droplet diameter and velocity line are used here by deducing the mean diameter and velocity of all the droplets in every time bin of 0.1 ms. The evolution of the droplet diameter and the velocity are clearly shown by the average velocity lines. All the analysis on droplet velocity in this chapter will be presented in the form of average velocity.

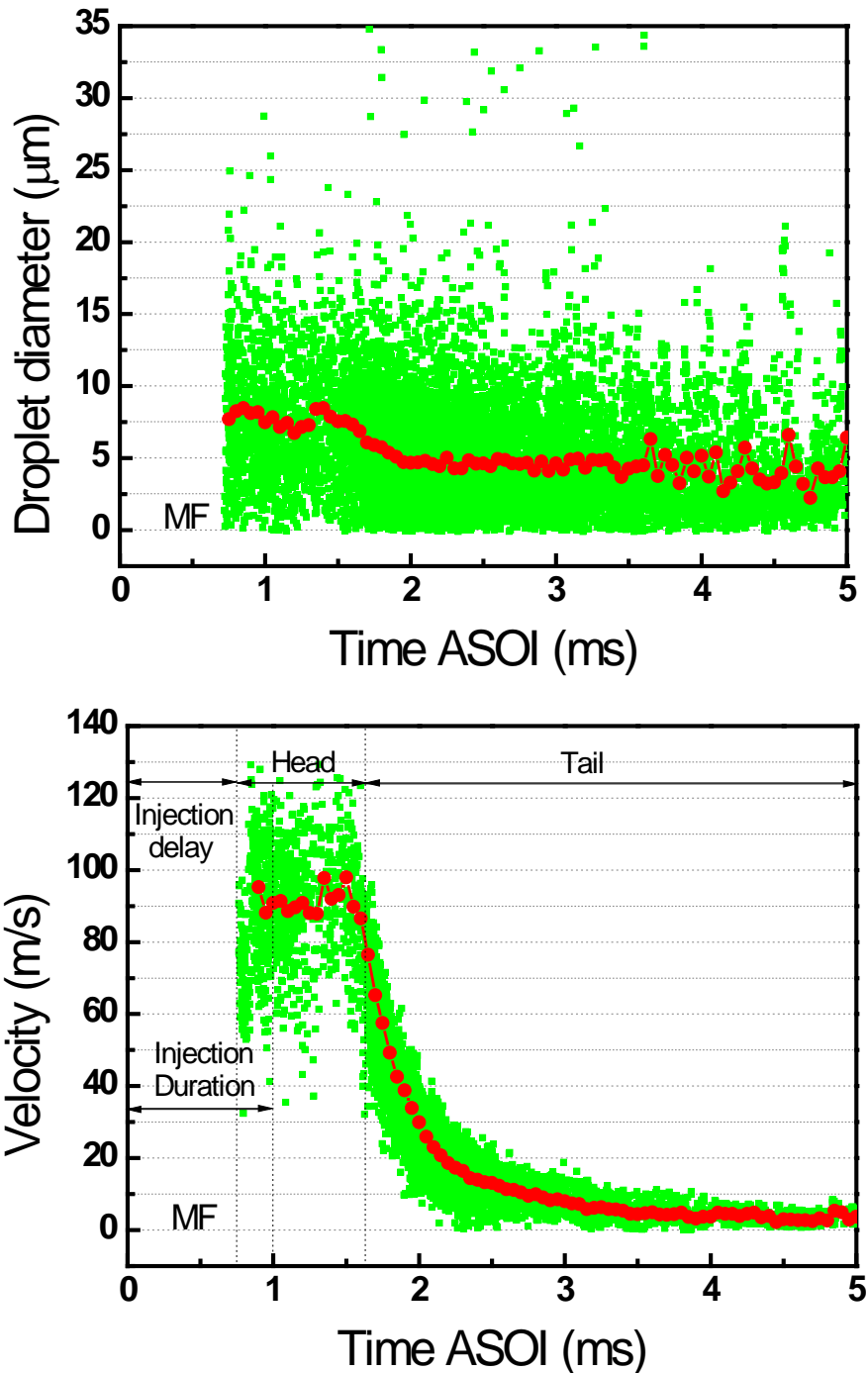


Figure 5-1: Droplet diameter and velocity of MF against time at ambient conditions and an injection pressure of 150 bar (40 mm from the nozzle)

5.3.2 Effect of Axial Position on SMD and Velocity

For each fuel under one test condition, the measurement of the SMD and the droplet velocity are taken at four different positions. Figure 5-2 shows the SMD and the mean velocity of a gasoline injection at 150 bar injection pressure and 1 bar ambient

pressure under the ambient temperature of 20°C. The SMD value of gasoline increases as the measuring point moves downwards, as shown in the figure. This is due to the evaporation of the small droplets during the movement of the spray. After the break-up of the liquid fuel, a large amount of droplets with different sizes are generated. It should be noted that it is easier for small droplets to evaporate than big droplets. Therefore, after the small droplets “disappear”, the mean diameter size would increase. A similar trend can be observed for the measurements of all the fuels in this study.

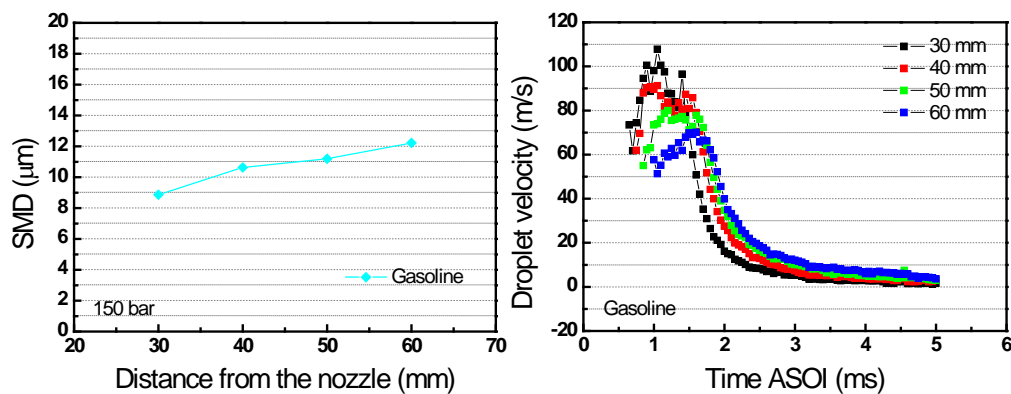


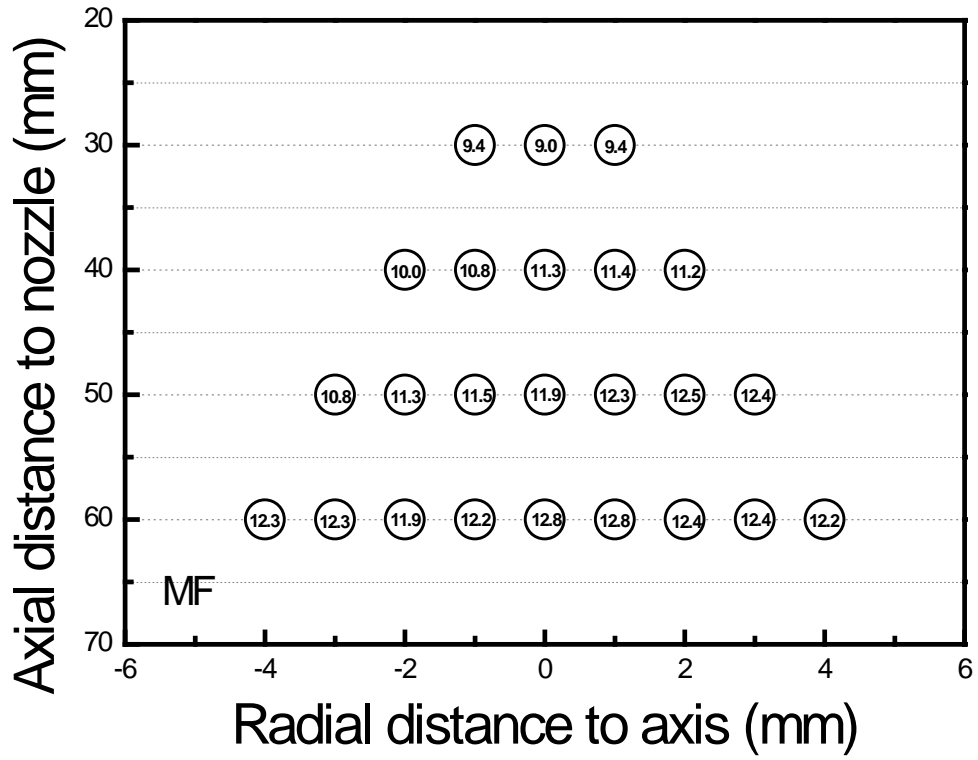
Figure 5-2: The SMD and mean velocity of gasoline at different positions.

Differences can be observed amongst the velocities measured at different positions, as shown in Figure 5-2. The maximum velocity on the average velocity line decreases as the measuring point moves downwards (from 30mm to 60mm). The maximum velocity measured at 30 mm distance from the nozzle is about 100 m/s whereas the maximum velocity measured at 60 mm distance from the nozzle is about 70 m/s. This trend is due to the deceleration of the droplets caused by the drag force from the ambient air. In the meantime, the time between the injection and the maximum

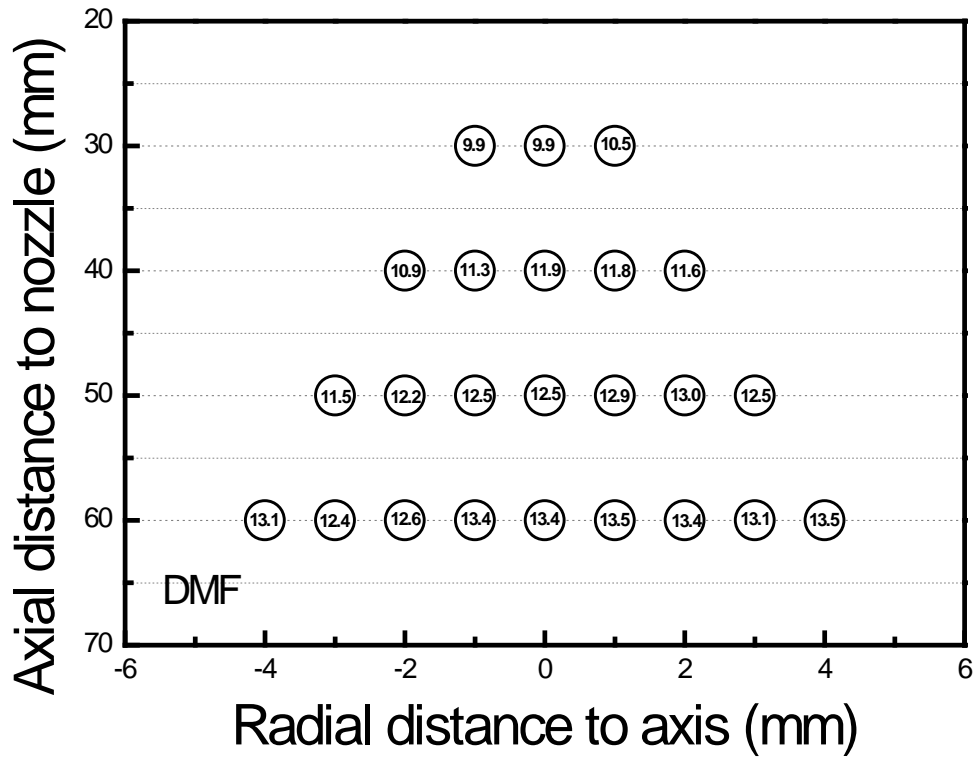
velocity point increase when the measuring point goes down. On the tail, the delay can also be clearly seen. In this study, in order to compare the droplet velocity of different fuels, only the droplet velocity at the position of 40 mm would be used. At this point, the break-up process is almost finished for all fuels.

5.3.3 Droplet Distribution (SMD distribution)

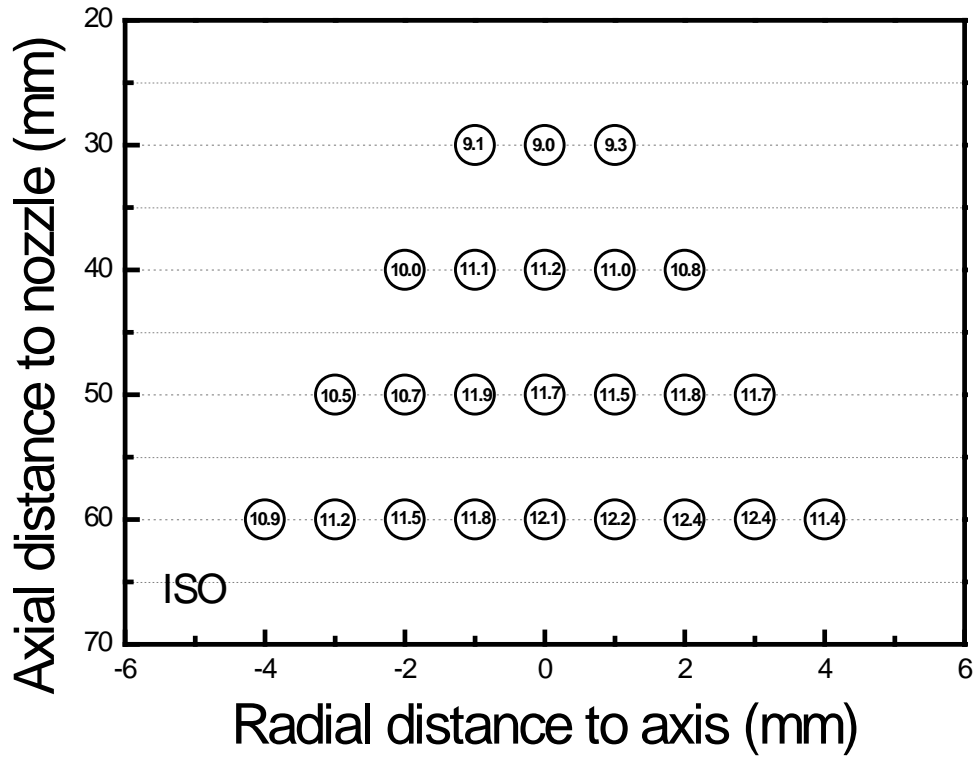
The SMD maps of all the tested fuels across the spray are shown in Figure 5-3. Droplet sizes of different axial (from 30 mm to 60 mm) and radial (from -4 mm to 4 mm relative to the jet center) positions are shown in the circles with the unit of μm . The range of the droplet size is within $8\mu\text{m}$ to $15\mu\text{m}$ and the droplet sizes generally show good symmetry along the axis for all the fuels. The droplet size in the centre is generally larger than the droplet size on the edge, due to the break-up and evaporation process. A similar trend can be found in the literature (Tian, 2010a). From the maps, it can be observed that the SMD value of ethanol is the largest and gasoline is the smallest. Other fuels also exhibit differently in terms of droplet size; detailed analysis will be given in following sections.



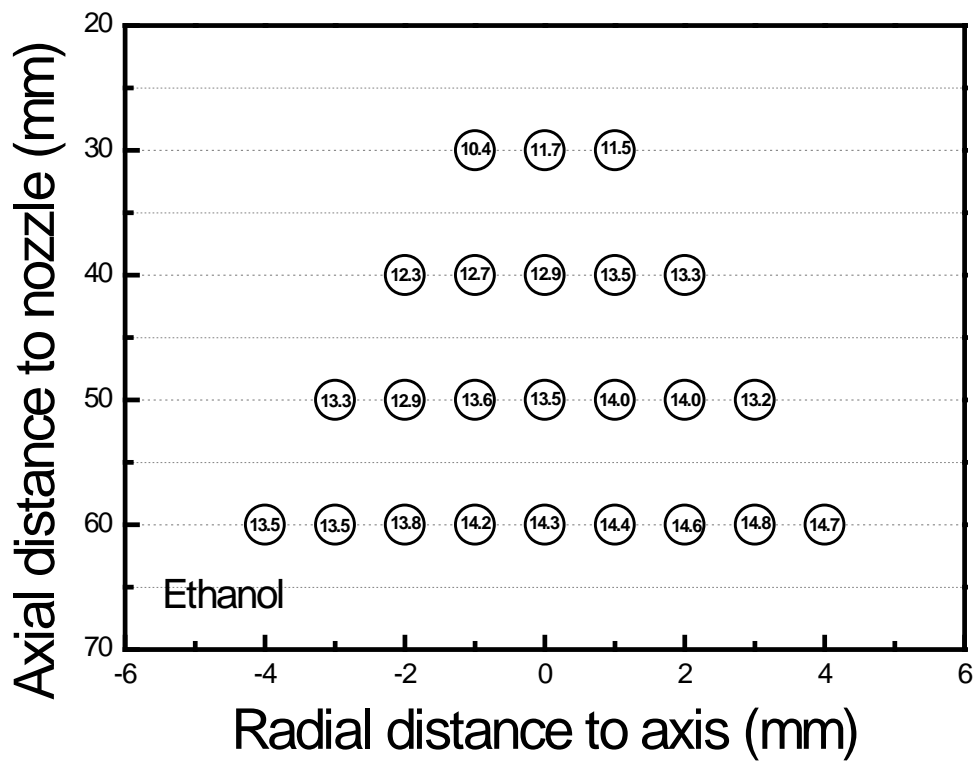
(a)



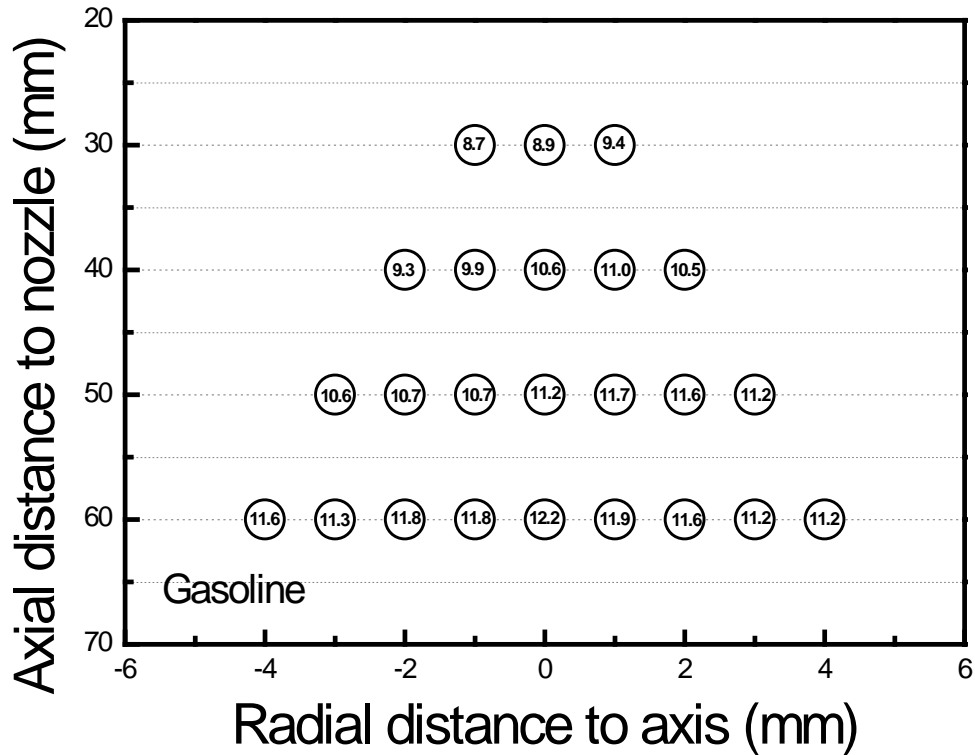
(b)



(c)



(d)



(e)

Figure 5-3: SMD values of the tested fuels throughout the spray (Test conditions: 150 bar injection pressure, 1 bar back pressure, 20°C vessel temperature)

5.3.4 The Differences of the Fuels

Figure 5-4 shows the SMD and development of the droplet velocity of different fuels under 150 bar injection pressure and 1 bar back pressure and vessel temperature of 20 °C. Ethanol exhibits the largest SMD at almost all positions, followed by DMF, MF and then isooctane. Gasoline has the smallest SMD compared to other fuels. In contrast, the development of the droplet velocity shows totally different trend. MF, DMF and isooctane almost have overlapping droplet velocity curves. The droplet velocity of gasoline is lower than these three and ethanol has the lowest droplet velocity. At this test condition, the SMD of ethanol is about 16%-21% larger than the gasoline and its droplet velocity is about 20% lower than the gasoline at the head

part. The SMD of MF and DMF are about 6% and 11% larger than that of gasoline after axial position of 30 mm.

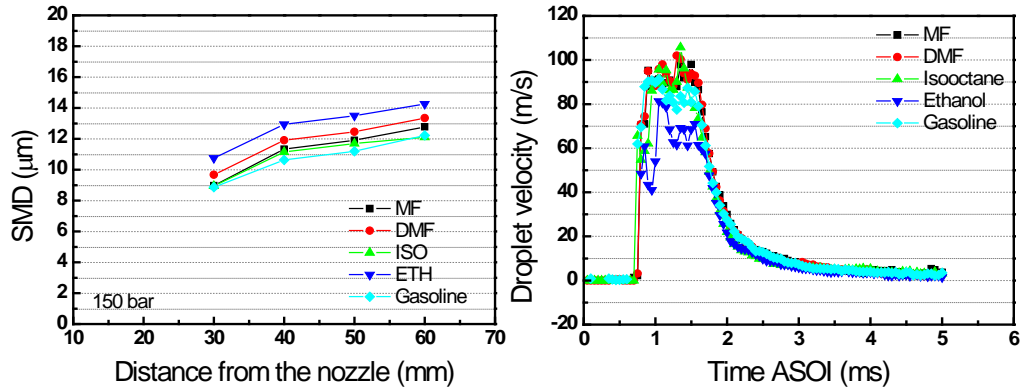


Figure 5-4: SMD values and droplet velocity (40 mm from the nozzle) of the five fuels under 150 bar injection pressure, 1 bar back pressure and vessel temperature of 20 °C (nominal conditions).

Figure 5-5 presents the Reynolds number and the Weber number for the injection of all the fuels under the same condition as Figure 5-4. For ethanol injection, both its Weber number and Reynolds number are the smallest compared to the other fuels. It means that the forces which break the droplet up are relatively small. It can be inferred that the droplet size of ethanol should be the largest amongst the five fuels. This inference is in agreement with the test results shown in Figure 5-5, in which ethanol spray has the largest droplet size.

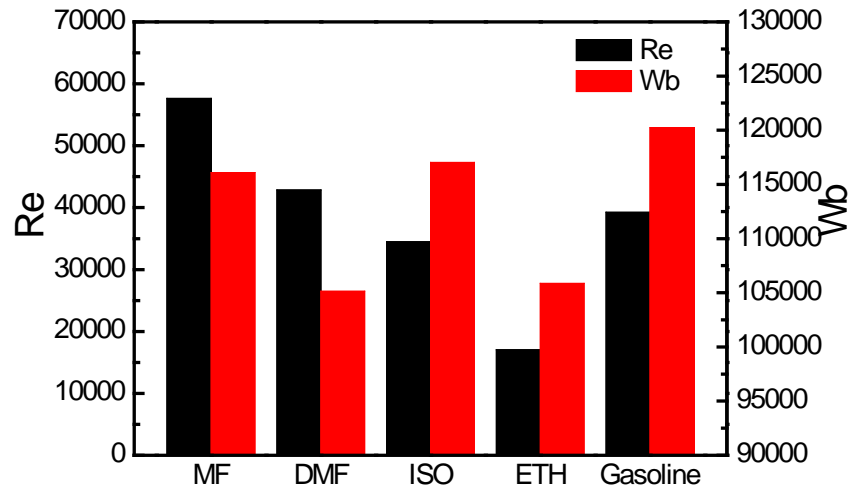


Figure 5-5: Reynolds number and Weber number of MF and DMF at nominal conditions

As for the other fuels, the Weber number of DMF injection is as small as ethanol injection even though its Reynolds number is higher; this could be the reason that DMF injection has the second largest SMD, as shown in Figure 5-4. The Weber number of MF injection is larger than that of DMF and ethanol and smaller than that of gasoline and isooctane. This gives MF the SMD values which are smaller than those of DMF and ethanol and bigger than those of gasoline and isooctane. The main dominant factor is the Weber number in this condition. When the Weber number is higher, the fuel would have small SMD values regardless of the Reynolds number. However, if the Weber number is similar, the injection with the larger Reynolds number would have small SMD values.

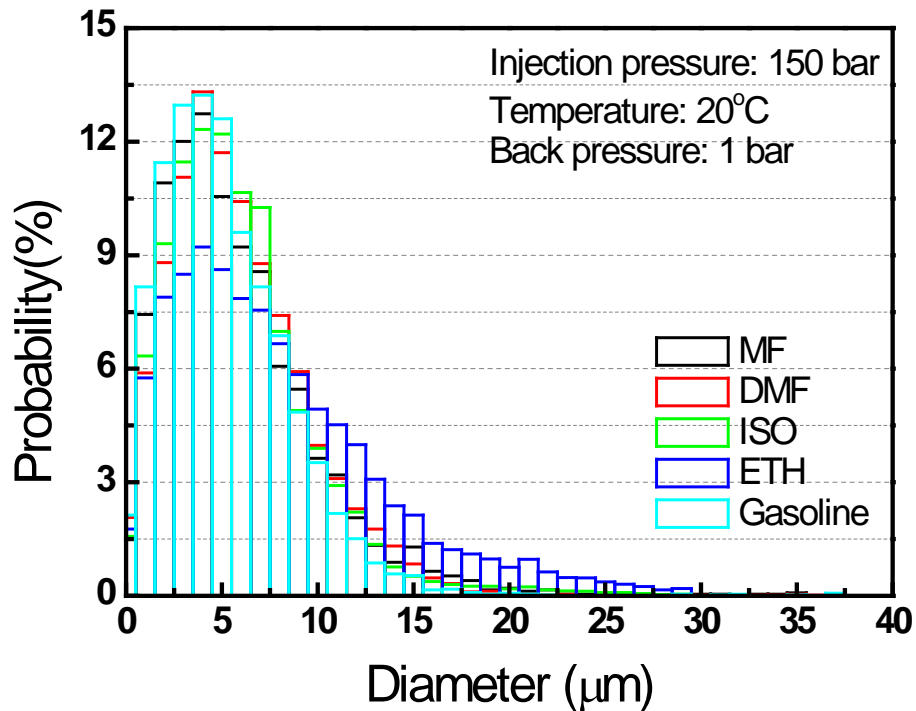


Figure 5-6: Histogram of the five fuels at nominal conditions (40 mm from the nozzle)

The histogram for droplet sizes of different fuels at nominal conditions is shown in Figure 5-6. It is not surprising that ethanol has the highest percentages of big droplets. This shows accordance with the SMD values in Figure 5-4. Some differences are also observed amongst the fuels. DMF shows a slightly higher probability between droplet size of 10 μ m and 20 μ m. Gasoline has higher proportion of small droplets. That is why the SMD values of DMF are the second highest and the SMD values of gasoline are the lowest.

5.3.5 Effect of the Injection Pressure

In this section, the effects of injection pressure on SMD and droplet velocities are studied. Figure 5-7 shows the SMDs and droplet velocities of MF and DMF under three injection pressures (50 bar, 100 bar, 150 bar) and vessel temperature 20°C. As

the injection pressure increases, a significant drop in the droplet size can be observed. The direct effect of the injection pressure increase is the increase of the exit velocities of the spray jet. The higher exit velocities create a stronger interaction between the fuel jet and the surrounding air, which enables better break-up of the fuel droplets. The droplet velocities prove this from another aspect: compared with the SMD value, the droplet velocity shows the reverse trend in that the droplet velocity increases dramatically as the injection pressure increases. This is due to the larger drag force resulting from the higher air density.

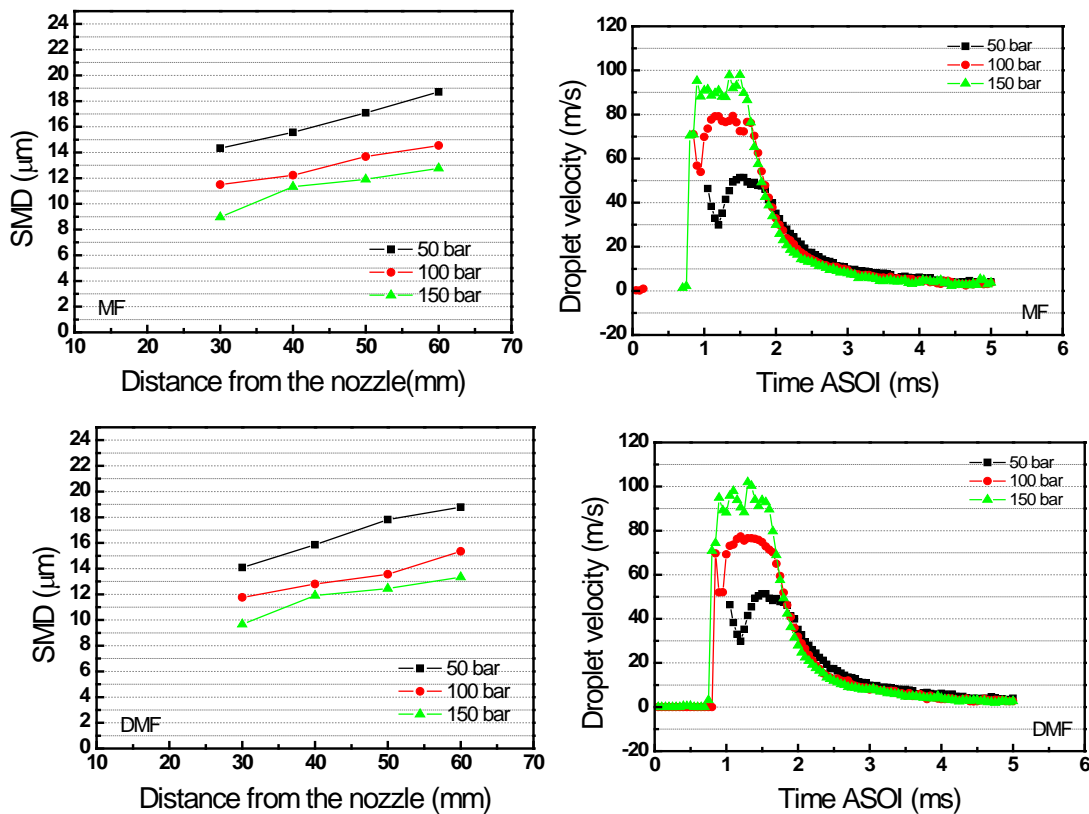


Figure 5-7: SMD values and droplet velocity of MF and DMF under three injection pressures, 1 bar back pressure and vessel temperature of 20 °C

The Reynolds number and the Weber number of both fuel injections are shown in Figure 5-8; both of them increase as the injection pressure increases. This indicates that the inertial and external forces, which promote the break-up of the spray, increase

with the increase of the injection pressure. This is in accordance with the observation of the SMD values in Figure 5-7. It can also be seen from Figure 5-7 that the SMD values of MF are smaller than those of DMF under all injection pressures. This is due to MF injection having a higher Reynolds number and higher Weber number, which leads to better atomization. It can also be noticed that the Reynolds number and Weber number of MF injection are higher than those of DMF at all injection pressures. This should be the main reason that MF has smaller SMD than DMF.

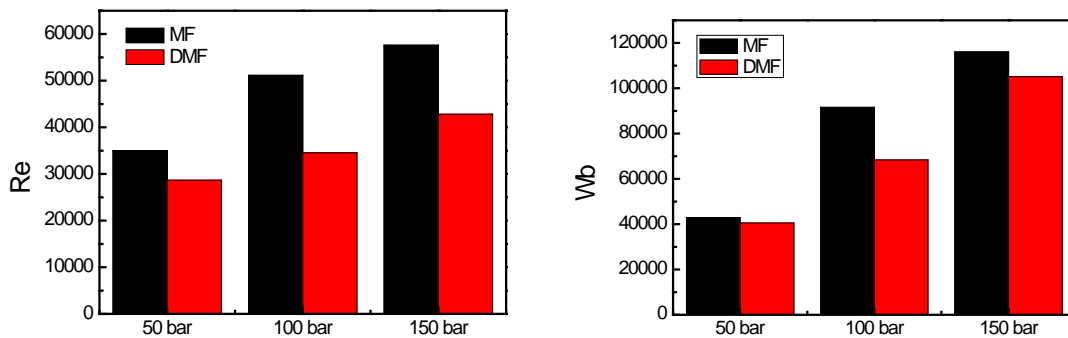


Figure 5-8: Reynolds number and Weber number of MF and DMF injection at different injection pressures

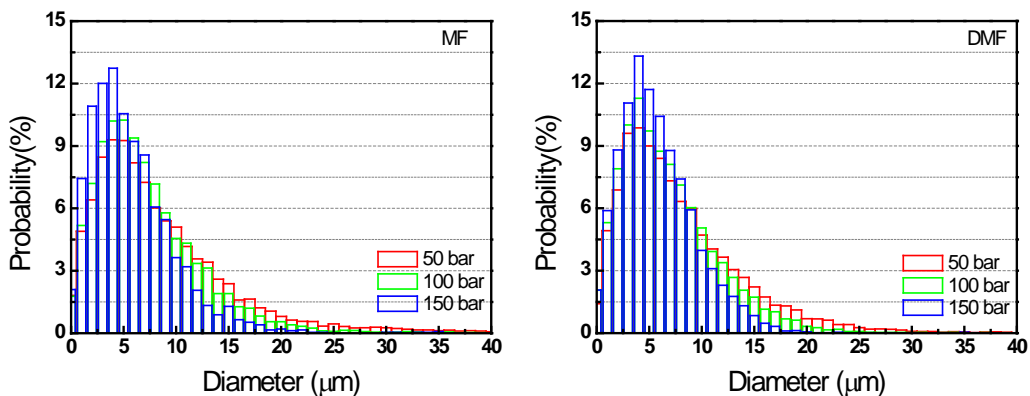


Figure 5-9: Histogram of MF and DMF at different injection pressures (40 mm from the nozzle)

As shown in Figure 5-9, the effect of the injection pressures on MF and DMF injection are similar. With a higher injection pressure applied on the liquid fuels, the

percentage of the small droplets increase while the percentages of the big droplets decrease significantly. This is because that high injection pressures lead to higher exit velocity of the liquid columns. Thus the big droplets in both fuels have more chances to break-up into small droplets.

Figure 5-10 exhibits the SMD values and droplet velocities of different fuels under 50 bar injection pressure. The SMD values exhibit differently under this low injection pressure compared to the SMD values at an injection pressure of 150 bar. Although ethanol still has the biggest SMD values under both injection pressures, the contrasts of other fuels are not so clear at lower injection pressures (50 bar) as it is at high injection pressure (150 bar). In general, the SMD values of ethanol are the highest along the axle, followed by gasoline and then DMF, isooctane and MF. This can be explained by the corresponding Reynolds numbers and Weber numbers. As shown in Figure 5-11, isooctane injection has the highest Weber number while the rest of the fuels have similar Weber numbers at an injection pressure of 50 bar. As for Reynolds number, MF injection is the highest, followed by DMF, isooctane and then ethanol. The Reynolds number of gasoline injection is close to that of isooctane injection. It should be noted that the Reynolds number of MF injection is 3.5 times as big as the Reynolds number of ethanol injection. The simplest deduction from the order of the Reynolds numbers and the Weber numbers is that ethanol spray would have the largest mean droplet size amongst the fuels because of its low level of the Reynolds number and its average level of Weber number. This is verified by the test result in Figure 5-4. The reason that MF has the lowest SMD values is that the Reynolds

number of MF injection is the highest and the Weber number is not low. Isooctane injection has the second lowest SMD values even though its Reynolds number is not high; this is mainly due to its high Weber number. Therefore, it can be concluded that when the injection pressure is low, both the Reynolds number and the Weber number are affecting the SMD values. Neither of them is the dominant factor. In order to make the statement more clearly, the discussion is summarized in Table 5-2.

Table 5-2: Summary of the trends for Wb, Re, and SMD values at 50 bar and 150 bar injection pressure

Injection pressure	Wb number and Re number		SMD	Explanation
High (150 bar)	Wb	Gasoline>ISO>MF>ETH≈DMF	ETH>DMF>MF>ISO>Gasoline	At high injection pressure, Wb is playing a more important role than Re
	Re	MF>DMF>Gasoline>ISO>ETH		
Low (50 bar)	Wb	ISO>ETH≈MF>DMF≈Gasoline	ETH>Gasoline>DMF>ISO>MF	At lower injection pressure, both Wb and Re are important to the droplet size.
	Re	MF>DMF>ISO≈Gasoline>ETH		

The peak droplet velocities of the five fuels fall from the range of 90 m/s to the range of 50 m/s as the injection pressure drops from 150 bar to 50 bar. Moreover, for the five fuels, their droplet velocity diagrams almost overlap with each other. It seems that the fuel properties are not the main factors which determine the droplet velocities under low injection pressure.

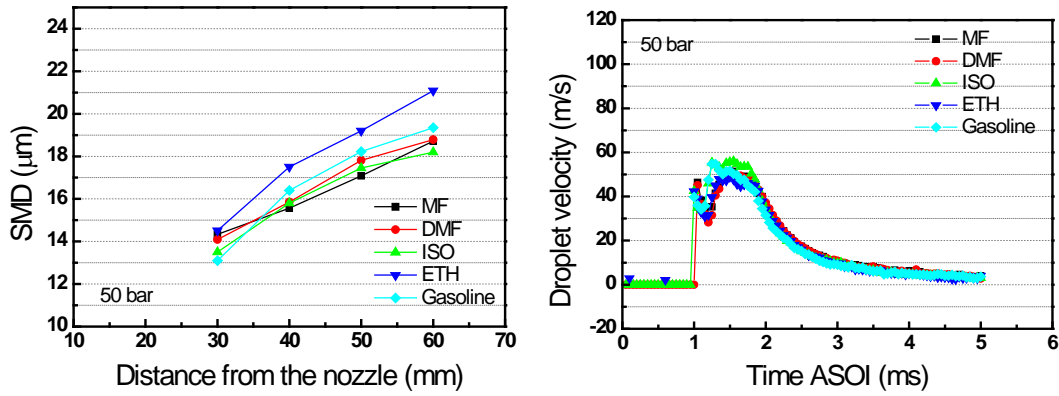


Figure 5-10: SMD values and droplet velocities of the five fuels under 50 bar injection pressures, 1 bar back pressure and vessel temperature of 20 °C.

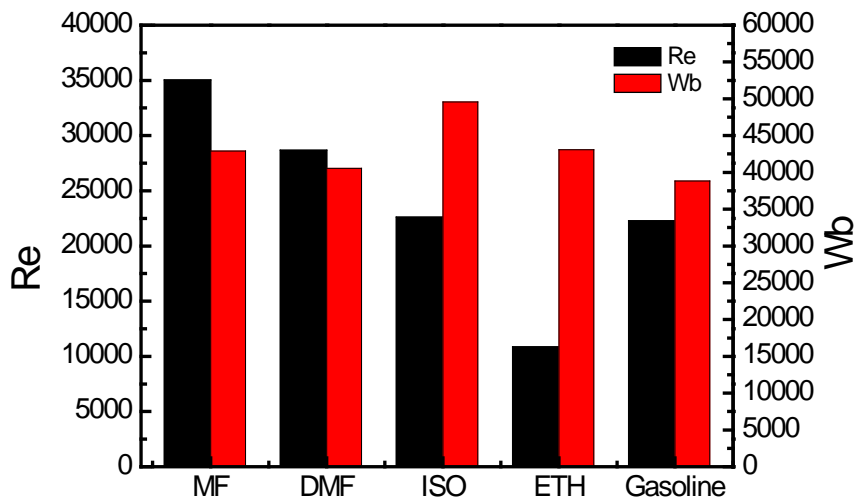


Figure 5-11: Reynolds number and Weber number of the fuel injections at injection pressure of 50 bar

5.3.6 Effect of the back pressure

Figure 5-12 shows the SMD and droplet velocities of MF and DMF spray under three back pressures (1 bar, 3 bar, 7 bar). It can be seen that back pressure has a significant effect on both the droplet size and the droplet velocities. With the increase of the back pressure, the SMD values of MF and DMF first decrease and then increase. The SMD values at 3 bar back pressure are slightly lower (at most of the distances about 5% lower) than the SMD values at 1 bar back pressure whereas the SMD values at 7 bar

back pressure are much higher than the SMD values at 3 bar back pressure. The SMD values of MF at 7 bar are about 30% to 40% higher compare to the values at 3 bar. Similarly, the SMD values of DMF at 7 bar are around 40% to 50% higher than the values at 3 bar. In order to understand this, it should be noted that the increase of the back pressure has two effects on the spray break-up: firstly, the increase of the gas density increases the drag force and thus causes higher deceleration to the spray jet. This can be observed from the droplet velocity diagram. The maximum droplet velocities are about 90 m/s, 70 m/s and 50 m/s for 1 bar, 3bar, and 7 bar back pressure, respectively. The deceleration effect becomes much bigger as the back pressure goes up. Secondly, the increase of the gas density may increases the shear force which breaks the liquid column up. As reported in the literature on diesel fuel break-up (Li, 2012), droplet sizes decrease when the back pressure increases due to the increase of the shear force. In conclusion, the increase of the back pressure has two opposite effects on the droplet size. One of the effects, the deceleration, leads to larger SMD values. The other effect, the increase of the shear force, leads to smaller SMD values. In this study, the SMD values for both MF and DMF decrease when the back pressure increases from 1 bar to 3 bar and increases when the back pressure increases from 3 bar to 7bar. This means that when the increase of the back pressure is not so significant, for example from 1 bar to 3bar, the dominant effect is the increase of the shear force rather than the deceleration. Therefore, the SMD values decrease because of the larger interaction between spray and air. When the pressure increases to 7 bar, the main affecting factor becomes the deceleration of the spray. Thus, in this case, the

SMD values increase due to the dramatic decrease in the speed. A summary of the discussion is given in Table 5-3.

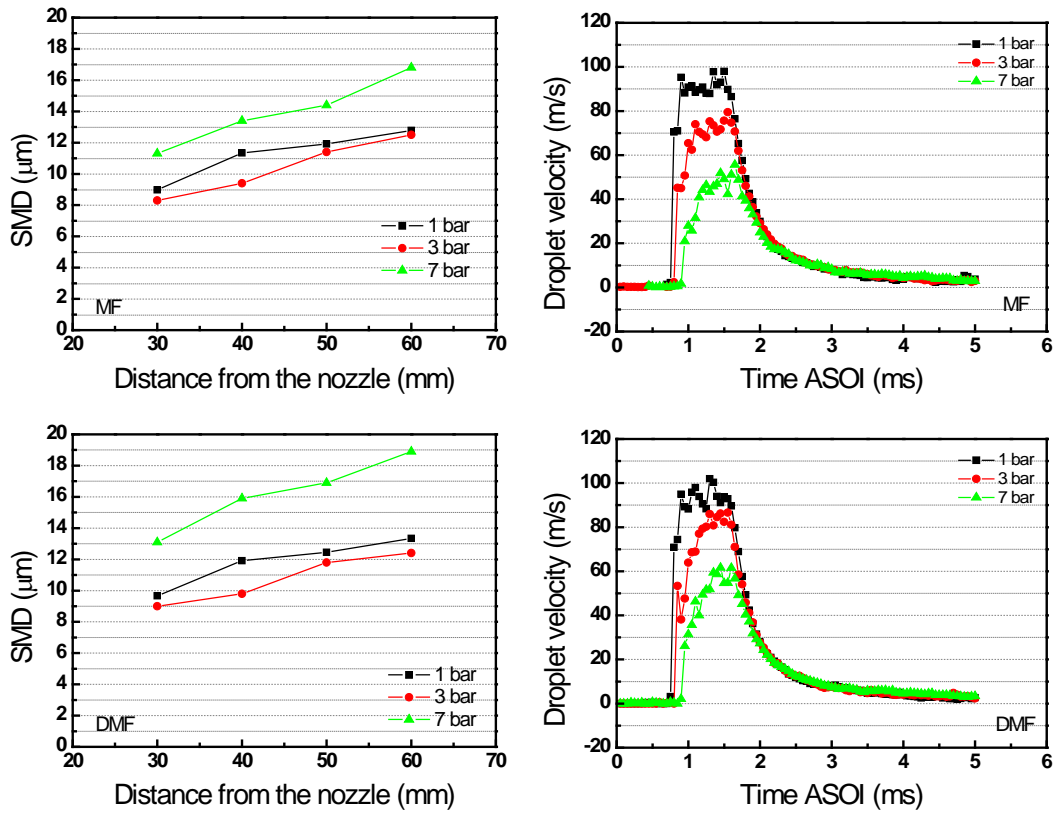


Figure 5-6: SMD values and droplet velocity of MF and DMF under three back pressures, 150 bar injection pressure and vessel temperature of 20 °C.

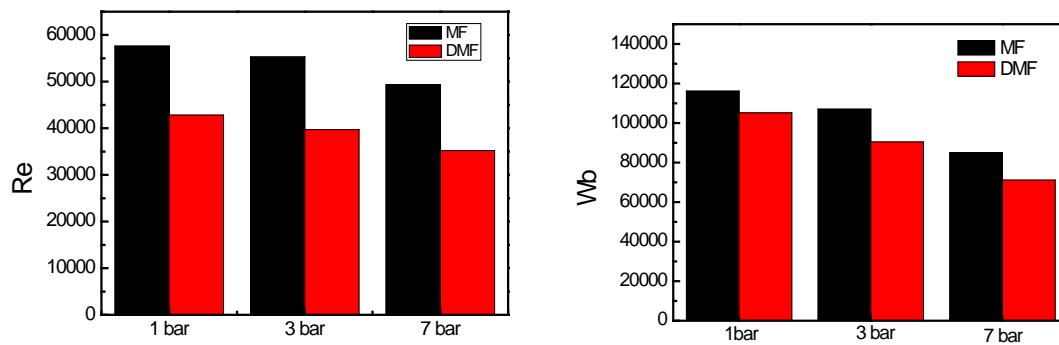


Figure 5-7: Reynolds number and Weber number of MF and DMF under different back pressures

Table 5-3: Summary of the trends for Wb, Re, and SMD at 1 bar and 7 bar back pressure

Back pressure	Wb number and Re number		SMD	Explanation
Low (1 bar)	Wb	Gasoline>ISO>MF>ETH≈DMF	ETH>DMF>MF>ISO>Gasoline	At low back pressure, the external disruptive aerodynamic force, represented by Wb, is more significant.
	Re	MF>DMF>Gasoline>ISO>ETH		
High (7 bar)	Wb	ISO>ETH≈MF>DMF>Gasoline	ETH>ISO>DMF>Gasoline≈MF	At high back pressure, the inertial force, represented by Re, has a bigger impact.
	Re	MF>DMF>ISO≈Gasoline>ETH		

The Reynolds number and Weber number for MF injection and DMF injection under different ambient pressures are shown in Figure 5-13. Both numbers decrease as the ambient pressure increase. This is due to the increased drag force from the ambient air which causes the decrease of the spray velocity. For both non-dimensional numbers, the values of MF are larger than those of DMF. This indicates better break-up of the spray. From the previous figures, it can be seen that the SMD values of MF are smaller than that of DMF.

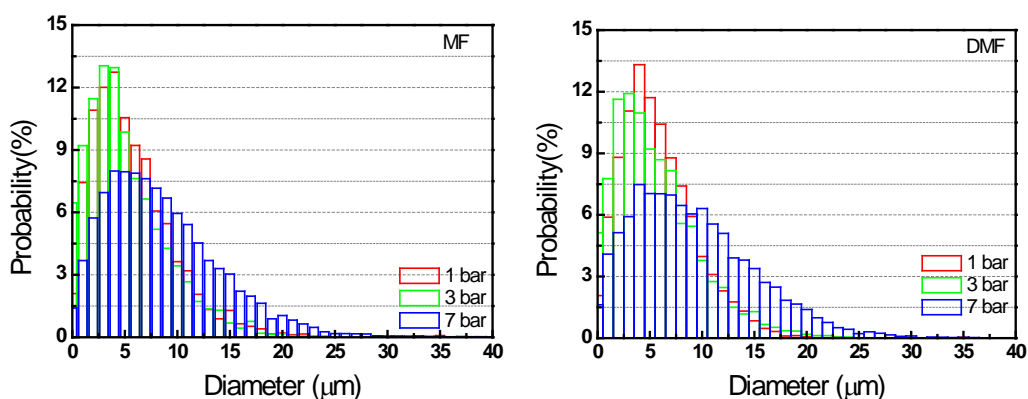


Figure 5-14: Histogram of MF and DMF at different back pressures (Injection pressure 150bar, vessel temperature 20°C and measured at 40 mm from the nozzle)

The histograms of MF and DMF at different back pressures are presented in Figure 5-14. As discussed previously, when the back pressure increases from 1 bar to 3 bar,

the SMD values of both fuels decrease; when the back pressure further increase from 3 bar to 7 bar, the SMD values of both fuels increase. This trend could be seen more clearly in the histogram figure: the back pressure has a very big impact on the droplet size distribution. As the back pressure increase from 1 bar to 3 bar, the proportion of the small droplets (between 0 μ m to 5 μ m) increases. Also, when the back pressure increases from 3 bar to 7 bar, the concentration of the big droplet significantly increase. The reason for this phenomenon is explained in previous part.

Clear differences between the SMD values of different fuels under high back pressure can be observed in Figure 5-15. The SMD values of ethanol are the highest, followed by isooctane, DMF and then gasoline. MF has the smallest SMD values. On comparing the SMD values of these fuels under 1 bar back pressure, as shown in Figure 5-4, the SMD values increase from a range of 9-14 μ m to the range of 12-20 μ m. This 30% increase of SMD values is due to the decrease of the Reynolds number and the Weber number caused by the deceleration of the spray. This trend is very different from the research on diesel or diesel-like fuel spray in the other people's study (Li, 2012), in which the SMD values decrease with the increase of the back pressure. In the case of diesel fuel injection, the injection pressure is much higher (100MPa-300MPa). The spray exit velocity is thus much higher compared with the GDI injector spray's exit velocity. The deceleration effect from the air is not significant in the case of diesel injection. However, the interaction between air and the spray increases and the effect surpasses the effect of deceleration. Therefore, the

diesel fuel droplet sizes decrease with the increase of the back pressure; whereas the droplet sizes of the gasoline alternatives decrease with the increase of the back pressure.

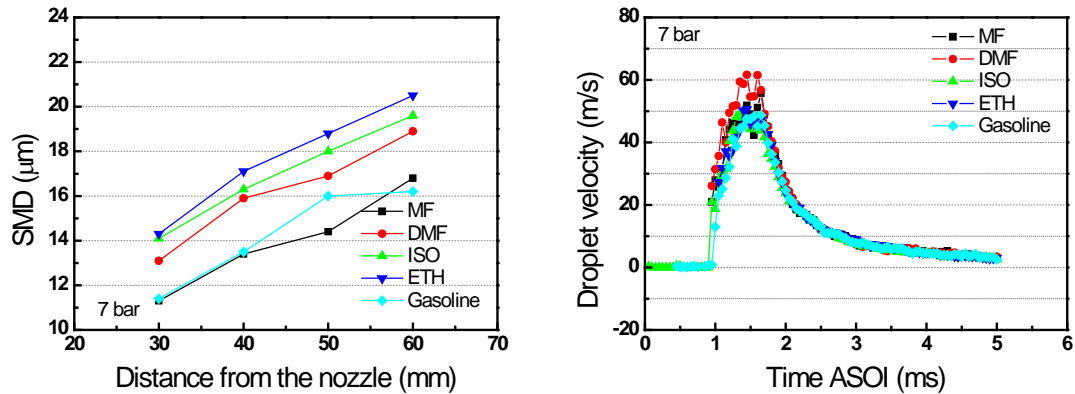


Figure 5-8: SMD values and droplet velocity of the five fuels under 7 bar back pressures, 150 bar injection pressure and vessel temperature of 20 °C.

Figure 5-15 also shows the droplet average velocity of the five fuels. It could be seen that almost all the fuels have similar droplet velocities along the time axle, except DMF. The velocity of DMF between the time 1.3 ms and 1.8 ms is higher at some points. But generally at most of the time period after start of injection, its velocity is similar to the other fuels. The effect of the higher droplet velocity on the DMF droplet size is not very clear due to its relative short period.

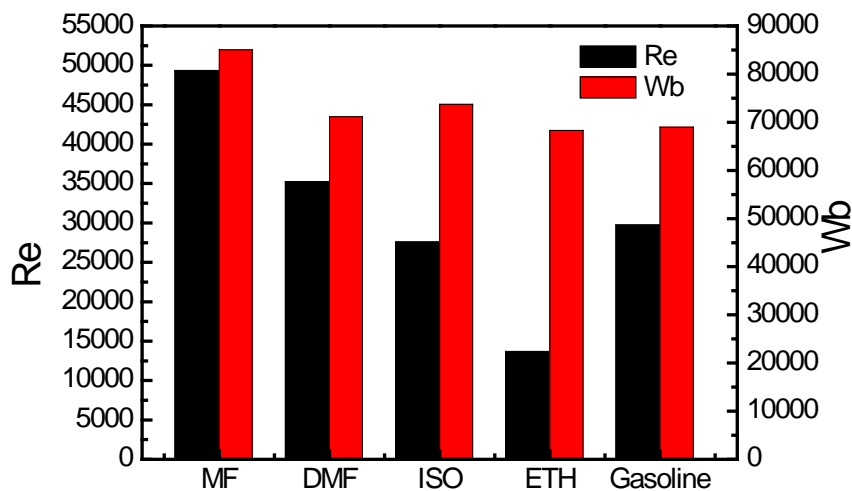


Figure 5-9: Reynolds number and Weber number of the fuel injections under back pressure of 7bar

Under the ambient pressure of 7 bar, ethanol has the largest SMD values followed by gasoline, DMF and isooctane; MF has the smallest SMD values, as shown in Figure 5-15. The SMD values of the five fuels show a reverse trend compared to the Reynolds numbers, as shown in Figure 5-16. The sequence of SMD values is no longer the same as the SMD values at 1 bar ambient pressure, which is shown in Figure 5-4, because at 1 bar ambient pressure, the dominant factor is the Weber number whereas at 7 bar ambient pressure the dominant factor is the Reynolds number.

5.3.7 Effect of the Vessel Temperature

In order to examine the effect of the ambient temperature (vessel temperature) on the SMD and the droplet velocity, the measurement of these parameters are made at three ambient temperatures (20°C, 60°C, 90°C). Figure 5-17 exhibits the SMD and droplet velocities of MF and DMF spray under three ambient temperatures. Figure 5-18 shows the Reynolds number and the Weber number of the two fuels' injection under three ambient temperatures. As mentioned in Chapter 4, the spray "collapses" when the ambient temperature reaches the fuel's boiling point. The main behaviour of the spray jet's "collapse" is the significantly reduced penetration length and the disappearance of the clear boundary of each jet. In the meantime, the vessel temperature has a negative effect on the SMD values of MF and DMF, as shown in Figure 5-17. When the vessel temperature increases, the SMD values of both fuels decrease.

It can be clearly seen that the increase of the vessel temperature leads to decrease of

the droplet velocity. If the vessel temperature is lower than the fuel's boiling point, the droplet velocity only decreases slightly (about 10m/s decrease on the droplet velocities for the temperature increase from 20 °C to 60 °C for MF and DMF). If the vessel temperature is higher than the fuel's flash boiling point, the droplet size would fall dramatically. The droplet velocity of MF decreases by 60% to 70% as the vessel temperature increases from 60 °C to 90 °C. This effect is mainly due to the “collapse” of the fuel spray.

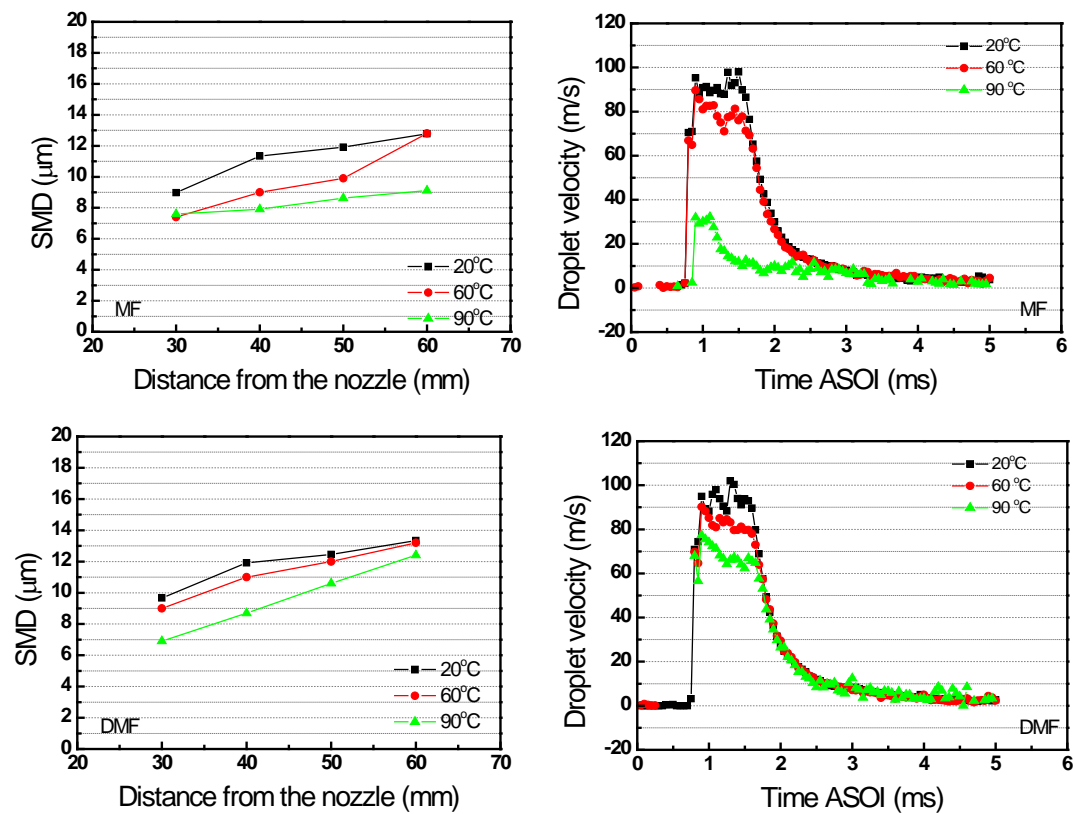


Figure 5-10: SMD values and droplet velocities of MF and DMF under 150 bar injection pressures, 1 bar back pressure and vessel temperature of 20°C, 60 °C and 90 °C.

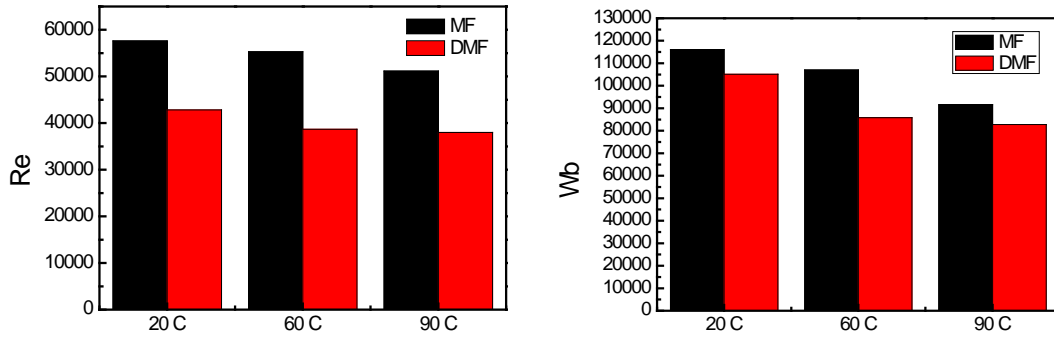


Figure 5-11: Reynolds number and Weber number of MF injection and DMF injection at different ambient temperatures

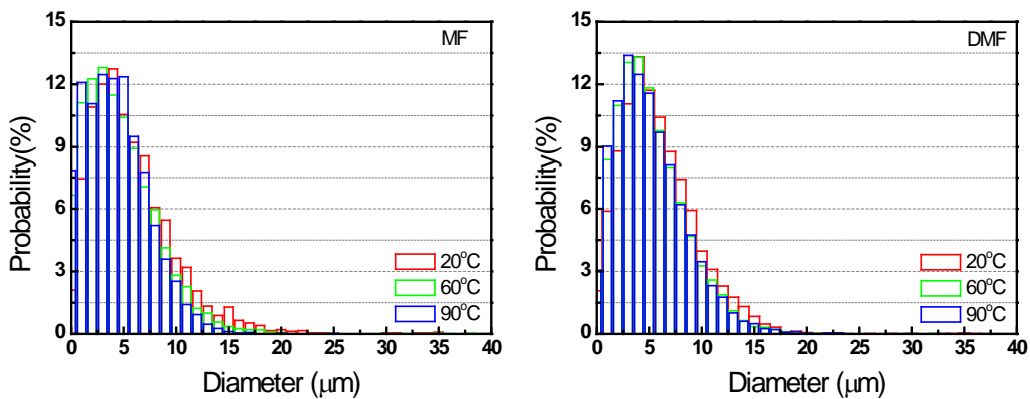


Figure 5-19: Histogram of MF and DMF at different ambient temperatures (40 mm from the nozzle)

The effect of the vessel temperature on the probability of the droplet size of MF and DMF is shown in Figure 5-19. With the increase of the ambient temperature, it could be seen that proportion of the big droplet significantly decreases due to evaporation of the fuels. Also, it could be seen that probability of the small droplets (less than 5 μm) increase. This means that the medium size droplets become small droplets when the surrounding temperature is high. The main effect of the ambient temperature on the atomization of MF and DMF is the evaporation of all the droplets.

5.3.8 Ohnesorge number at different conditions

In order to estimate the atomization of the fuels under different conditions (test

conditions presented in Table 5-4), the Ohnesorge numbers of them are plotted against their Reynolds numbers, as shown in Figure 5-20. The method of calculation the Ohnesorge number is described in chapter 2.3.1. In this figure, the break-up regimes which are defined by Reitz et al. (1982) are also added. It should be noted that, for all the fuels, regardless of their injection pressure, back pressure, and ambient temperature, all of the test points are well in the atomization regime. This means the onset of the fuel liquid column break-up is, or at least very close to, the nozzle exit. In this regime, the complete disintegration of the jet leads to very small droplets.

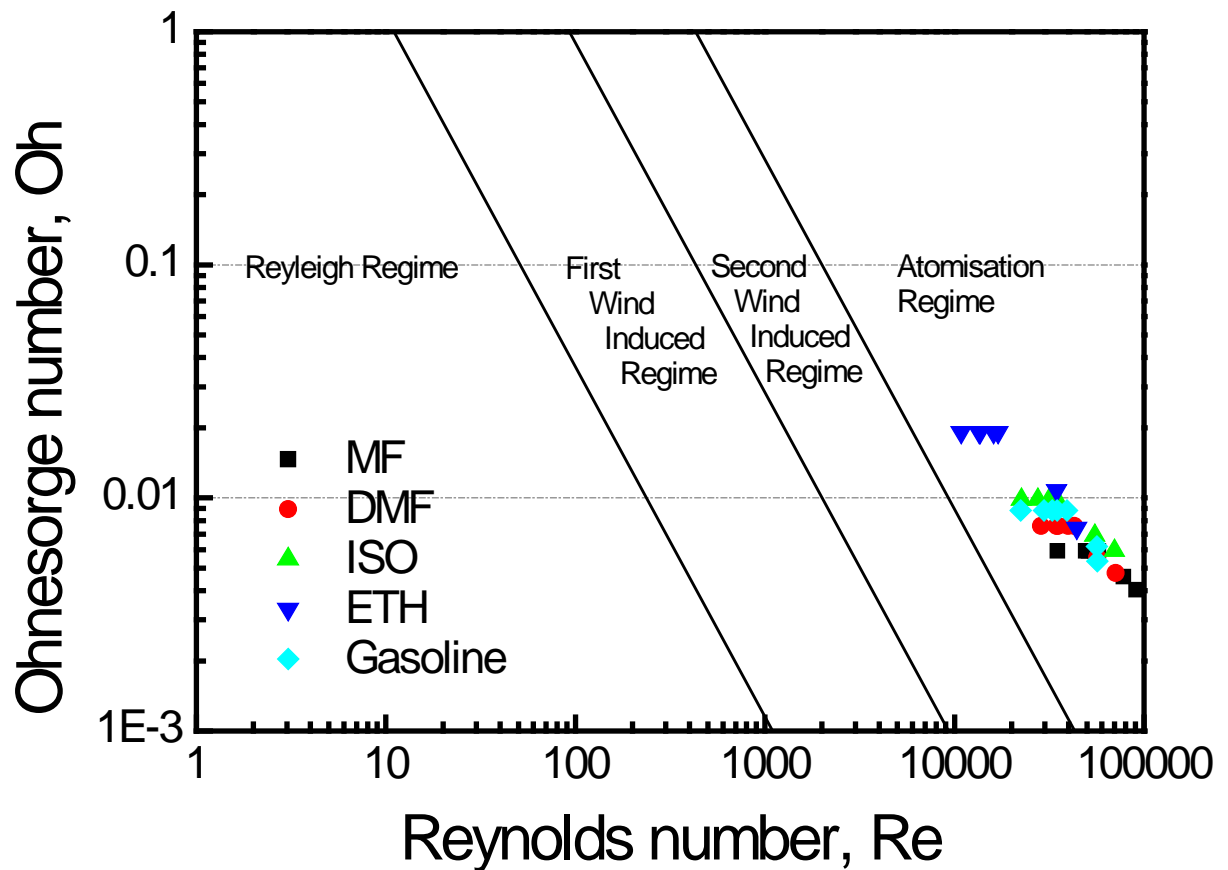


Figure 5-20: Ohnesorge diagram for the injection

Table 5-4: Test conditions for the Ohnesorge numbers plotted in Figure 5-20

Fuel	Injection pressure (bar)	Back pressure (bar)	Vessel temperature (°C)
MF	50	1	20
	100	1	20
DMF	150	1	20
	150	3	20
ETH	150	7	20
	150	1	60
Gasoline	150	1	90

5.4 Summary

This chapter evaluates the atomization of the fuels in terms of droplet size and velocities. The effect of the measuring point, injection pressure, back pressure and ambient temperature on the droplet size and the droplet velocity are investigated. The following conclusions are drawn:

1. The differences of the fuel properties (e.g. density, viscosity, and surface tension) are estimated by calculating their Reynolds numbers and Weber numbers under different test conditions. Ethanol spray has a relatively higher Weber number and Reynolds number at almost all the conditions, thus its droplet size is the biggest under almost all test conditions. DMF usually has a bigger droplet size compared to gasoline. The droplet size of MF is usually smaller than that of DMF, due to the higher Reynolds numbers and Weber numbers. The order of the SMD values among the three fuels (MF, DMF and gasoline) varies under different test conditions, due to the varying combined effect of the Reynolds number and the

Weber number. Generally, Compared to ethanol, the droplet size of MF and DMF was more similar to that of gasoline and isooctane at different conditions.

2. The main effect of the injection pressure on the spray break-up is on the spray exit velocity. Higher injection pressure leads to higher spray velocity; thus a higher Reynolds number and Weber number could be observed. Both the inertial force and the external force, which break up the spray liquid column and the droplets, are bigger. Therefore smaller SMD values and higher droplet velocities are expected and observed.
3. Two main effects of the back pressure on the spray break-up are observed: Firstly, the increase of the gas density increases the drag force and thus causes deceleration to the spray jet. This effect hinders the break-up of the spray. Secondly, the increase of the gas density may increase the shear force which makes the liquid column easier to break up. The SMD values for both MF and DMF decrease by around 5% at most distances when the back pressure increases from 1 bar to 3 bar. And the SMD values of the two fuels increase by around 30% to 50% when the back pressure increases from 3 bar to 7bar. This means the dominant factor affecting between 1 bar and 3 bar is the increase of the shear force and when the pressure continues to increase the main effect becomes the spray jet deceleration.
4. When the injection pressure is relatively high (150 bar) and the back pressure is relatively low (1 bar), the dominant affecting factor is the Weber number. The shear force between the flow and the ambient air dominates the spray break-up. If

the back pressure is relatively high (7 bar), the dominant factor shifts to the Reynolds number. In this situation, the drag force which is applied on the flow from the air is very high. The flow deceleration is so fast that the speed of the flow downstream of the spray is low. The shear force, which is due to the interaction between the spray flow and the air, is thus restrained. The internal force, which is represented by the Reynolds number, becomes the main affecting factor.

5. The main effect of the vessel temperature on the droplet size and the velocity is linked to the fuel's flash boiling point. If the vessel temperature is lower than the fuel's flash boiling point, the droplet velocity only decreases slightly. If the vessel temperature is higher than the fuel's flash boiling point, the droplet size would fall dramatically. With the increase of the surrounding temperature, the SMD values of MF and DMF injection decrease.

Chapter 6

Laminar Flame Characteristics of 2, 5-dimethylfuran and 2-methylfuran

This chapter examines the laminar flame characteristics of the bio-fuels, MF and DMF, compared to isooctane. In particular, the laminar burning velocity and the flame instability of the fuels are discussed.

6.1 Introduction

Laminar flame propagation characteristics are important fundamental physicochemical properties for a fuel; they are the basic data required for combustion modeling and also can be used in validating the chemical reaction mechanisms of the fuel (Law, 2000). Using high speed schlieren photography, this work examines the laminar burning characteristics of MF-air mixtures with varying temperatures (60°C, 90°C and 120 °C) and equivalence ratios (0.7-1.1) at 0.1MPa initial pressure in a constant volume vessel. The stretched flame speeds are determined by the outwardly spherical flame method. The unstretched flame speed, Markstein length and laminar burning velocity of MF combustion at different equivalence ratios and temperatures are then deduced and compared to those of DMF and isooctane. Finally, the flame instability analysis including the analysis of the flame thickness, density ratio and laminar burning flux is provided.

6.2 System Validation

In order to validate the system setup and procedures used, laminar burning velocities of isooctane-air mixtures at 0.1MPa initial pressure and elevated temperatures were calculated and compared with the data from the literature in Figure 6-1. It is shown that the current measurement has a good agreement with the widely accepted result of Bradley et al.(1998), and Hasse et al.(2000). It can also be seen that the current results are higher than the work of Kelley et al. (2011). It is because their initial temperature is 80°C and the initial temperature for current work is 90°C. The Markstein Length of isooctane from the current measurement is also compared with data from literature. The current results show good agreement with the results of Halter et al.(2010), Zhou et al. (2011) and Bradley et al.(1998). The method they used to calculate the Markstein length is the same as the current work (Linear methodology, described in chapter 3.5.3). There is some difference between the current results and the results of Galmiche et al.(2012) and Varea et al.(2012). This is because the current work uses linear methodology to deduce the Markstein length. However the work of Galmiche et al. and Varea et al. use non-linear methodology, which is developed by Kelley and Law (2009), to deduce the Markstein Length. Therefore, differences at lean conditions could be expected. Generally, it could be seen that the current work shows acceptable agreement with the work found in literature in terms of laminar burning velocity and Markstein Length (Linear methodology). This validates the present experimental setup and methodology.

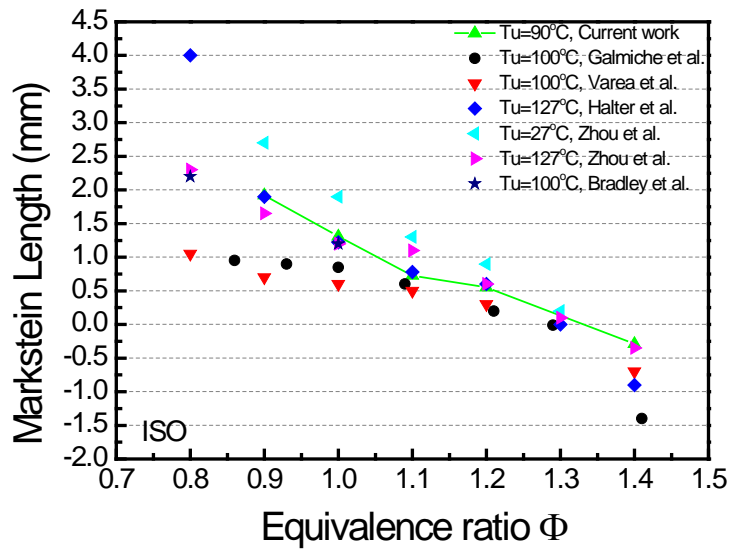
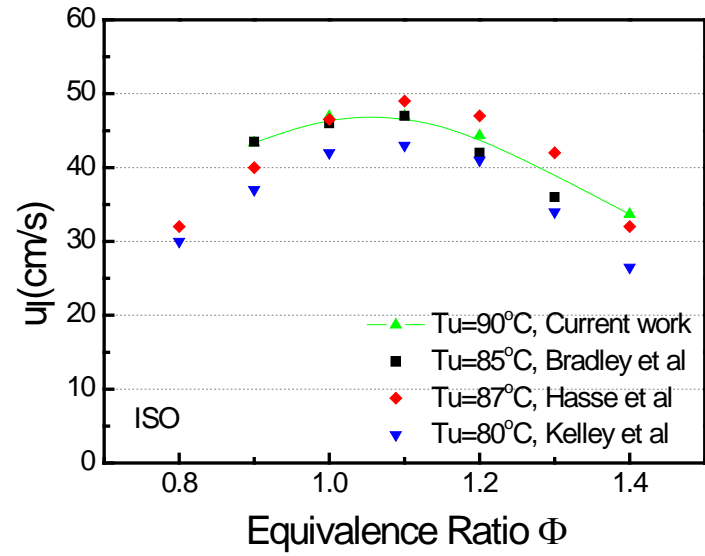


Figure 6-1: Laminar burning velocities and Markstein length of isooctane-air mixtures versus equivalence ratios at 0.1MPa pressure and elevated initial temperature

6.3 Flame Morphology

The schlieren images for MF, DMF and isooctane at stoichiometric conditions and the initial temperature of 90°C are shown in Figure 6-2. MF flame propagation is the fastest and isooctane flame propagation speed is the slowest. Due to the quenching effect from the electrodes the flame propagation speed is always slower along the direction of the electrodes than the vertical direction thus the flame is not perfectly spherical. Small wrinkling also appears near the electrodes, but it does not affect the overall shape of the flame.

Based on the repeated schlieren imaging, it was found that the early stage of the flame is greatly affected by the spark energy. While as the flame approaches the vessel boundary, the shape of the flame becomes distorted with the flatter surface at the vertical sides due to the influence of the internal geometry (Burke, 2009).

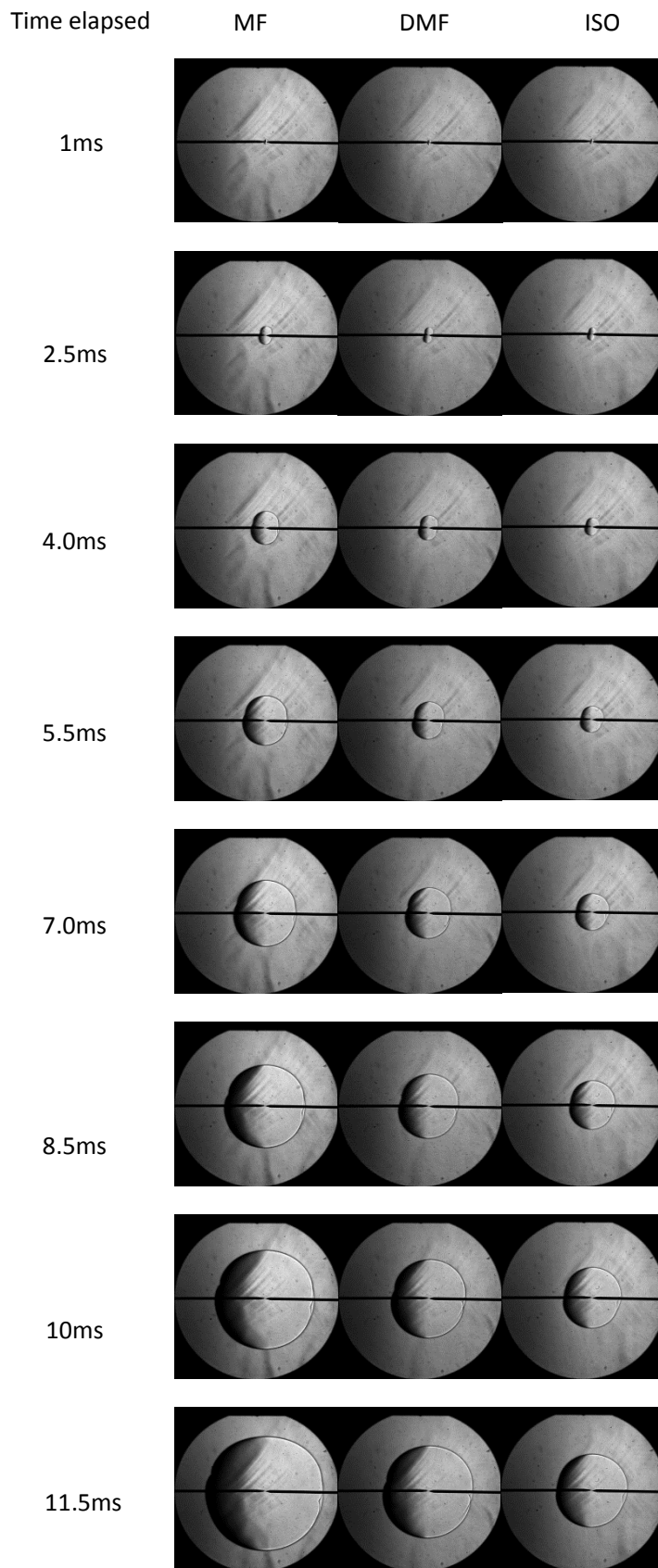


Figure 6-2: Chronological schlieren images of stoichiometric fuel-air mixtures at initial temperature of 90°C.

6.4 Stretched and Unstretched Flame Speed

Figure 6-3 shows the stretched flame propagation speed versus stretch rate for the three fuels at different equivalence ratios and 120°C initial temperature. Both the stretched propagation speed and the stretch rate are calculated by detecting the flame front from four directions, as shown in Figure 3-16. With respect to time, the flame expands in the vessel; the flame stretch rate becomes smaller due to the inverse relationship between the flame stretch rate and flame radius. The close-to-linear relationship between the flame stretch rate and the flame radius can be observed at a large stretch rate. For instance, in Figure 6-3 a, it can be seen that all the results show a good linearity at large stretch rates (the fitting line plotted on the figure). At a relatively smaller stretch rate, when the flame radius are big, the acceleration of the stretched flame speed decreased or even stopped, thus the trends become non-linear. This demonstrates that the geometry of the vessel affects the flame propagation when the flame boundary approaches to the vessel wall.

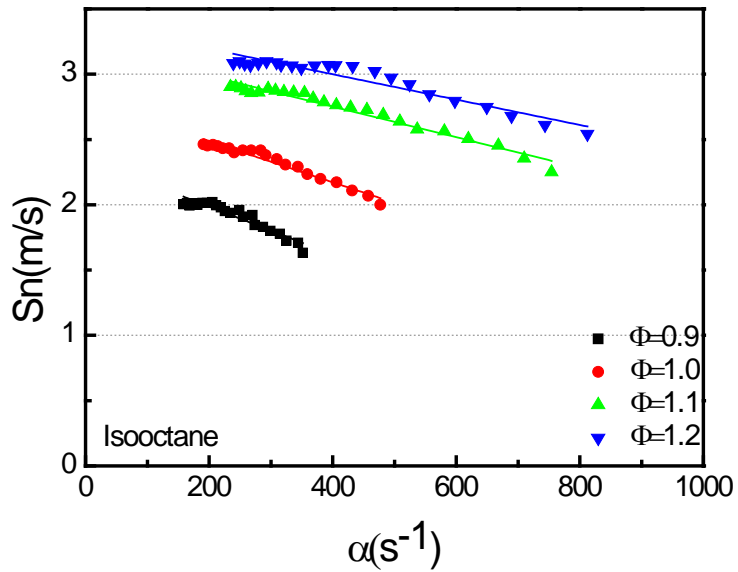
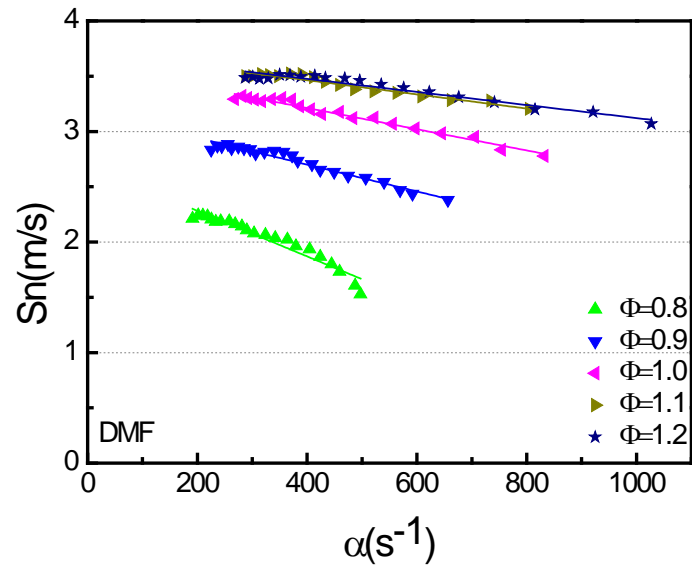
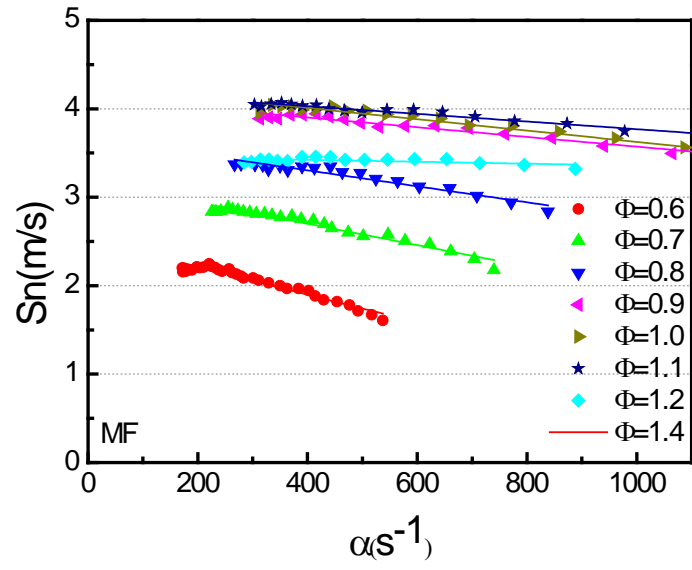


Figure 6-3: Stretched flame speed of the test fuels at 120°C initial temperature at different equivalence ratios and stretch rates.

The unstretched flame propagation speed was obtained by extrapolating the stretched flame propagation speed to zero stretch rate and the Markstein length was obtained by calculating the gradient of the stretched flame propagation speed to stretched rate slope. Figure 6-4 shows the unstretched flame speed of the three fuels at different temperatures and equivalence ratios. For all the temperatures (60°C, 90°C and 120°C), MF has the fastest unstretched flame propagation speed at all the equivalence ratios. For instance, at 120°C and under the same equivalence ratio, the unstretched flame propagation speed of MF is about 15% faster than that of DMF and about 20%-50% faster than that of isooctane. The unstretched flame propagation speeds of the three fuels increase significantly with the increase of initial temperatures, as expected. The maximum unstretched flame propagation speed of MF occurs at slightly rich region when $\Phi=1.1$ for the three temperatures tested, although the unstretched flame propagation speed for $\Phi=1.2$ is only slightly slower than that at $\Phi=1.1$. However for DMF and isooctane, the maximum unstretched flame propagation speeds occur between the equivalence ratios of 1.1 and 1.2. The error bars in Figure 6-4 indicate that the root mean square deviation (RMSD) for different measurement of the laminar burning velocity is generally less than 2%. However, very rarely, at a few extreme test points, the RMSD could be 5% to 7% (e.g. the RMSD for MF at 90°C and $\Phi=1.1$ is 6%).

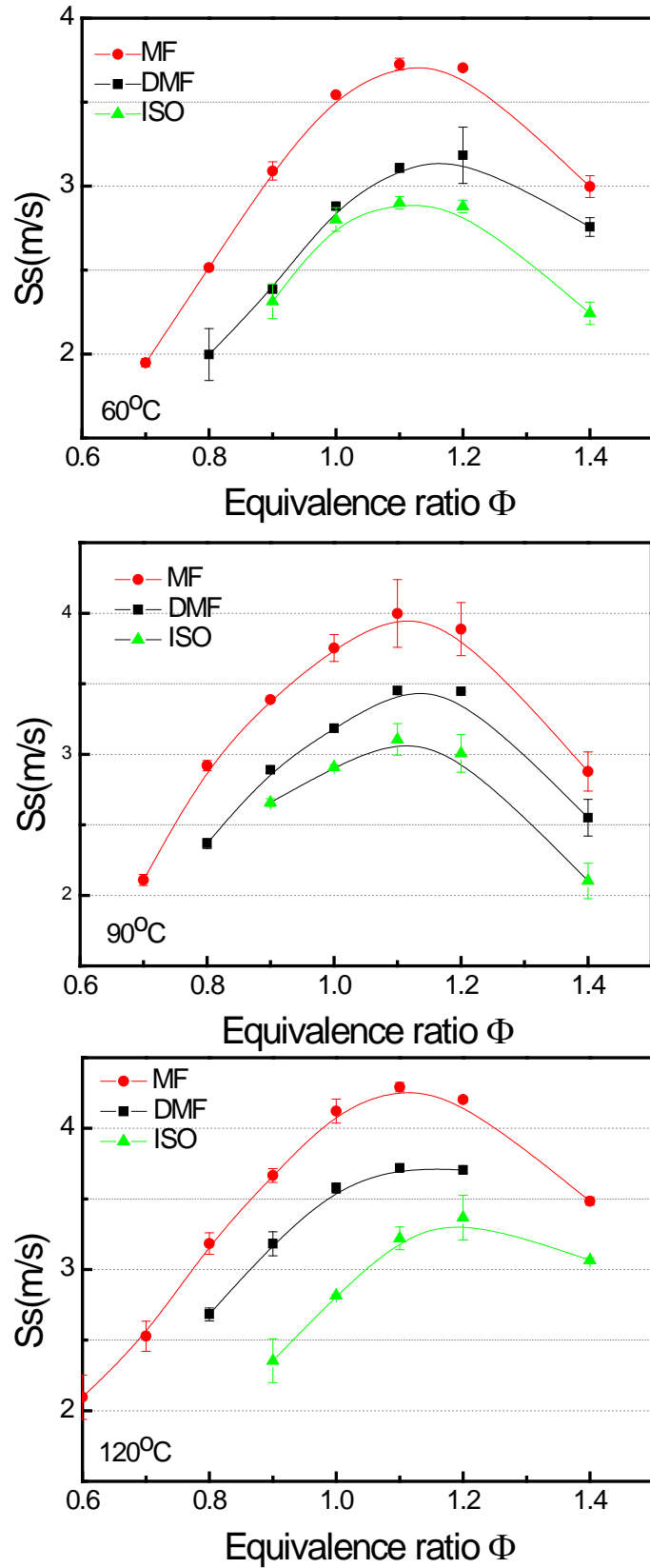


Figure 6-4: Unstretched flame speed of the test fuels at different temperatures and equivalence ratios

6.5 Adiabatic Flame Temperature and Laminar Burning Velocities

The adiabatic flame temperatures for MF, DMF and isooctane under 120°C initial temperature at varying equivalence ratios are shown in Figure 6-5. MF has the highest adiabatic flame temperature, followed by DMF and then isooctane. The adiabatic flame temperatures of MF and DMF reach their peaks at the equivalence ratio of 1.1. The same trend can be observed for isooctane except that the peak occurs under the condition closer to a stoichiometric ratio of 1.0. For hydrocarbon-air mixtures the adiabatic flame temperature peaks at the rich mixture side due to the product dissociation and reduced amount of heat release.

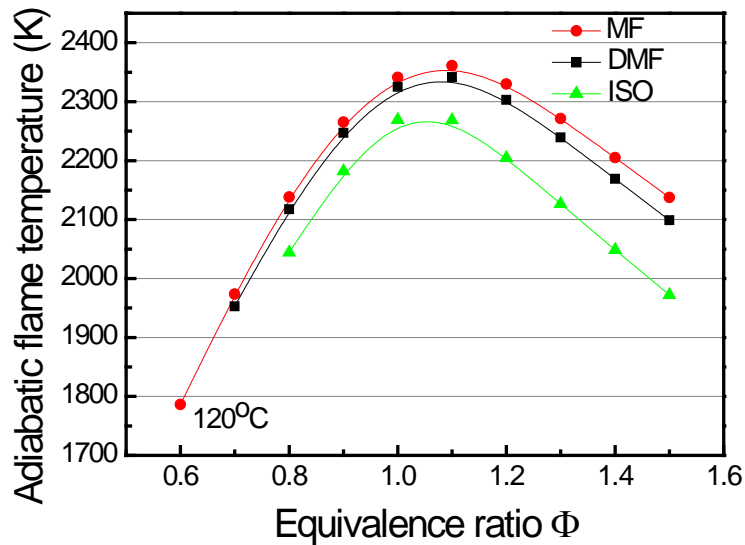


Figure 6-5: Adiabatic flame temperatures for three fuels at 120°C with varying equivalence ratios.

The laminar burning velocity is a strong function of the equivalence ratio and initial temperature of the reactants (Stone, 1999). It is the speed at which the flame is advancing into the unburned mixture. Figure 6-6 shows the laminar burning velocities

versus the equivalence ratios at different initial temperatures. The laminar burning velocities of MF under varying initial temperatures reach their peaks in the equivalence ratio range of 1.1 to 1.2 and this is correlated to the state of the adiabatic flame temperatures. For the other two fuels, a similar trend can be observed. Compared with DMF and isooctane, MF has the highest laminar burning velocities at all conditions. For instance, at 90 °C initial temperature and the equivalence ratio of 1.2, the laminar burning velocities of MF, DMF and isooctane are 69cm/s, 61cm/s and 56cm/s, respectively. Based on Tabaczynski's theory described in the literature (Stone, 1999), the flame burning rate in a spark ignition engine is largely affected by the laminar burning velocity and turbulence intensity in the combustion chamber. With the same engine configuration and operation conditions, the fuel which possesses higher laminar burning velocities burns faster in the cylinder. The work of Wang et al. (2013) proved that the combustion duration of MF is much shorter than that of DMF and gasoline in a DISI engine, which leads to higher indicated thermal efficiency than the other two fuels. In addition, the laminar burning velocities for all the three fuels increase with the initial temperature. For MF, the laminar burning velocity at 120 °C is about 16%-18% faster than that at 90 °C and 34%-40% faster than that at 60 °C within the range of equivalence ratio 0.7-1.1.

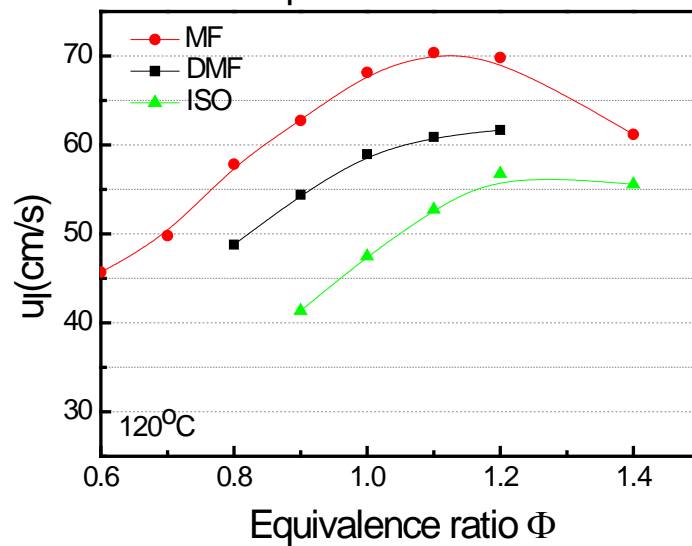
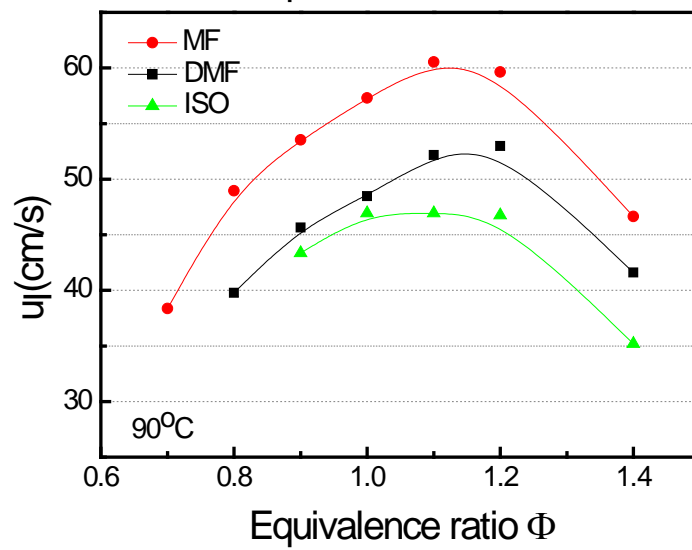
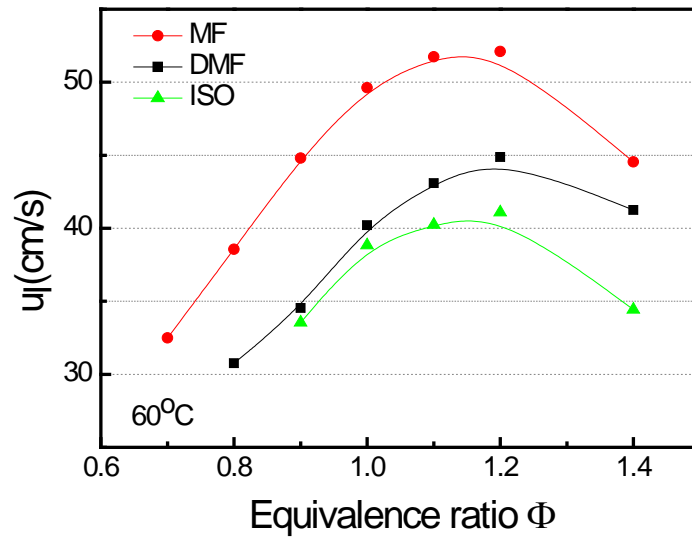


Figure 6-6: Laminar burning velocities of test fuels at different temperatures and equivalence ratios.

6.6 The Flame Instability

The flame instability is essential for understanding of the combustion of a fuel. In flame propagation, the flame front cellular instability leads to self-acceleration and the detonation. If this happens in an engine, the heat release will be very unsteady and knock might occur. In order to understand the effect of the influencing factors on the flame front instability, it is necessary to give a short review on the theory. According to the literature (Law, 2000 and Matalon, 2007), there are mainly two types of flame surface instabilities acting on the flame front when the laminar burning velocity is relatively high: the diffusion-thermal instability and the hydrodynamic instability. The diffusion-thermal instability is a result of diffusion in the flame front while the hydrodynamic instability is a result of thermal expansion of the gas upon crossing the flame. The diffusion-thermal instability is characterized by the Markstein length. The hydrodynamic instability of the flame front, which is induced by the density transition across the flame front, is characterized by the flame thickness and the density ratio. The increase of the density ratio or the decrease of the flame thickness indicates the promotion of this kind of instability.

6.6.1 Markstein Length

Markstein length indicates the effect of stretch rate on flame propagation speed, and characterizes the diffusion-thermal instability (Law, 2000 and Karlin, 2007) of the fuel. For heavy hydrocarbon–air mixtures, the Markstein length decreases with the increase of equivalence ratio; while for light hydrocarbon–air mixtures it increases with the increase of the equivalence ratio (Bechtold, 2001). Figure 6-7 shows that the

Markstein lengths of MF and the other two fuels at tested temperatures all decrease with the increase of the equivalence ratios, and this observation is in agreement with the above theory since these three fuels are all heavy hydrocarbon fuels. The results also show that the Markstein length of MF is significantly smaller than those of DMF and isooctane at equivalence ratios lower than 1.1. However, at equivalence ratios higher than 1.1, the differences between MF and the other two fuels are within the error range. So, it can be concluded that the diffusion-thermal instability of MF is higher than DMF and isooctane at low equivalence ratios and it is nearly the same compared to DMF and isooctane at equivalence ratios higher than 1.1.

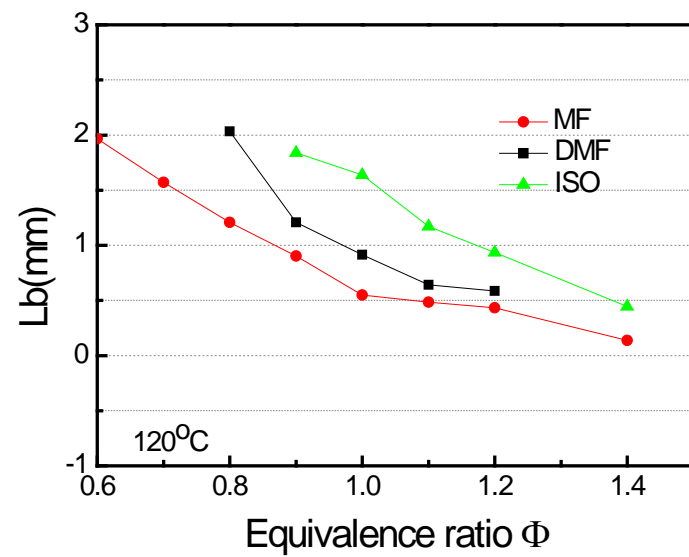
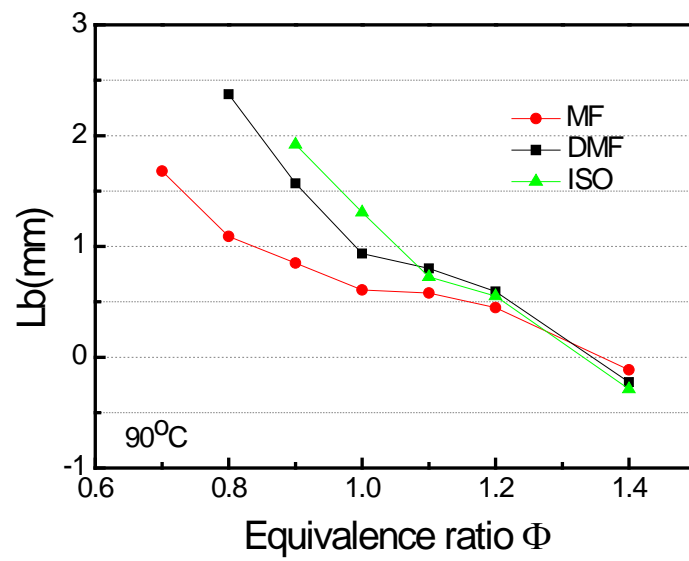
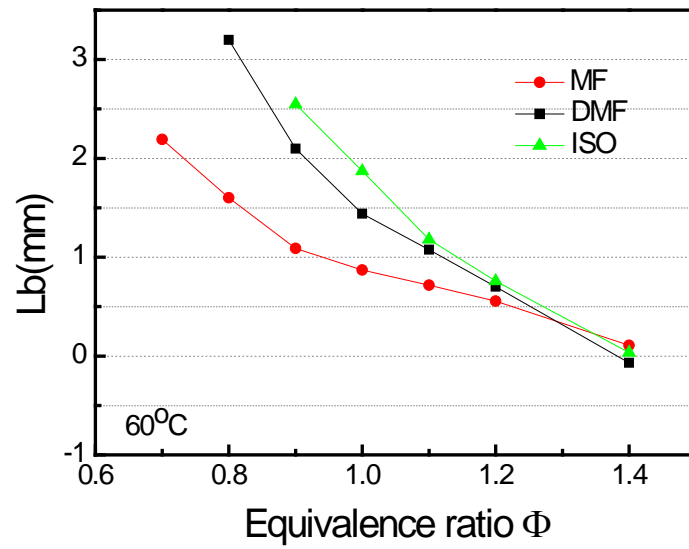
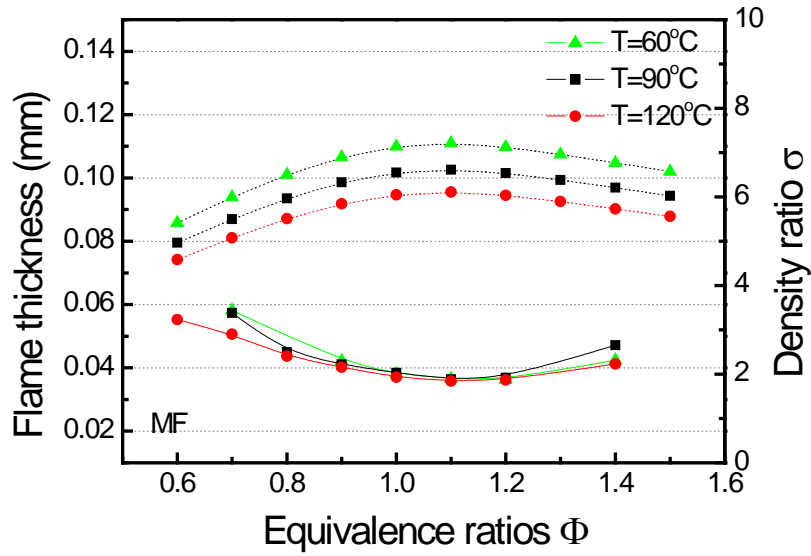


Figure 6-7: Markstein length of test fuels at different temperatures and equivalence ratios.

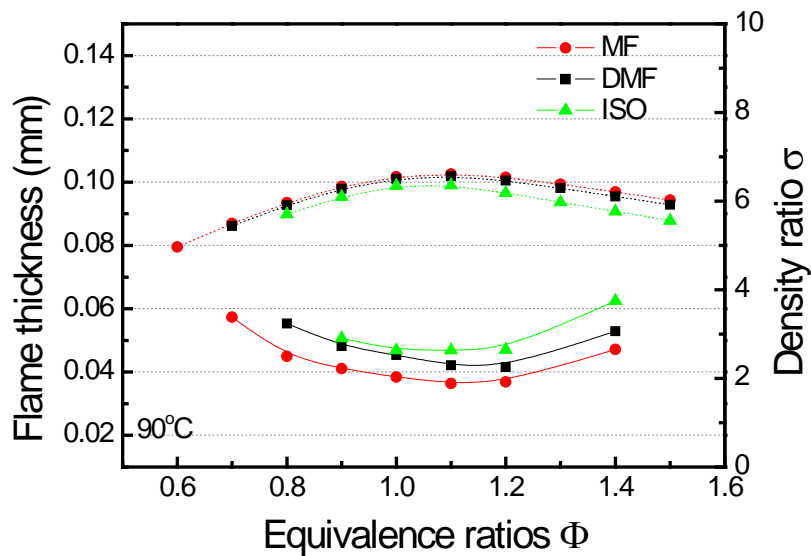
With respect to initial temperature under the same equivalence ratio conditions, the difference between the Markstein lengths of MF for 90°C and 120°C are very small. At 60°C, MF has bigger Markstein lengths than the other two temperatures (90°C and 120°C) at low equivalence ratios (0.7-1.0) but the differences become very small at high equivalence ratios (1.1-1.4).

6.6.2 Flame Thickness and Density Ratio

Figure 6-8 shows the flame thickness and density ratio versus equivalence ratio for MF at different initial temperatures and the three fuels at an initial temperature of 90°C. For MF, the flame thickness is not sensitive to variation of initial temperature whereas the density ratio decreases with the increase of the initial temperature, as shown in Figure 6-8 a. It is indicated in Figure 6-8 b that MF has the smallest flame thickness at all equivalence ratios compared to DMF and isooctane. Also, it can be seen that the density ratio of MF and DMF are similar and both of them are slightly higher than that of isooctane. Therefore, the hydrodynamic instability of MF is the highest amongst the three fuels followed by DMF and then isooctane and it decreases with the increase of the initial temperature.



(a)



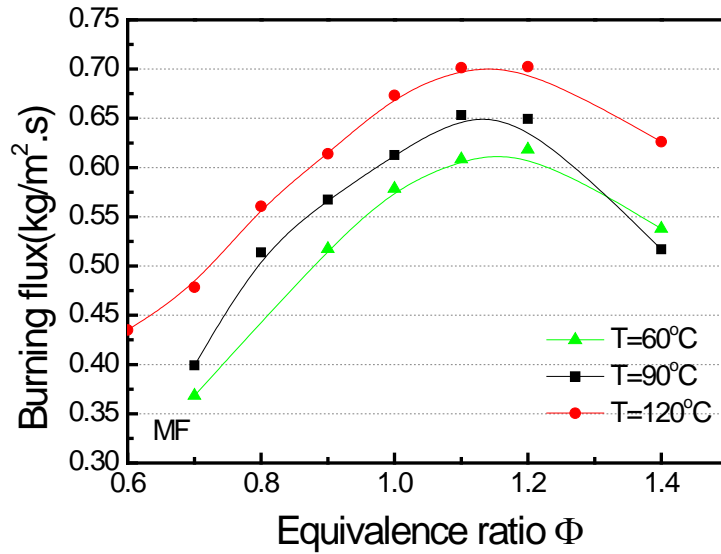
(b)

Figure 6-8: Flame thickness (solid line) and density ratio (dot line) versus equivalence ratio for (a) MF under three temperatures (b) three fuels under 90°C .

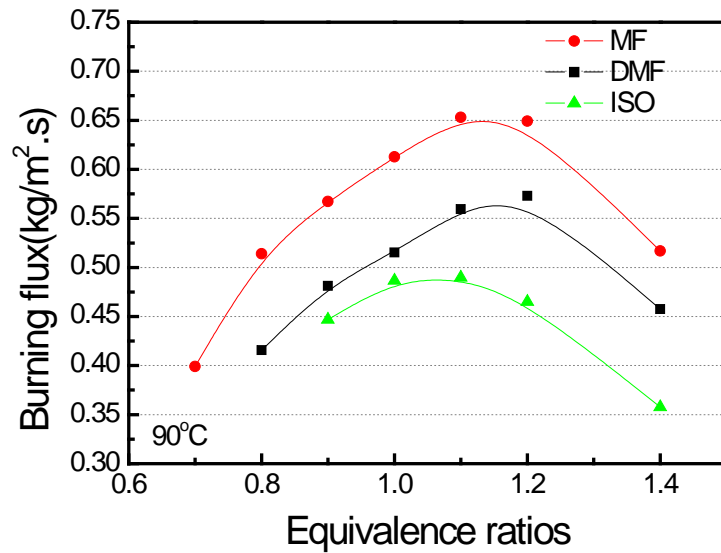
6.6.3 Burning Flux

Laminar burning flux is the eigenvalue of flame propagation. It provides the essential information of exothermicity, reactivity and diffusivity (Law, 2006). It is a very important indicator of the fuel's combustion properties. Figure 6-10 shows the

burning flux versus equivalence ratio for MF at different initial temperatures and the three fuels at an initial temperature of 120°C. The laminar burning flux of MF increases with the increase of the initial temperature. With increasing initial temperature, the increase of the laminar burning velocity of MF is the main effect on the laminar burning flux compared to the decreasing density of the MF-air mixture. The peak values of the laminar burning flux of MF at three temperatures appear between equivalence ratio 1.1 and 1.2. Figure 6-10 b shows that the burning flux of MF is the highest amongst the three fuels followed by DMF and then isooctane. The laminar burning flux of MF and DMF exhibit peak values between equivalence ratios of 1.1 and 1.2 whereas the laminar burning flux of isooctane exhibits peak values between equivalence ratios of 1.0 and 1.1.



(a)



(b)

Figure 6-9: Burning flux versus equivalence ratio for (a) MF under three temperatures (b) three fuels under 120°C.

6.7 Summary

An experimental investigation of the laminar combustion characteristics of 2-methylfuran (MF) was conducted using high speed schlieren photography in a constant volume vessel at elevated temperatures (60°C, 90°C and 120°C) and varied equivalence ratios ($\Phi=0.6-1.4$) under 0.1MPa initial pressure. The characteristics of

MF laminar flame were compared to those of DMF and isooctane. The conclusions drawn from the study for the tested conditions are as follows:

1. The unstretched flame speed of MF is up to 30% faster than that of DMF and up to 50% faster than that of isooctane. The highest unstretched flame speed of MF under all temperatures occurs at the equivalence ratio of 1.1, whereas for DMF and isooctane, the highest unstretched flame speed occurs at equivalence ratios between 1.1 and 1.2.
2. At equivalence ratios lower than 1.1, MF flame is less stable than DMF and isooctane and the Markstein lengths of MF are smaller than those of DMF and isooctane. At the equivalence ratios higher than 1.1, the Markstein length differences between MF and the other two fuels are very small.
3. The laminar burning velocity of MF is the highest amongst the three fuels under all the conditions tested, and it reaches its maximum of 70.4cm/s at an initial temperature of 120°C and an equivalence ratio of 1.1.
4. MF has the smallest flame thickness at all the conditions tested compared to DMF and isooctane. For MF, the density ratio is significantly affected by the initial temperature whereas the flame thickness is very insensitive to initial temperature change.
5. The laminar burning flux of MF increases with the increase of initial temperature and exhibits peak values between the equivalence ratios of 1.1 and 1.2. Compared to DMF and isooctane, the burning flux of MF is the highest at all the conditions tested.

Chapter 7

Turbulent Flame Behavior in the Engine

This chapter investigates the turbulent flame behavior of the bio-fuels in the optical engine using high speed imaging and OH-LIF. The turbulent flame propagation speed, the burning rate, and the fluorescence signal were measured and correlated.

7.1 Introduction

Despite the aforementioned OH-LIF and high speed imaging studies on a wide range of open flames and in-cylinder combustion (Soid , 2011, Singh, 2009), an optical study of the in-cylinder combustion of DMF and MF to reveal the information of OH distribution and flame has not been reported. In this paper, a combination of high-speed imaging and PLIF is used to observe the flame propagation and OH in the combustion process of DMF and MF, using a DISI optical engine with homogeneous mixtures generated by an early injection strategy. The experiment was carried out at two different engine load conditions (for IMEP of 4.5 and 5.5 bar). Heat release analysis and image studies were performed. Isooctane was used as the reference fuel instead of gasoline as in many relevant research studies (Schulz, 2005) because of its non-fluorescent characteristics. The key contribution is that four empirical functions has been constructed which can correlate the data from the present study and also the previous publications among OH distribution, flame propagation and heat release rate. These functions reveal the close link between the flame images in 2-D form and the

combustion parameters in the cylinder (e.g. heat release, MFB). They offer an alternative way to estimate the combustion in the cylinder (e.g. heat release, MFB) using photography method rather than using the pressure data.

7.2 Test Conditions

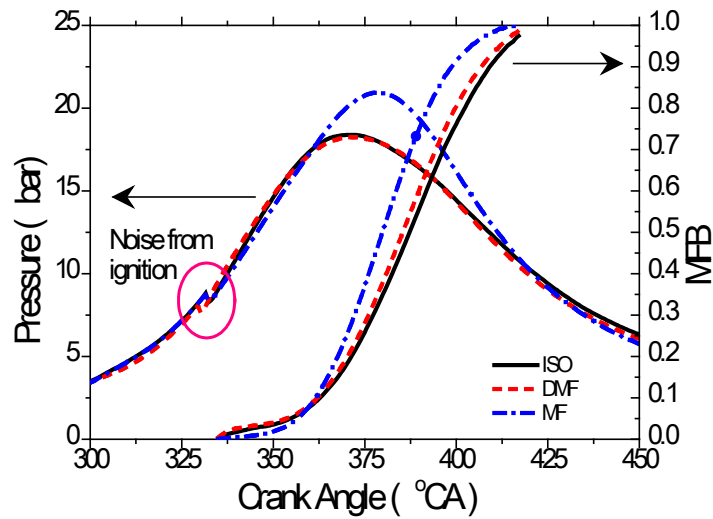
The engine was operated at IMEPs of 4.5 and 5.5 bar with stoichiometric air/fuel ratios for three different fuels, i.e. isooctane, DMF and MF. The injection timing was 280°CA BTDC in order to generate homogeneous mixtures and the ignition timing was fixed for each engine load condition, which was 29°CA BTDC for IMEP 4.5 bar and 24 °CA BTDC for IMEP 5.5 bar. A pressure transducer was used to record the in-cylinder pressure. Before the pressure data was recorded, the engine was operated for at least 3 minutes to stabilize its operating condition.

7.3 Pressure Trace and Combustion Phase

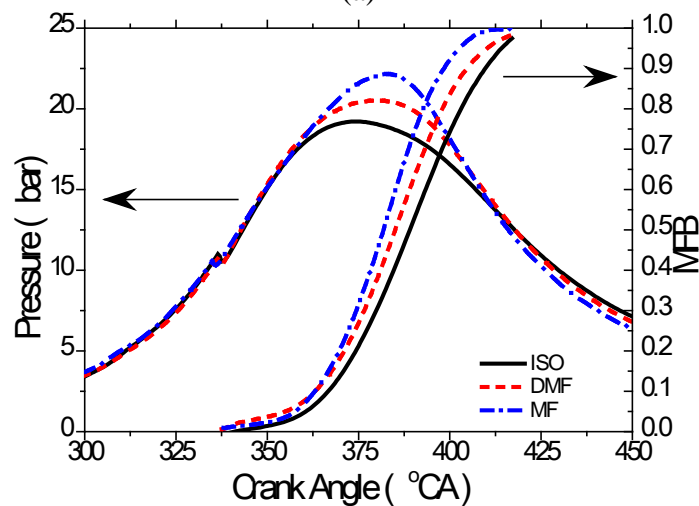
The in-cylinder pressure results were averaged from 100 cycles for each throttle position used in the optical measurement. The pressure traces of the three fuels (isooctane, DMF and MF) are shown in Figure 7-1 (hereafter isooctane is marked as ISO in the figures, TDC is referred to as 360°CA,). It is observed that MF has the highest peak pressure and fastest combustion at the IMEP of both 4.5 and 5.5 bar. DMF is between the other two, closer to isooctane. These trends have showed good agreement with the previous study (Wang, 2013, Zhong, 2010 and Daniel, 2011).

Table 7-1: Ignition delays

IMEP	Fuel	Ignition Delay ($^{\circ}$ CA) MFB0-MFB10
4.5 bar	Isooctane	32
	DMF	31
	MF	29.5
5.5 bar	Isooctane	30.5
	DMF	27
	MF	27



(a)



(b)

Figure 7-1: In-cylinder Pressures and MFB (a) IMEP 4.5bar (b) IMEP 5.5bar

DMF and MF both have shorter ignition delays (shown in Table 7-1, defined as from

spark timing to MFB10) and higher burning velocities than isooctane, thus higher thermal efficiencies can be achieved even without advancing the ignition timing. The previous thermal engine tests have discussed these in detail (Daniel, 2011, Wang , 2013, Zhong , 2010, Daniel, 2012a, Daniel, 2012b) so there is no further discussion of this part in the current paper.

7.4 Flame Propagation

7.4.1 Flame Luminance

The images in Figure 7-2 show faster flame propagation towards the exhaust valves due to the higher local temperature and the tumble, as shown in previously studies (Ma, 2012). DMF and MF have brighter flames than isooctane with the camera having the same gain setting. Generally, the higher flame luminance is associated with higher combustion temperatures and higher soot concentrations (He, 2008). However, the brightness of the flames of the three fuels does not directly reflect the in-cylinder temperatures in the current results. The pressure trace of DMF at the low load is very close to that of isooctane (see Figure 7-1), indicating the two cases have similar in-cylinder temperatures through the whole combustion process. Nevertheless the luminance of DMF flame is higher than that of isooctane. From chapter 6, it is known that adiabatic temperatures of MF is about 1% higher than DMF at stoichiometric state (also shown in Table 7-2), and because the pressure trace of MF is also the highest, it is confirmed that MF has the highest in-cylinder flame temperature.

But the shown luminance of MF flame here is slightly lower than that of DMF. Therefore it is believed that the dominating factor for the luminance of the flame of the test fuels might be the soot concentration and DMF's brighter flame reflects a stronger soot formation. However, an interesting contrast was found by previous thermal engine researches (Wang, 2013, Zhong, 2010 and Wu, 2011) that the exhaust emissions of PM with DMF and MF are lower than with gasoline, which was attributed to the oxygen content in the molecule. Thus it can be deduced that DMF and MF might generate more soot than isooctane does during combustion because of the circular molecular structures, but the oxygen content also promotes the oxidization process and the soot concentration also reduces faster than in the isooctane cases. These behavior differences balance out generating a low final soot quantity in the exhaust.

Table 7-2: The adiabatic flame temperatures and un-stretched laminar flame speeds of the three fuels

	Adiabatic Flame Temperature	Flame speed
MF	2342 K	3.8 m/s
DMF	2326 K	3.2 m/s
Isooctane	2270 K	2.9 m/s

*Pressure 1 bar, initial temperature 90°C, stoichiometric

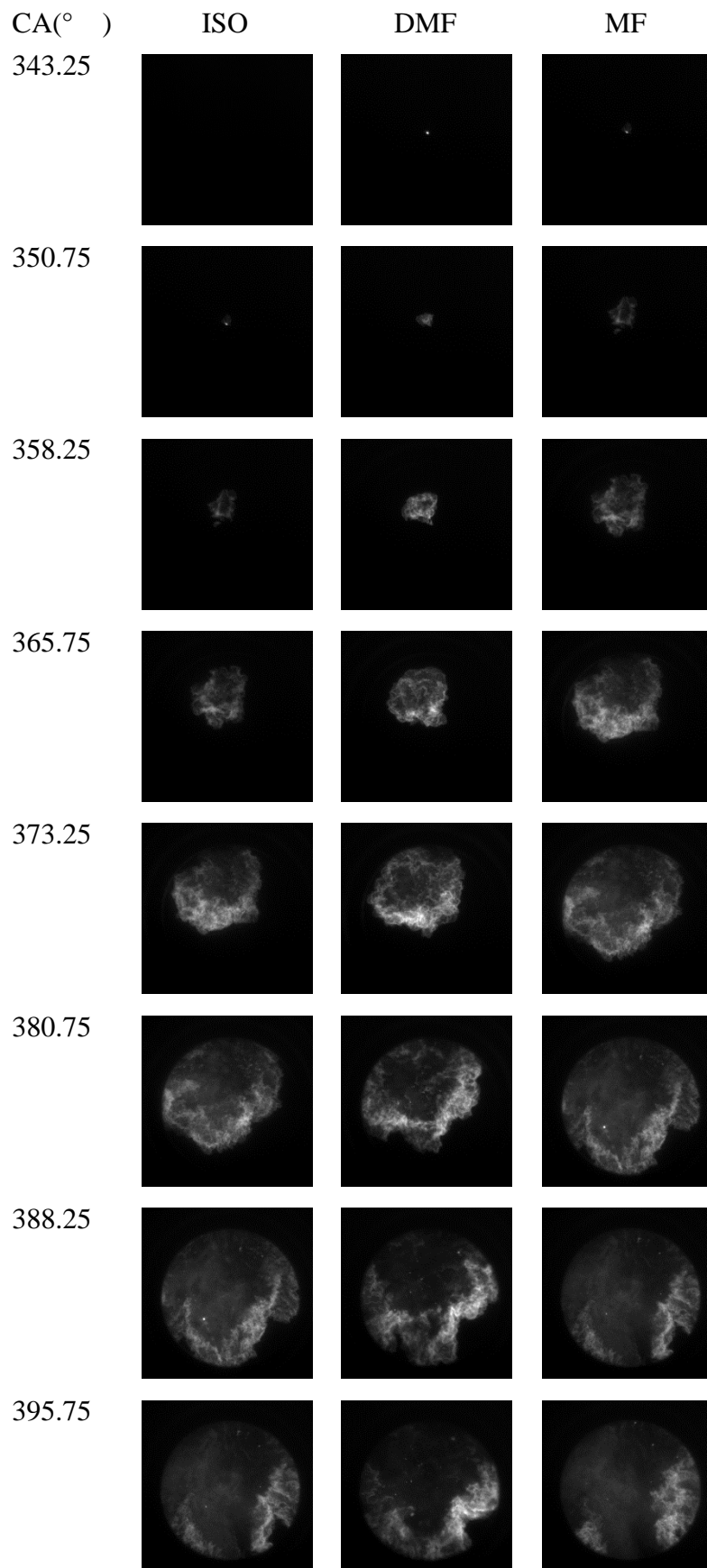


Figure 7-2: Single cycle images

7.4.2 Flame Area vs MFB

Figure 7-3 a and b present the average flame area growths and the MFB data at the loads of IMEP 4.5 and 5.5 bar respectively. The dash-dot lines are the normalized flame areas and the solid lines are MFB data from Figure 7-1. The errors for over 90% of the data points (error bar not included for clarity of the figure) are lower than $\pm 7.25\%$, and some points ($<10\%$) at the very early or late stages produced larger errors up to $\pm 16.5\%$.

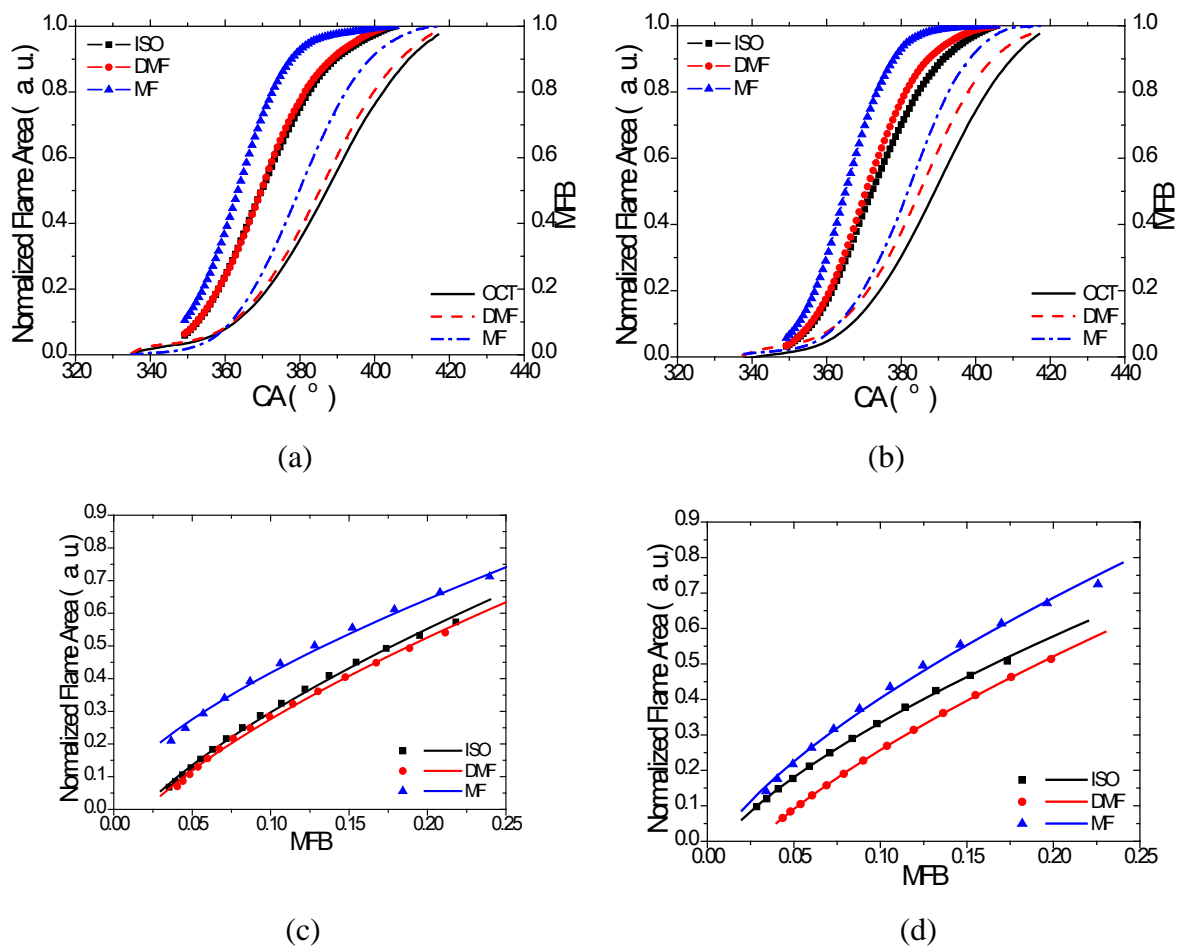


Figure 7-3: Flame area and MFB data analyses (a) MFB and normalized area at IMEP 4.5bar (b) MFB and normalized area at IMEP 5.5bar (c) Correlation between flame area and MFB (4.5bar) (d) Correlation between flame area and MFB (5.5bar)

In Figure 7-3 a, DMF and isooctane have similar flame area growths at IMEP 4.5 bar, following the trends of the MFB data. When the flame is spread over the visible area, the combustion process is at around MFB50. MF has a significantly shorter ignition delay and a faster flame area growth. The flame area growth of MF reaches 60% of the visible area more than 10°CA earlier than the other fuels. In Figure 7-3 b, the flame growth curves of DMF and isooctane show larger differences at IMEP 5.5 bar than at 4.5 bar, particularly in the later stage. It was found that, at the same spark timing, DMF had larger differences compared to gasoline in flame propagation at IMEP 3.0 bar but was similar to gasoline at IMEP 4.0 bar (Ma, 2012, Jiang, 2012). The differences between isooctane and DMF are small around IMEP 4.0 to 4.5 bar. MF's flame propagation is the fastest and all the fuels have faster rates of flame area growth at a higher IMEP (note that at 5.5 bar the spark timing is 5°CA later than at 4.5bar).

After part of the flame went beyond the visible area in the later stage, the visible boundary length started to reduce and this situation increasingly affected the results. Therefore, the flame images at the early stage (the early combustion corresponding to MFB up to 25%) are used to for correlation with the heat release data, as shown for the two engine loads in Figure 7-3 c and 7-3 d respectively. As mentioned above, the MFB is directly associated to the burned volume of the mixture, which is a cubic function of the flame propagation radius; while the flame area is a quadratic function of the flame propagation radius. Therefore the leading order of the correlation functions for the three fuels should be 2/3. Thus the correlation function is constructed

as:

$$A_{\text{flame}} = \alpha_1 V_{\text{MFB}}^{2/3} + C_1 \quad (2)$$

where A_{flame} is the flame area, V_{MFB} is the MFB value, α_1 and C_1 are coefficients (the values are given in Table 7-3). The R-square results show that this constructed correlation function fits into the experimental data very well..

Table 7-3: Fitting results for flame area-MFB

Function	$A_{\text{flame}} = \alpha_1 V_{\text{MFB}}^{2/3} + C_1$			
IMEP		α_1	C_1	R-square
4.5 bar	Isooctane	1.927	-0.08089	0.9991
	DMF	2.086	-0.1923	0.9999
	MF	2.237	-0.07849	0.9958
5.5 bar	Isooctane	2.023	-0.1392	0.9968
	DMF	1.971	-0.1484	0.9971
	MF	1.781	0.03369	0.994

In function Equation 2, a higher temperature leads to a higher value of α_1 at the low load but the tendency is opposite at the high load, the values are all around 2.0. Therefore, α_1 is related to both the temperature and the fuel property, but the combustion system design is the dominating factor. In theory, C_1 should always be zero since the heat release starts with the flame propagation. However, the pole of the spark plug shields part of the initial flame, resulting in some errors in the fittings. This explains the reason why most of the flame area growth at the beginning is behind the MBF starting point. At the same time, the equivalence ratio of the local mixture is subject to cycle-to-cycle variations, leading to relatively larger errors in the flame measurement. It is also found that C_1 is related to the fuel type, as MF always has the highest C_1 while DMF has the lowest. This is because the ignition and initial flame

propagation of MF is the fastest and DMF is relatively more difficult to ignite, which is also indicated by the flash point data in Table 1.

7.4.3 Flame Speed vs ROHR

Figure 7-4 a and 7-4 b represent the flame speeds (scattering points) and the rate of heat release (lines). In all the cases, the flame speeds follow similar mono-peak profiles to the heat release rate. In Figure 7-4 a, a good linear trend is revealed in MF's flame speed on the rising side. MF has the highest flame speed of about 7.1 m/s at 365°C_A, nearly 2 m/s faster than the peaks of isooctane and DMF. The flame speed of MF at 350°C_A is about 4.2 m/s, 0.6 m/s more than that of isooctane and DMF. This means shortly after the ignition, the flame speed of MF becomes significantly faster than the other two. Additionally, MF has shortest ignition delay among the three fuels. These two reasons result in the very fast flame propagation in MF combustion, as shown in previous figures. The ROHR data show that the heat release rate of DMF is slightly higher than that of isooctane. The peak of DMF and MF is 3.5°C_A and 9°C_A earlier, and about 4% and 23% higher than that of isooctane respectively.

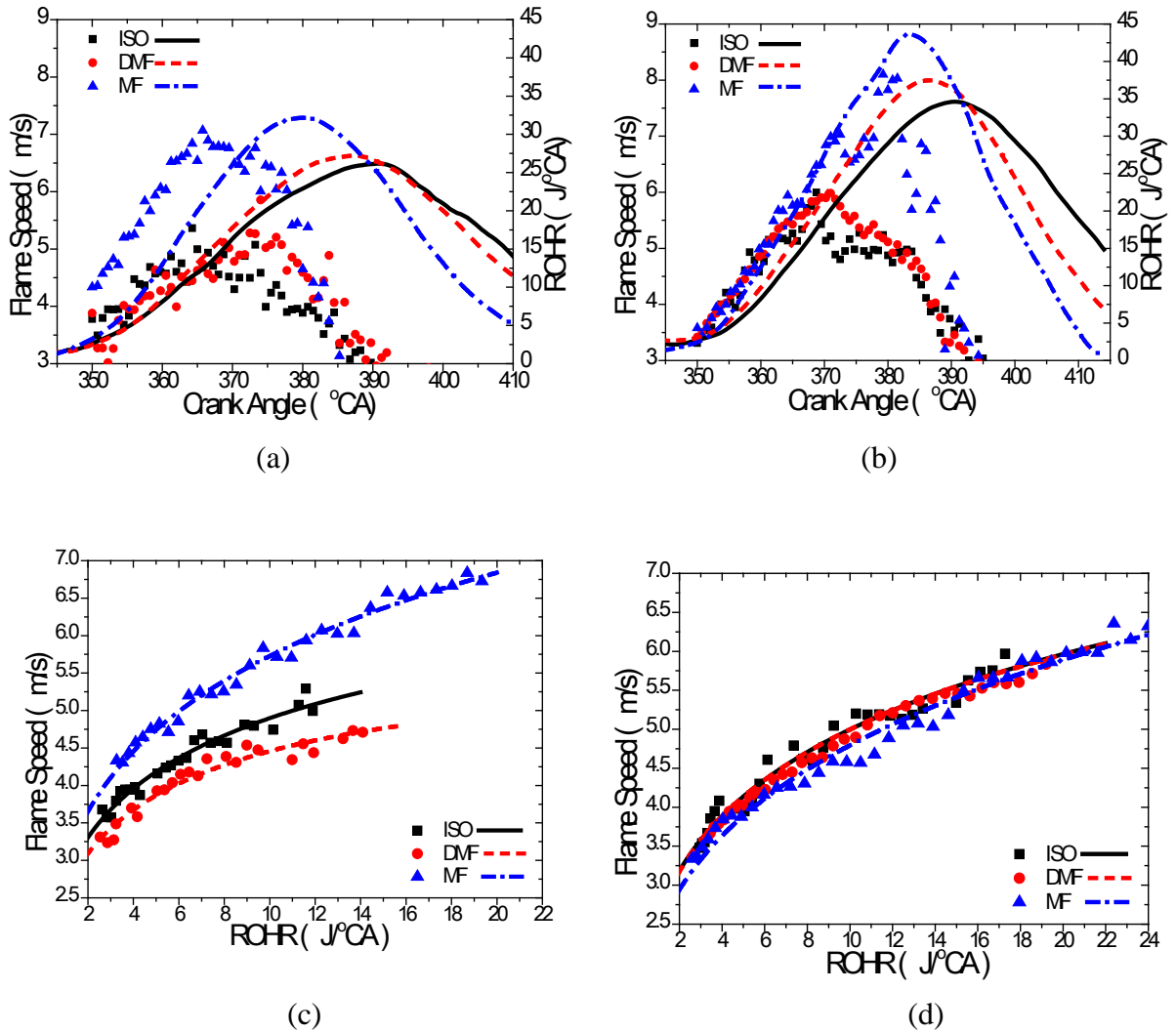
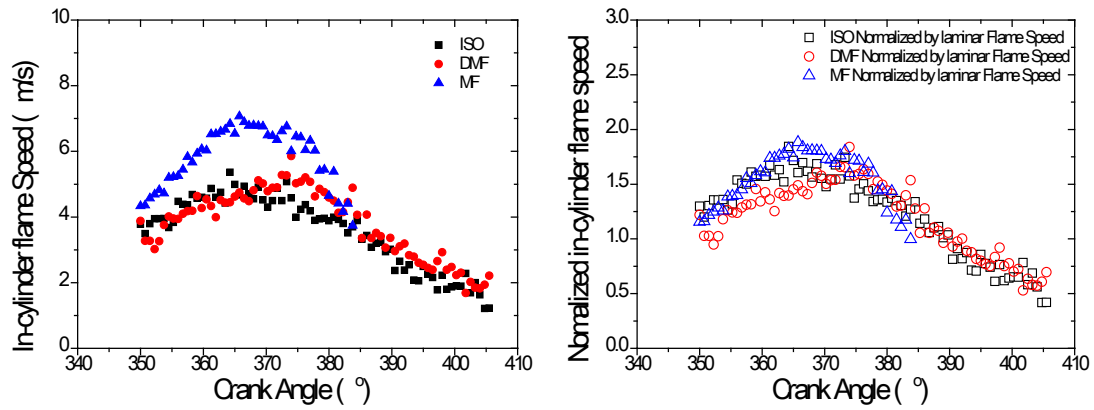


Figure 7-4: Flame speed and ROHR (a) Flame speed and ROHR at IMEP 4.5bar (b) Flame speed and ROHR at IMEP 5.5bar (c) Correlation between flame speed and ROHR (4.5bar) (d) Correlation between flame speed and ROHR (5.5bar). (Scattering points: experiment data; lines: fitting results)

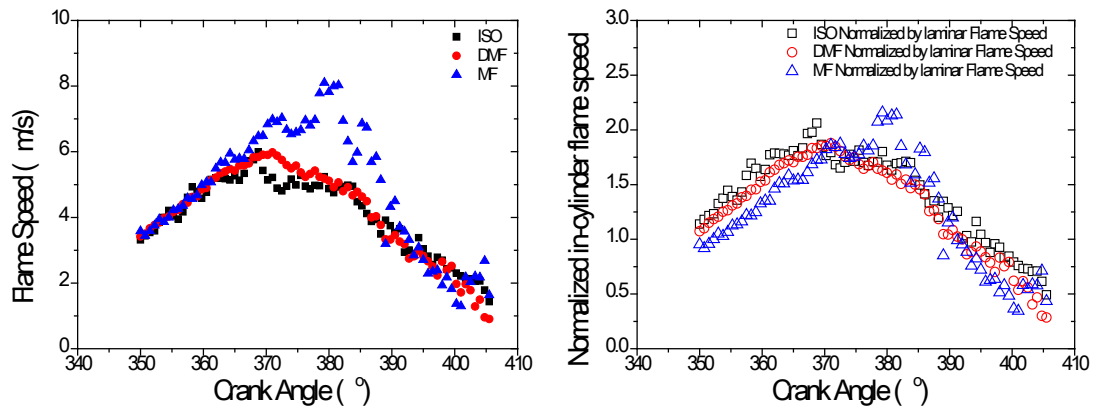
The ROHR data in Figure 7-4 b for the higher load shows significant differences among the three fuels. MF has the fastest flame speed and isooctane has the slowest. The maximum ROHR of MF is 7°CA earlier and about 26% higher than that of isooctane. Unlike the cases in Figure 7-4 a, the difference of ROHR between DMF and isooctane is larger. The maximum ROHR of DMF is 4°CA earlier and 8% higher than that of isooctane. The peak flame speed of MF in Figure 7-4 b is about 8.1 m/s.

DMF has a peak speed around 6 m/s, which is about 0.2 m/s higher than that of isooctane. At the initial stage around 350°C_A, all the three fuels have similar speeds around 3.4 m/s. Aleiferis et al. (2012a) reported similar in-cylinder isooctane flame speeds in a DISI engine. In Figure 7-4 b, all of the speed increments are quite similar to each other and clearly different from the case of IMEP 4.5 bar. This means the turbulence, which strengthens at higher loads, has a great effect on the combustion, particularly in the early stages.

The laminar flame research studies in chapter 6 showed that the un-stretched flame speed of DMF was around 3 m/s at 1 bar initial pressure at 90°C which was slightly faster than for isooctane (see Table 7-2) under this condition. In the current study, the flame speeds were quite different because the in-cylinder combustion was dominated by the turbulence, and obviously the temperatures and the pressures were much higher. The flame speeds of DMF and isooctane are closer as revealed by the laminar flame test results. A previous fundamental study of MF flame (Wu, 2011) showed that MF has higher reactivity than the other two fuels because of its chemical characteristics and this is supported by the present study as MF demonstrated the fastest combustion rate. On the other hand, if the current in-cylinder flame speed is normalized by the laminar flame speed (in-cylinder flame speed/laminar flame speed ratio) respectively, the speed curves interestingly collapse into almost one single curve, as shown in Figure 7-5. It can be concluded that, although turbulence can dominate the in-cylinder combustion, flame propagation is still greatly affected by the fuel characteristics.



(a)



(b)

Figure 7-5: The comparison of the flame speeds (a) IMEP 4.5 bar (b) IMEP 5.5 bar

When the flame front was approaching the cylinder wall, the flame propagation speed slowed down with the pressure wave reflected from the wall (Tian, 2010). Thus only the data before the peak of heat release rate, which usually corresponds to the time before the flame spreads to the whole combustion chamber (Wilson, 2005), is used to correlate with the ROHR in Figure 7-4 c and 7-4 d for the 2 engine loads. As discussed in Sec. 4.2.2, the heat release rate is correlated to the change rate of the burned volume of the mixture, while the flame speed is correlated to the changing rate of the flame propagation distance. Additionally, the correlation between the flame propagation distance and the burned volume of the mixture is a cubic function.

Therefore, the fitting function is constructed with an exponent of 2/3 and an exponent of 1/3 to reflect the correlation between the flame speeds based on 2D flame front measurement and the burning rate of the mixture in volume (the heat release rate).

The function is in the following form:

$$V_{\text{SPEED}} = \alpha_2 H_{\text{ROHR}}^{2/3} + \beta_2 H_{\text{ROHR}}^{1/3} + C_2 \quad (3)$$

where V_{SPEED} is the flame speed, H_{ROHR} is the ROHR value, α_2 , β_2 and C_2 are coefficients (the values are given in Table 7-4). In theory, C_2 should be zero and constant, however considering the errors, C_2 is restricted in a range of -0.1 to 0.1. The R-square results are also given. The R-square results are still over 0.95, slightly lower than for the fitting of Equation 1, because the results include the errors from the device, method and the calculation.

Table 7-4: Fitting results for flame speed-ROHR

Function	$V_{\text{SPEED}} = \alpha_2 H_{\text{ROHR}}^{2/3} + \beta_2 H_{\text{ROHR}}^{1/3} + C_2$				
IMEP		α_2	β_2	C_2	R-square
4.5 bar	Isooctane	-0.3765	3.068	0.036	0.9575
	DMF	-0.45	3.064	-0.0556	0.9505
	MF	-0.2345	3.125	0.08512	0.9836
5.5 bar	Isooctane	-0.2072	2.735	0.0665	0.9649
	DMF	-0.2237	2.802	0.00167	0.9635
	MF	-0.0809	2.35	0.10756	0.9754

At the load of IMEP 5.5 bar, the three lines tend to overlap within a small range but in the cases of IMEP 4.5 bar they are more separated. As the exponent 2/3 represents the 3D-to-2D projected results of the flame imaging, the values of α_2 mainly relate to the engine specification. The impact of turbulence is more obvious, which is revealed by β_2 , showing that their values for the three fuels are close to each other at the same loads but are different at varied loads, respectively. Also, it should be noted that a

higher β_2 does not necessary mean higher impact of turbulence. There are an obvious differences for the values of β_2 at different loads. However, for the same load, the differences between different fuels are very small. The differences among the values of β_2 imply that the fuel properties also have considerable impacts.

A validation is given in Figure 7-6 and Table 7-5 to prove the form of Equation 3. The data of a previous flame speed study (Wei, 2012a) were extracted and fit in the same way as the current discussion. It was found that the form of Equation 3 presents good profile in the fitting. And the curves of high turbulence cases also show a concentrated tendency just like in Figure 7-4 d, which confirms the conclusion that, when the turbulence gets stronger, it becomes a dominating factor more than the fuel property does.

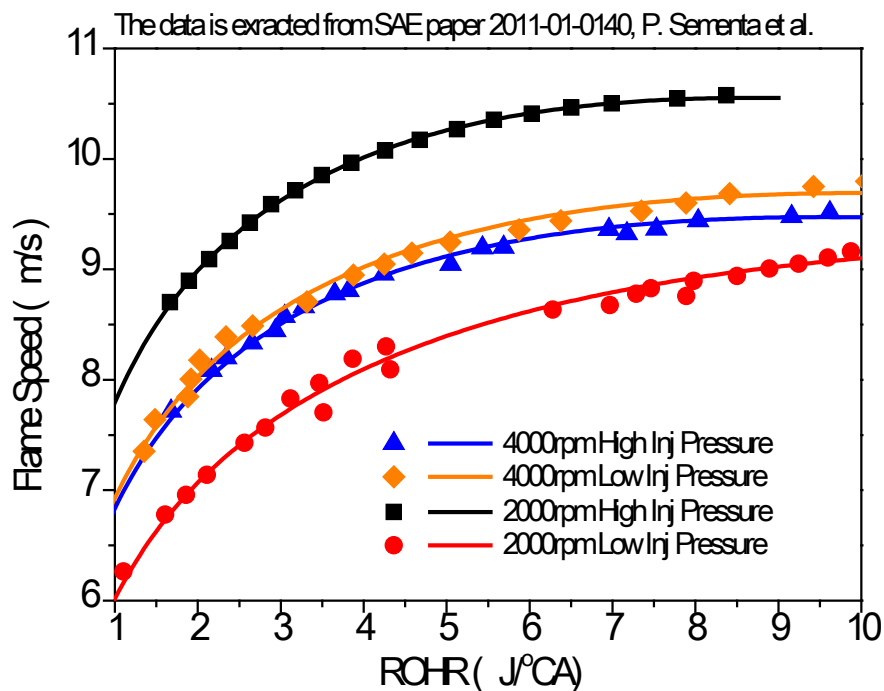


Figure 7-6: The validation for the speed-ROHR function form (Sementa, 2011)

Table 7-5: The parameters for the fittings in Figure 7-6

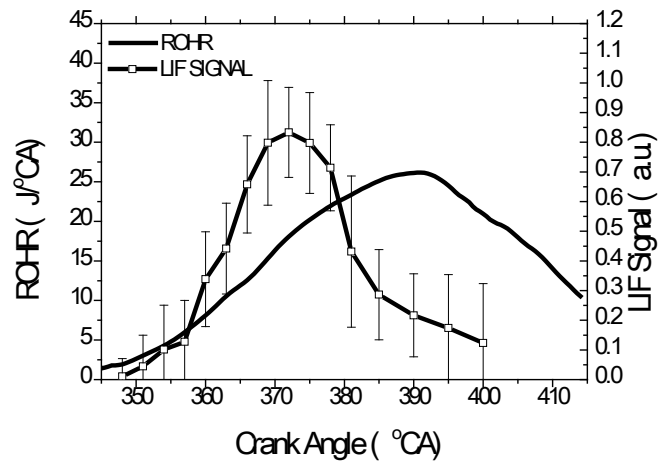
Function	$V_{\text{SPEED}} = \alpha_2 H_{\text{ROHR}}^{2/3} + \beta_2 H_{\text{ROHR}}^{1/3} + C_2$				
RPM		α_2	β_2	C_2	R-square
2000	High P_{inj}	-2.48	10.19	0.0856	0.9995
	Low P_{inj}	-1.53	7.4960	0.0519	0.9912
4000	High P_{inj}	-2.0980	8.9010	0.0325	0.9941
	Low P_{inj}	-2.0620	8.990	0.0903	0.9914

7.5 OH-LIF

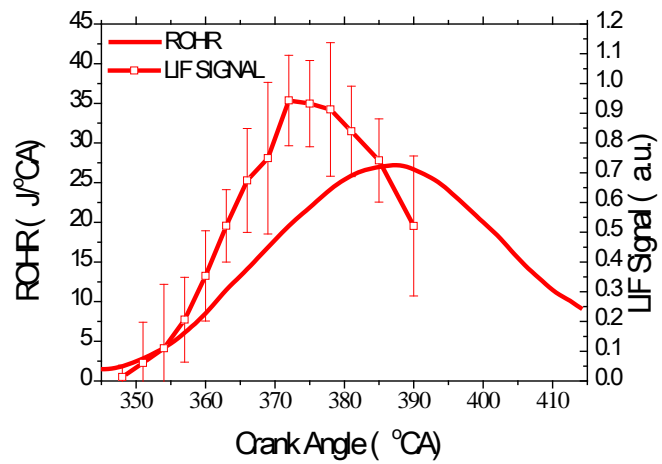
7.5.1 Effect of Fuel

Figure 7-7 presents the normalized OH-LIF signal area compared with the heat release rate. As discussed in chapter 3.5.5, the laser sheet is projected into the engine cylinder at 9 mm below the spark plug via a small side window on the optical engine. In this study, the area of the LIF signal under the same threshold is measured to indicate the LIF signal. The total area which the laser covers in the cylinder is normalized as 1 and the ratio of the LIF signal area to the total area is called the “Normalized LIF signal”. The LIF signal is normalized statistically by averaging the OH area using the same threshold so the results can be compared directly to each other. The method is described in section 3.5.5. Error bars representing the normalized deviations are given at each point, which show the variations of the OH signal area due to the cycle-to-cycle variations of the SI combustion. Larger deviations appear in the later stage after 360°CA when the flame front went beyond the laser area. The area of OH signal appearance always reaches the peak before the ROHR maximum and then decreases. It must be noted that the combustion area inside the laser sheet is only a small part of the combustion chamber, thus the descending of the OH signal does not necessarily mean that total OH in the whole engine cylinder is reducing after the

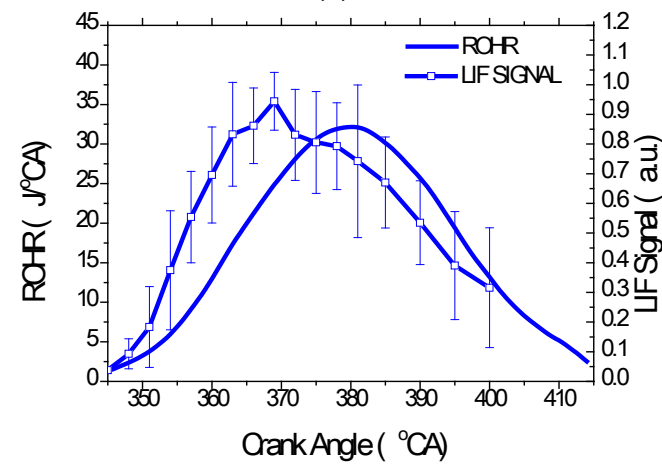
flame goes beyond the piston window but it does indicate the status of OH concentration within the visible area.



(a)



(b)

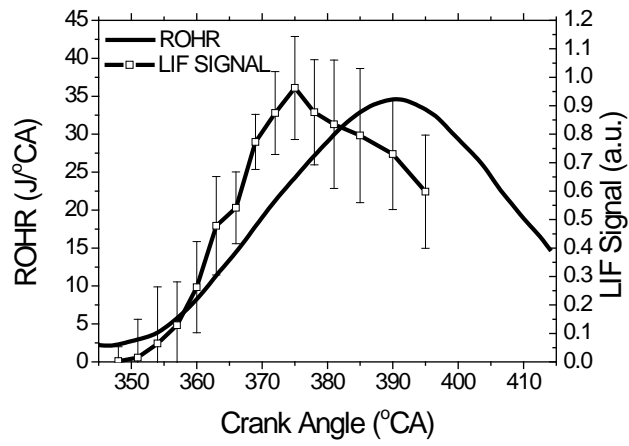


(c)

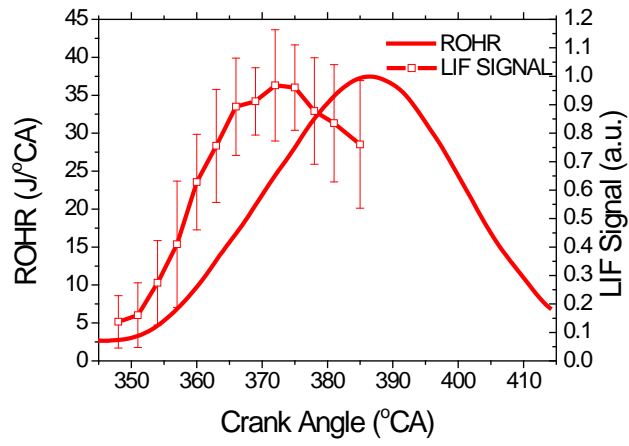
Figure 7-7: ROHR and Normalized LIF Signal (IMEP=4.5bar) (a) Isooctane (b) DMF (c) MF

The OH signal areas of isooctane (Figure 7-7a) and DMF (Figure 7-7b) have similar rising trends at the load of IMEP 4.5 bar. This matches the in-cylinder pressure trace data analyzed above. However the peak value of the OH area with DMF is 10% higher than with isooctane, and this reflects the higher combustion temperature of DMF. The OH in the MF flame (Figure 7-7c) increases significantly faster than the other two and the maximum OH area of MF is at the same level as that of DMF, but the time is about 3°CA earlier as a result of the fast chemical reaction in MF combustion.

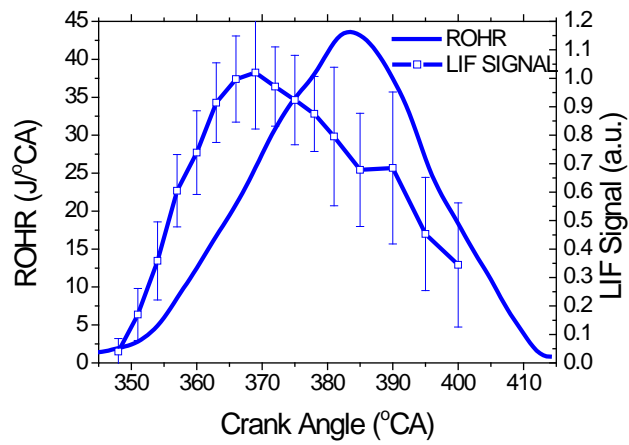
Figure 7-8 shows the ROHR and the normalized LIF signal at a load of IMEP 5.5 bar. The scale of the LIF signal in Figure 7-8 is the same as that in Figure 7-7. Increasing errors of the LIF signal data at the later stage are also observed. The OH-LIF signal data show that the three fuels have larger differences at the load of IMEP 5.5 bar. Figure 7-8 a and 7-8 b shows the maximum OH areas of DMF and isooctane are again quite close, but the peak of DMF is earlier showing the earlier heat release. The OH area in the MF flame (Figure 7-8 c) has increased fastest and the peak is the highest and the earliest.



(a)



(b)



(c)

Figure 7-8: ROHR and Normalized LIF Signal (IMEP=5.5bar) (a) Isooctane (b) DMF (c) MF

It has been known that more OH leads to a fiercer reaction because OH is one of the most important radicals in breaking the carbon chains and C-H bonds, as well as in oxidizing the carbon and hydrogen atoms. The energy released in these processes is a large percentage of the total energy release of the entire combustion process, making the OH radical signal representative of the high temperature reaction area. From the analysis of the OH and ROHR data above, it can be concluded that molecular structure plays an important role in these reactions. Although the circular structures of DMF and MF seem to be more stable than the carbon chain structure of isooctane, the CH₃- radicals in the reaction during their combustion are actually much more reactive than the CH₃- and -CH₂- radicals with isooctane combustion (Wei, 2012b). The CH₃- structure in the DMF and MF molecules can more readily lose an H- radical, which may become an OH radical later, promoting the reaction. Furthermore, the unsymmetrical structure of MF makes it even easier to lose an H- radical from the CH₃- side of the molecule, which is reported in a previous fundamental research study (Friese, 2013). Besides, MF has a lower molecular weight than DMF, which also promotes the mass transfer in the combustion process and accelerates the combustion reactions.

7.5.2 Effect of Load

Figure 7-9 summaries all of the OH-LIF data from the previous figures. The reactivity of DMF is between MF and isooctane as discussed in the previous section, but clearly the load (temperature and pressure) has a larger impact on DMF's OH distribution than for the other two fuels. The OH signal of DMF appears much faster at higher

loads than at low loads and the difference for DMF is more significant. This indicates that the variation of ignition delay for DMF caused by the load increase is the largest, in line with the heat release results (see Table 7-1).

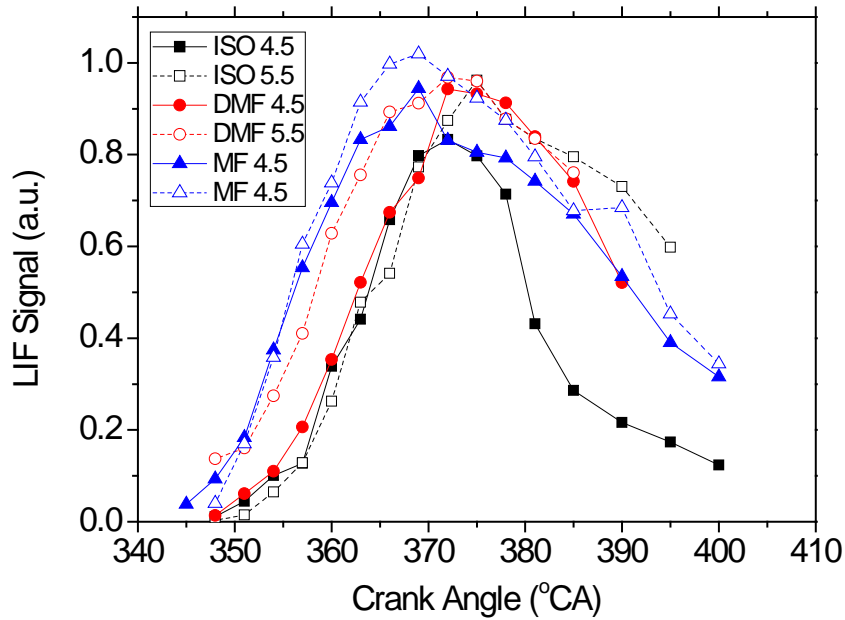


Figure 7-9: Normalized LIF Signal

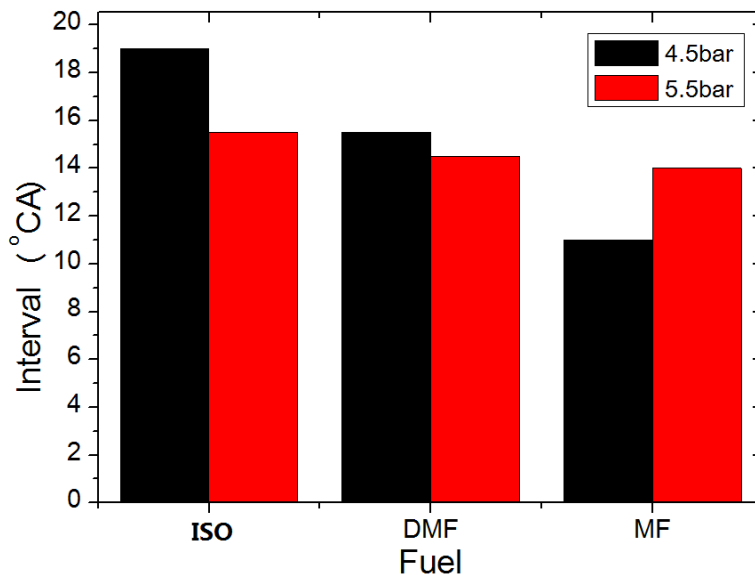


Figure 7-10: Interval between the OH and ROHR peaks with IMEP 4.5 bar and 5.5 bar

Figure 7-10 shows the intervals between the OH area peaks and the ROHR peaks at

the two different loads (from Figure 7-8). At the load of IMEP 4.5 bar, the intervals between the ROHR peaks and LIF signal peaks are 19°CA, 15.5°CA and 11°CA for isooctane, DMF and MF respectively. In the case of IMEP 5.5 bar, the intervals are 15.5°CA, 14.5 °CA and 14°CA respectively. Although the IMEP increased by only 1.0 bar, the interval between the peaks of OH and ROHR have changed significantly. The differences between the three fuels are much smaller at 5.5 bar IMEP, where all the intervals are between 14 and 15.5°CA. The interval with MF increases and the other two decrease with load. This indicates that the ignition delay of MF is more sensitive to the in-cylinder condition (pressure and temperature) associated with engine load. Thus the initial heat release retards more significantly than with that of the other two fuels at IMEP 5.5 bar, resulting in a shorter interval. It appears that when the load increases with a given fuel, the in-cylinder condition (turbulence, pressure and temperature) starts to play a more pronounced role in the flame development which partially offsets the effect of fuel characteristics.

7.5.3 Correlations among OH Distribution, Flame Area and MFB

Figure 7-11 shows the correlations of OH-LIF signal with MFB and the flame area before MFB20 (for the reason explained earlier about the visible flame area, in section 4.2.1) and curved profiles of the fitting lines can be observed. The data errors or deviations in the early stages were relatively large because the initial flame areas were small and in later stages near MFB20, the flame in some cycles had already gone out of the visible area, reducing the observed growth rates of the OH areas.

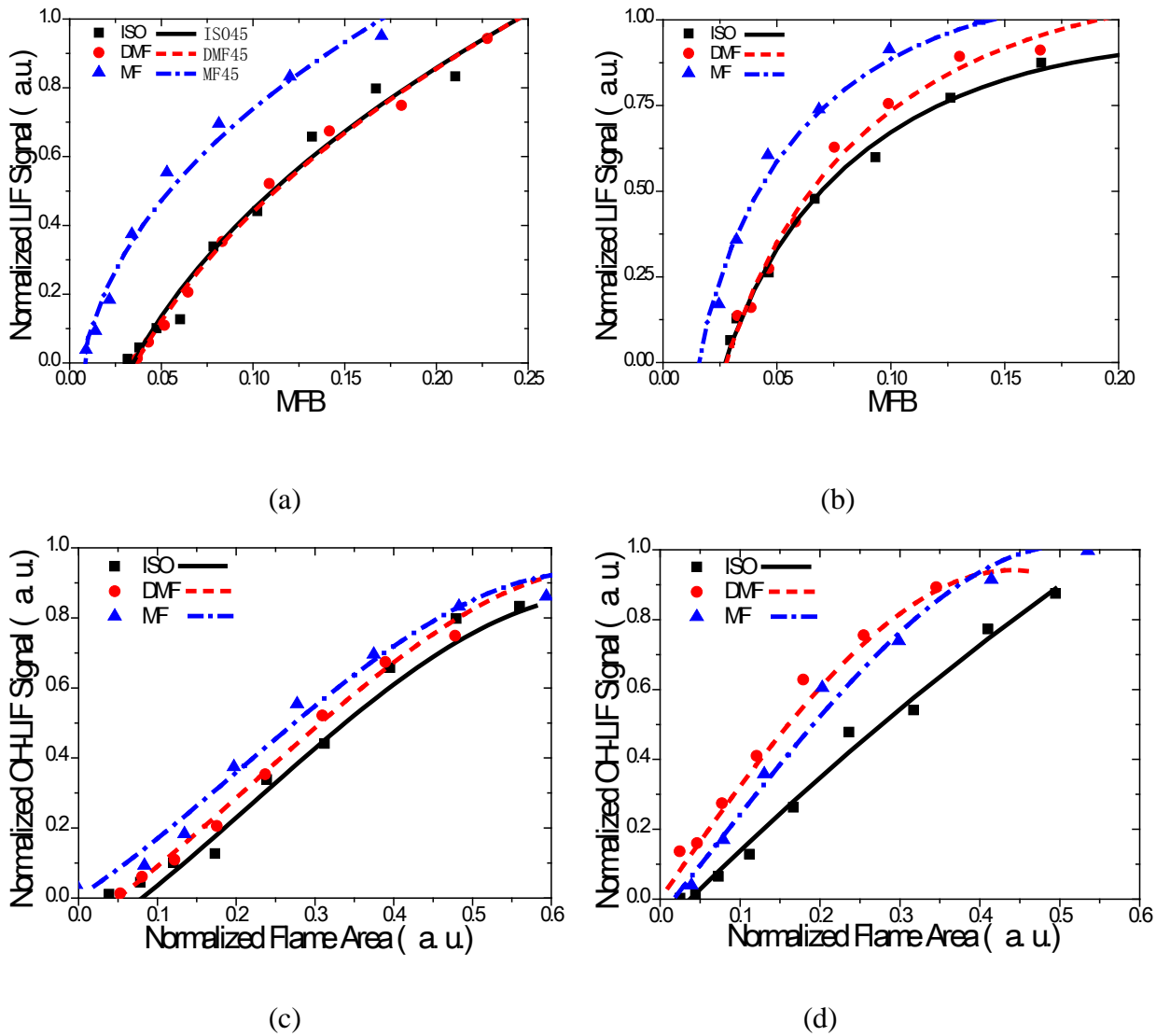


Figure 7-11: Correlations among LIF signal, MFB and flame area (a) OH-LIF versus MFB at IMEP 4.5bar (b) OH-LIF versus MFB at IMEP 5.5bar (c) OH-LIF versus Flame area at IMEP 4.5bar (d) OH-LIF versus Flame area at IMEP 5.5bar (Scattering points: experiment data; lines: fitting results)

It is predictable that when the flame is fully inside the visible range, the MFB, flame area and OH distribution should have a similar correlation to each other. Since the MFB and OH in the flame are both related to the volume of the burned mixture, the following cubic function is constructed to evaluate the OH LIF distribution, showing a correlation with MFB in isooctane, DMF and MF's combustion:

$$S_{OH} = \alpha_3 \beta_3 V_{MFB}^{2/3} + \gamma_3 \delta_3 V_{MFB}^{1/3} + C_3 \quad (4)$$

where S_{OH} is a relative value of OH distribution; V_{MFB} is the MFB value; α_3 and γ_3 are coefficients that related to the engine specifications; β_3 is related to the loads and δ_3 is a coefficient related to the fuel type. C_3 is a correction factor related to the fuel and engine load. Table 7-6 presents the fitting parameters used for Figure 7-11 a and 7-11 b. The R-square results are all above 0.975. Notice that the OH-LIF signal is normalized, the discussion of the coefficients are all based on the current relative values.

Table 7-6: Fitting results for OH-MFB

Function	$S_{OH} = \alpha_3 \beta_3 V_{MFB}^{2/3} + \gamma_3 \delta_3 V_{MFB}^{1/3} + C_3$				
IMEP		$\alpha_3 \beta_3$	$\gamma_3 \delta_3$	C_3	R-square
4.5 bar	Isooctane	0.6946	2.675	-0.944	0.9768
	DMF	0.672	2.752	-0.9834	0.9935
	MF	0.673	2.22	-0.437	0.9838
5.5 bar	Isooctane	-7.829	10.08	-2.32	0.9926
	DMF	-7.911	10.6	-2.481	0.9853
	MF	-7.916	9.72	-1.92	0.9845

Table 7-6 shows that, with a fixed engine specification, the product of α_3 and β_3 is mainly determined by the in-cylinder temperature and turbulence which are related to the load. The product of γ_3 and δ_3 shows a tendency that a faster combustion fuel has a higher value and a higher in-cylinder temperature results in larger variations, indicating the effect of the fuel property. The values of C_3 show that no OH signal appears in the initial stage, because the laser sheet is located lower than the spark plug, as introduced in the experimental setup part. The impact of fuel characteristics can be observed in the values of C_3 . For Figure 7-11 a and 7-11 b, C_3 values of MF are the highest because MF combustion has a faster flame speed and temperature rising rate,

and thus OH signal appears the fastest.

As expected, the similarity of DMF and isooctane at 4.5 bar IMEP has also appeared in Figure 7-11 a. Due to the similarity in the pressure trace results, the two lines almost overlapped. In Figure 7-11 b, the three lines for the higher load remain in the same order but the lines of DMF and isooctane are more separated than in Figure 7-11 a for the lower load. The incline angles (indicator of the first degree correlation between the amount of burned mixture and the LIF signal) for all the fuels remain similar in the initial stages before MFB10, and this observation is in agreement with the results in a study of in-cylinder OH chemiluminescence of flame propagation of gasoline (Sementa, 2011). Previous HCCI OH-LIF studies (Collin, 2003, Hildingsson, 2005) also showed similar trends in the correlations of MFB and LIF signal in the flame propagation stages. Based on the data above, it is can be concluded that in the early stage of in-cylinder SI combustion, OH can indicate the MFB of the three fuels in a relative scale. A validation of Equation 4 is shown by Figure 7-12 and the results show a good correlation in the constructed function form between the heat release rates and the OH signals.

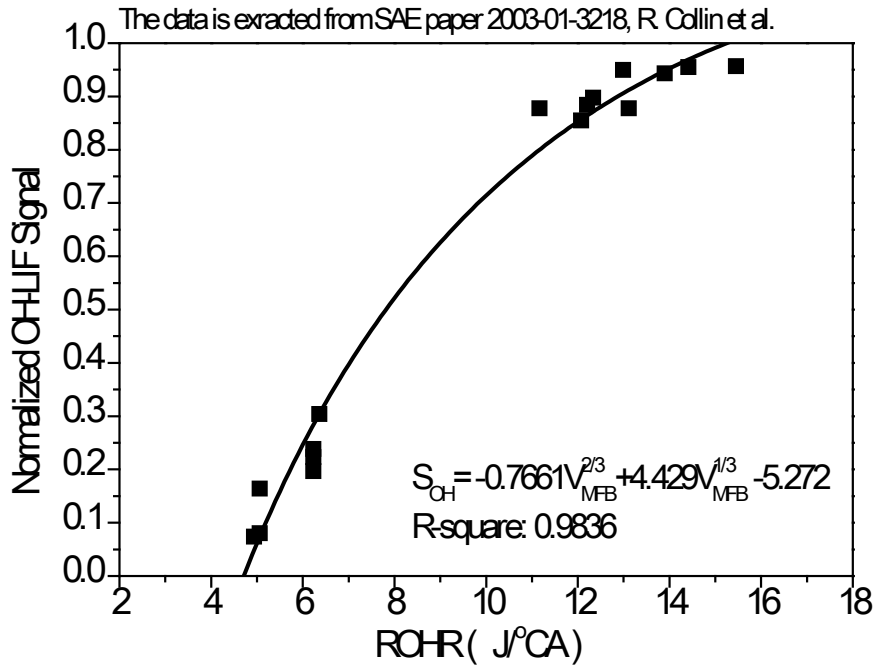


Figure 7-12: The validation for the LIF-MFB function form (Collin, 2003)

Figure 7-11 c and 7-11 d are the correlations between OH-LIF and flame area growth. The solid lines in the figure are the fitting results for the scattering points. At the load of 5.5 bar IMEP, the initial incline angles are larger than those for 4.5 bar IMEP, and the change with MF is the most significant. Although the OH area can be deduced from Equation 2 and Equation 4, an accurate description of the turbulent combustion process using empirical models is not straightforward. Based on the flame propagation data and the OH-LIF results, a cubic function has been constructed to predict the OH distribution area from the flame images:

$$S_{OH} = \alpha_4 A_{flame}^3 + \beta_4 \gamma_4 A_{flame}^2 + \delta_4 \epsilon_4 A_{flame} + C_4 \quad (5)$$

where S_{OH} is a relative value of OH distribution; A_{flame} is the flame area and the others are coefficients.

Table 7-7: Fitting results for OH-Flame

Function	$S_{OH} = \alpha_4 A_{flame}^3 + \beta_4 \gamma_4 A_{flame}^2 + \delta_4 \varepsilon_4 A_{flame} + C_4$					
IMEP		α_4	$\beta_4 \gamma_4$	$\delta_4 \varepsilon_4$	C_4	R-square
4.5 bar	Isooctane	-3.3898	2.2728	1.4901	-0.1025	0.9845
	DMF	-3.3920	2.3272	1.4889	-0.0783	0.9933
	MF	-3.3954	2.1038	1.4897	0.0037	0.9838
5.5 bar	Isooctane	-4.8528	3.0772	1.5416	-0.0538	0.9922
	DMF	-4.8517	-0.5762	3.3328	0.00	0.9927
	MF	-4.8820	1.185	2.609	0.0002	0.9883

Table 7-7 presents the fitting coefficients used for Figure 7-11 c and 7-11 d. The R-square results are all above 0.983. The variation of the coefficients with load is significant in the quadratic term and the one-degree term, while the leading term is relatively stable at the same load. Therefore, α_4 , γ_4 and ε_4 are used to indicate the impacts of the engine specifications and the working condition which is related to the turbulence, the in-cylinder pressure and temperature; β_4 and δ_4 are coefficients related to the fuel type. C_4 is a correction factor depending on the fuel and the working condition in relation to early flame development as faster combustion fuel always has higher C_4 , due to the faster forming of the OH. Higher temperature and in-cylinder pressure also give rise to a higher value of C_4 . The fitting test results show that although the deduction from Equation 2 and Equation 4 leads to a different form, the cubic degree function in Equation 5 is good to represent the correlation.

7.6 Summary

The characteristics of the combustion of DMF and MF compared with isooctane were studied in a direct injection SI optical engine using OH-LIF and high speed imaging

combined with in-cylinder pressure measurement and heat release analysis. MF presents significant differences with DMF and isooctane. The following conclusions were drawn from the experiment results:

1. MF has the fastest flame area growth rate and the highest peak flame speed at different temperatures and in-cylinder pressures (represented by the loads), followed by DMF. The averaged flame propagation data shows that the differences between DMF and isooctane are smaller at lower temperatures, which matches the similarities in the pressure trace data and the combustion phases. The flame speed data also represents a correlation with the previous laminar flame speed test results.
2. Flame area growth data shows significant correlations with the MFB data and the flame speed data also reveals correlations with the ROHR data in the early stage (when the flame was in the fully visible range). It is found that the differences of the fitting results among the three fuels became smaller in a condition of higher temperature (high load).
3. The OH distribution of MF has the highest peak value and time at different temperatures and pressures; DMF has the second highest. In general, higher combustion temperatures and pressures will advance the peaks of the OH signals. The difference becomes quite significant with higher temperatures and pressures. The OH LIF signal of DMF has a similar profile to that of isooctane in the majority of the early stage when the load is lower, which matched the results of the pressure traces. The load had a larger impact on

the OH results of DMF, due to the variations in the evaporation of DMF which was related to the in-cylinder temperature.

4. The ROHR trends match the OH distributions well before the flame went out of the visible range. The intervals between the peaks of ROHR and OH distribution increase in the order of MF, DMF and isooctane. It is also found that the intervals change and the difference among the three fuels become less at the higher load due to the impact of turbulence.
5. MFB and OH-LIF results are correlated with a fitting function with an exponent of $2/3$ and show that OH signal matches the MFB data well, thus OH can indicate the MFB of the three fuels in relative values. The flame area and the OH-LIF signal reveal cubic function correlations at different loads respectively. The fitting results show that combustion temperature is an important factor in both of the evaluations.
6. The most important contribution of this work is that 4 empirical functions have been constructed. These functions reveal the close link between the flame images in 2-D form and the combustion parameters in the cylinder (e.g. heat release, MFB). They potentially offer an alternative way to estimate the combustion in the cylinder (e.g. heat release, MFB) using photography method rather than using the pressure data.

Chapter 8

Conclusions

The main aim of this thesis was to explore the spray and combustion characteristics of the furan gasoline alternatives: MF and DMF. Their characteristics were compared to gasoline and other fuels in order to gain better understanding of these two bio-fuels. Some of the previous studies conducted by the author's group (Daniel, 2012a, Daniel, 2012b and Wang, 2013) show that these fuels have good engine performance, better knock suppression ability, compared to gasoline and acceptable engine out emissions. However, in order to eventually apply these furan bio-fuels in IC engines, more profound knowledge regarding to the fuels' injection, atomization and flame propagation in both static and dynamic conditions is needed. Thus the author is motivated by this aim to perform the following studies: macroscopic spray analysis, droplet size and velocity analysis, laminar flame propagation analysis and turbulent flame behaviour analysis. The main conclusions from this work are presented in this chapter, followed by suggestions and recommendations.

8.1 Summary and Conclusions

8.1.1 Macroscopic Spray Characteristics

The macroscopic spray characteristics were studied using the high speed imaging technique. At the nominal conditions (150 bar injection pressure, 20 °C ambient temperature, 1 bar back pressure), it was observed that the spray forms of the 5 fuels

were very similar in terms of shape and penetration length. As the back pressure increased (other conditions kept the same), the penetration length of all 5 fuels decreased significantly due to higher drag force from the air. However, it was found that the fuels with higher densities (e.g. MF) tended to have a better resistance to the decrease due to their higher inertial. When the ambient temperature went to 60°C, the penetration lengths of all fuels slightly decreased in the absence of “spray collapse”. As the ambient temperature further increased to 90°C, the “collapse” of the spray led to dramatic decrease of the penetration length for MF, ethanol and gasoline. It was also observed that for single component fuels, higher surface tension led to smaller spray cone angle. For instance, DMF had the highest surface tension at the nominal conditions and this led to the smallest spray cone angle.

Overall, the combined effects of the fuels’ properties and the ambient conditions were of vital importance to the spray characteristics of the fuel injection. If MF and DMF were going to be used in the automotive engine, the differences of these fuels (e.g. higher density, higher initial boiling point and relative high surface tension) compared to gasoline should be taken into consideration. Because these would have a significant effect on the macroscopic spray characteristics which would in turn affect the engine performance.

8.1.2 Droplet size and Velocity Measurement

PDPA was used to measure the droplet size and velocity of the 5 fuels at different test conditions. Compared to ethanol, the droplet size of MF and DMF was more similar

to that of gasoline and isooctane at different conditions (e.g. varied injection pressures, varied back pressures). The reason that ethanol generally had a much bigger droplet size was its relatively high surface tension and dynamic viscosity which would result in higher Weber number and Reynolds number.

The order of the droplet size of the 5 fuels varied under different test conditions due to the combined effects of inertial force (represented by Reynolds number) and the external disruptive aerodynamic force (represented by Weber number).

The SMD values for both MF and DMF decreased by around 5% at most distances when the back pressure increases from 1 bar to 3 bar. And the SMD values of the two fuels increased by around 30% to 50% when the back pressure increased from 3 bar to 7bar. This meant the dominant factor affecting between 1 bar and 3 bar was the increase of the shear force and as the pressure continues to increase the main effect became the spray jet deceleration.

The main effect of the vessel temperature on the droplet size and the velocity was linked to the fuel's flash boiling point. If the vessel temperature was higher than the fuel's flash boiling point, the droplet velocity would fall dramatically due to "collapse" of the spray. With the increase of the surrounding temperature, the SMD values of MF and DMF decreased.

Overall, the differences of the fuel properties led to different droplet size orders for the fuels at different test conditions. It should be note that the alternative fuels, MF and DMF, did have similar droplet sizes at various test conditions compared to the benchmark gasoline and isooctane. This was a good sign for them to be used in

current GDI engines.

8.1.3 Laminar Flame Propagation

Schlieren photography was used to study the laminar burning characteristics of MF and DMF compare to that of isooctane. The unstretched flame speed of MF was up to 30% faster than that of DMF and up to 50% faster than that of isooctane. Unsurprisingly, the laminar burning velocity of MF was also found to be the highest amongst the 3 fuels (around 15%-25% faster than DMF and 30%-45% faster than isooctane). It was also found that the flame of MF was not as stable as the other fuels due to its higher diffusion-thermal instability, which is characterized by its shorter Markstein length; and its higher hydrodynamic instability, which is characterized by its slightly higher density ratio and the smaller flame thickness.

In summary, the unstretched flame speed and the laminar burning velocity of MF were significantly faster than that of DMF and isooctane. This was very important for the understanding of the combustion behavior of MF in the engine cylinder, including its faster propagation speed, higher pressure rise rate and good knock suppression capability as reported in the literature.

8.1.4 Turbulent Flame Behaviour in a Modern GDI Engine

The combustion characteristics of DMF and MF compared with isooctane were studied in a DISI optical engine using OH-LIF and high speed imaging combined

with in-cylinder pressure measurement and heat release analysis. Four empirical functions have been constructed.

For combustion in the engine cylinder, MF behaved very differently compared to the other two fuels. It had the fastest flame area growth rate and the highest peak flame speed in the cylinder at different loads compared to the other fuels. The correlation of the flame speed data with the previous laminar flame speed data indicated that the laminar flame characteristics of the fuels played a key role on affecting the in-cylinder flame propagation.

At both loads (IMEP 4.5 bar and 5.5 bar), the area of the OH distribution of MF has the highest peak and earliest emerging timing; DMF has the second highest. Their MFB and OH-LIF results were correlated with a fitting function with an exponent of $2/3$. The function showed that OH signal matched the MFB data well; thus OH can indicate the MFB of the three fuels in relative values.

Overall, the combustion of MF was much faster than that of DMF and isooctane at the same load and this was discovered from both the flame images and the heat release analysis. The four functions constructed revealed the close link between the flame in 2-D form and the combustion parameters in the cylinder (e.g. heat release, MFB). They offered alternative ways to estimate the combustion process and combustion parameters in the cylinder (e.g. heat release, MFB) using photography method (e.g. high speed imaging and OH LIF) rather than using the pressure data.

8.2 Future Work

This work studied the characteristics of the furan bio-fuels, in particular MF and DMF, on the aspects of spray and combustion. In order for these fuels to become commercialized, more research is required to gain more understanding of the behaviour of the spray and combustion. The author here presents some recommendations for future work.

8.2.1 Spray Characteristics

The spray characteristics of the furan bio-fuels can be studied in an optical engine using various techniques (e.g. PLIF, high speed imaging) in order to discover their macroscopic spray characteristics under real engine conditions. Comparison can be made between these fuels and gasoline. The effect of the engine operating conditions on the spray can be explored. These data can be used to explain the combustion and emissions' behaviour. Also, this research can be useful for the design of engines, especially for the furan bio-fuels.

8.2.2 Laminar Flame Propagation

The present work studied the laminar burning characteristics under 1 bar condition and different initial temperatures using schlieren photography. However, more work can be done to understand the laminar burning characteristics under diluted conditions or pressurized conditions. These tests can provide more fundamental knowledge for

MF and DMF.

8.2.3 Combustion Behaviour in the Engine

The NO_x emissions for MF and DMF are worse than those of gasoline and ethanol, even though they have advantages on knock suppression and efficiency (Wang, 2013).

In order to utilize these fuels in an IC engine, EGR could be used as the NO_x reduction method. Thus, the study of EGR on the combustion behaviours can be carried out. It is important to understand the EGR rate and the turbulent flame propagation in the engine.

List of References

Aleiferis, P. Malcolm, J. Todd, A. 2008. An Optical Study of Spray Development and Combustion of Ethanol, Iso-Octane and Gasoline Blends in a DISI Engine. SAE Technical Paper 2008-01-0073.

Aleiferis, P. and Rosati, M. 2012a. Flame chemiluminescence and OH LIF imaging in a hydrogen-fuelled spark-ignition engine. *International Journal of Hydrogen Energy* 37:1797-1812

Aleiferis P and Rosati M. 2012b. Controlled autoignition of hydrogen in a direct-injection optical engine. *Combustion and Flame* 159:2500-2515

Aleiferis, P. and Romunde, Z.R.Van. 2013. An analysis of spray development with iso-octane, n-pentane, gasoline, ethanol and n-butanol from a multi-hole injector under hot fuel conditions. *Fuel* 105(2013) 143-168

Barnett, H. C., & Hibbard, R. R. 1957. Basic considerations in the combustion of hydrocarbon fuels with air.

Basshuysen, R.V. 2009. Gasoline engine with direct injection. Berlin: MercedesDurck.

Bechtold, J. K. Matalon, 2001. M. The dependence of the Markstein length on stoichiometry. *Combustion and Flame*. 127:1906–13.

Berntsson, A. Andersson, M. Dahl, D. 2008. A LIF-study of OH in the Negative Valve Overlap of a Spark-assisted HCCI Combustion Engine. SAE Technical Paper 2008-01-0037.

Bradley, D. Hicks, R.A. Lawes, M. Sheppard, C.G.W. Woolley, R. 1998. The measurement of laminar burning velocities and Markstein numbers for iso-octane–air and isooctane isooctane- n-heptane–air mixtures at elevated temperatures and pressures in an explosion bomb. *Combustion and Flame*. 115:126–44.

Broustail, G., Seers, P., Halter, F., Moréac, G., & Mounaïm-Rousselle, C. 2011. Experimental determination of laminar burning velocity for butanol and ethanol iso-octane blends. *Fuel*, 90(1), 1-6.

Burke, M. P. Chen, Z. Ju, Y. Dryer, F.L. 2009. Effect of cylindrical confinement on the determination of laminar flame speeds using outwardly propagating flames. *Combustion and Flame*. 156:771–9.

Celik, M.B. 2010. Gasoline Direct Injection. [Oline Available from: <http://cdn.intechopen.com/pdfs-wm/11336.pdf> [Accessed: 02/04/2014]

Chen, R. 2011. Cold-start emissions of an SI engine using ethanol–gasoline blended fuel. *Applied Thermal Engineering* 31.8 (2011): 1463-1467.

Collin, R. Nygren, J. Richter, M. 2003. Simultaneous OH- and Formaldehyde-LIF Measurements in an HCCI Engine. SAE Technical Paper 2003-01-3218.

Daniel, R. Tian, G. Xu, H. Wyszynski, M. L. 2011. Wu, X.; Huang, Z. Effect of spark timing and load on a DISI engine fuelled with 2,5-dimethylfuran. *Fuel*. 90 (2011) 449–458.

Daniel, R. Tian, G. Xu, H. 2011. Effect of spark timing and load on a DISI engine fuelled with 2,5-dimethylfuran. *Fuel* 90:449-458.

Daniel, R. Tian, G. Xu, H. 2012a. Ignition timing sensitivities of oxygenated biofuels compared to gasoline in a direct-injection SI engine. *Fuel* 99:72-82

Daniel, R. Xu, H. Wang, C. 2012b. Combustion performance of 2,5-dimethylfuran blends using dual-injection compared to direct-injection in a SI engine. *Applied Energy* 98:59-68

Dantec-Dynamics. 2006. BSA Flow Software Version 4.10 Installation & User's Guide. 10th ed.

Delacourt, E. 2005. Characterisation of very high pressure diesel sprays using digital imaging techniques. *Fuel* 84(7-8): p. 859-867.

Dodge, L. G. T. Ryan, W. and M. Ryan, G. 1992. Effects of Different Injector Hole Shapes on Diesel Sprays. SAE paper 920623.

Dumouchel, C. 2008. On the experimental investigation on primary atomization of liquid streams. *Experiments in Fluids*. 45(3): p. 371-422.

Energy Statistics. 2014 [Oline Available from: <http://yearbook.enerdata.net/> [Accessed: 02/04/2014]

Farrell, P. Chang, C. and Su, T. 1996. High pressure multiple injection spray characteristics., SAE technical paper 960860.

Friese P, Simmie J, Olzmann M. 2013 The reaction of 2,5-dimethylfuran with hydrogen atoms - An experimental and theoretical study. *Proc Combust Inst*

34:233 - 9.

Galmiche, B., Halter, F., & Foucher, F. 2012. Effects of high pressure, high temperature and dilution on laminar burning velocities and Markstein lengths of iso-octane/air mixtures. *Combustion and Flame*, 159(11), 3286-3299.

Gao, Jian, Jiang, Deming. Huang, Zuohua. 2007. Spray properties of alternative fuels: A comparative analysis of ethanol-gasoline blends and gasoline. *Fuel* 86.10 (2007): 1645-1650.

Gu, X., Huang, Z., Wu, S., & Li, Q. 2010. Laminar burning velocities and flame instabilities of butanol isomers-air mixtures. *Combustion and Flame*, 157(12), 2318-2325.

Gu, X. Li, Q. Huang, Z. Zhang, N. 2011. Measurement of laminar flame speeds and flame stability analysis of tert-butanol-air mixtures at elevated pressures. *Energy Conversion and Management*. 52(2011)3137 3146.

Graf, N. Gronki, J. Schulz, C. Baritaud, T. 2001. In-Cylinder Combustion Visualization in an Auto-Igniting Gasoline Engine using Fuel Tracer- and Formaldehyde-LIF Imaging. SAE Technical Paper 2001-01-1924.

Halter, F., Tahtouh, T., & Mounaim-Rousselle, C. 2010. Nonlinear effects of stretch on the flame front propagation. *Combustion and Flame*, 157(10), 1825-1832.

Han, D. and Steeper, R. 2002. Examination of Iso-octane/Ketone Mixtures for Quantitative LIF Measurements in a DISI Engine. SAE Technical Paper 2002-01-0837.

Hasse, C. Bollig, M. Peters, N. Dwyer, H. A. 2000. Quenching of Laminar iso-Octane Flames at Cold Walls. *Combustion and Flame*. Vol. 122, No. 1-2, 2000, pp.117-129.

He, Chao. Ge, Y. Tan, J. Han, X. 2008. Spray properties of alternative fuels: A comparative analysis of biodiesel and diesel. *International Journal of energy research* 32.14 (2008): 1329-1338.

He, X. Ma, X. Wu, F. and Wang, J. 2008. Investigation of Soot Formation in the Oxygenated Fuels Flame by Laser Induced Fluorescence and Incandescence. COMODIA 2008, Sapporo, Japan.

Heywood, John B. 1988. *Internal combustion engine fundamentals*. Vol. 930. New York: Mcgraw-hill. P529

Hildingsson, L. Persson, H. Johansson, B. 2005. *Optical Diagnostics of HCCI and*

UNIBUS Using 2-D PLIF of OH and Formaldehyde. SAE Technical Paper 2005-01-0175.

Hiroyasu, H. and M. Arai, 1990. Structures of Fuel Sprays in Diesel Engines. SAE paper 900475.

Hiroyasu, H. 1985. Diesel Engine Combustion and Its Modeling. in COMODIA 85. Tokyo.

Hu, E. Huang, Z. He, J. Zheng, J. Miao, H. 2009. Measurements of laminar burning velocities and onset of cellular instabilities of methane–hydrogen–air flames at elevated pressures and temperatures. *International Journal of Hydrogen Energy*. 34(2009)5574-5584.

Huang, Z. Zhang, Y. Zeng, K. Liu, B. Wang, Q. Jiang, D. 2006. Measurements of laminar burning velocities for natural gas–hydrogen–air mixtures. *Combustion and Flame* 146:302–11.

Iwamoto, Y. 1997. Development of gasoline direct injection engines. SAE Paper 970541

Janet, Y. Earl, C. McCormick, R. 2011. Utilization of renewable oxygenates as gasoline blending components. *National Renewable Energy Laboratory (U.S. DOE)*. NREL/TP-5400-50791.

Jerzembeck, S., Peters, N., Pepiot-Desjardins, P., & Pitsch, H. 2009. Laminar burning velocities at high pressure for primary reference fuels and gasoline: Experimental and numerical investigation. *Combustion and Flame*,156(2), 292-301.

Jiang, C. Ma, X. Xu, H. 2012. An Optical Study of DMF and Ethanol Combustion Under Dual-Injection Strategy. SAE Technical Paper 2012-01-1237.

Kang, J. C. Bae and K.O. Lee. 2003. Initial development of non-evaporating diesel sprays in common-rail injection systems. *International Journal of Engine Research*. 4(4): p. 283-298.

Karlin, V. Sivashinsky, G. 2007. Asymptotic modelling of self-acceleration of spherical flames. *Proceedings of the Combustion Institute*. 31: p. 1023-1030.

Kelley, A.P, Law, C.K. 2009. Nonlinear effects in the extraction of laminar flame speeds from expanding spherical flames. *Combust Flame*156(9):1844 – 51.

Kelley, A.P, Liu W, Xin YX, Smallbone, A.J, Law, C.K. 2011. Laminar flame speeds, nonpremixed stagnation ignition, and reduced mechanisms in the oxidation of

iso-octane. Proceedings of the Combustion Institute 33:501e8.

Kenneth, G.C. Adam, J. Liska, A.J. 2007. Food and fuel for all: realistic or foolish?. *Biofuels, Bioproducts and Biorefining* 1.1: 18-23

Klein-Douwel, R.J.H. Frijters, P.J.M. Seykens, X.L.J. Somers L.M.T. and Baert, R.S.G. 2009. Gas Density and Rail Pressure Effects on Diesel Spray Growth from a Heavy-Duty Common Rail Injector. *Energy & Fuels*. 23: p. 1832-1842.

Kowalewicz, A. 1993. Methanol as a Fuel for Spark Ignition Engines: a Review and Analysis. Proceedings of the IMechE, 207, 43-52.

Law, C. K. Sung, C. J. 2000. Structure, aerodynamics and geometry of premixed flamelets. *Progress in Energy and Combustion Science*. 26:459–505.

Law, C.K. 2006. *Combustion Physics*, first ed., Cambridge University Press, Cambridge.

Lefebvre, A.H. 1989. *Atomization and sprays*. New York: Hemisphere Publishing Corporation.

Leylegian, J. C. Sun, H. Y. Law, C. K. 2005. Laminar flame speeds and kinetic modeling of hydrogen/chlorine combustion. *Combustion and Flame*. 143(2005)199-210.

Li, Yanfei. 2012. Experimental study on spray and combustion characteristics of diesel-like fuels. University of Birmingham

Liu, S. Clemente, E.R.C. Hu. T. AND Wei, Y. 2007. Study of Spark Ignition Engine Fueled with Methanol/Gasoline Fuel Blends. *Applied Thermal Engineering*, 27, 1904-1910.

Luque, R. Herrero-Davila, L. Campelo, J. M. Clark, J. H.; Luna, D.; Marinasa, J. M. Romeroa, A. A. 2008. Biofuels: a technological perspective. *Energy & Environmental Science*. 1:p. 542-564.

Ma, X. He, X. Wang, J. 2011. Co-evaporative multi-component fuel design for in-cylinder PLIF measurement and application in gasoline direct injection research. *Applied Energy* 88:2617-2627.

Ma, X. Jiang, C. Xu, H. 2012. In-Cylinder Optical Study on Combustion of DMF and DMF Fuel Blends. SAE Technical Paper 2012-01-1235.

Ma, X. Jiang, C. and Xu, H. 2013. Laminar burning characteristics of 2-methylfuran

compared with 2, 5-dimethylfuran and isooctane. *Energy & Fuels* 2013. In Press. <http://pubs.acs.org/doi/abs/10.1021/ef401181g>

Matalon, M. Matkowsky, B. J. 1982. Flames as gas dynamic discontinuities. *Fluid Mechanics*. 124:239–59.

Matalon, M. 2007. Intrinsic flame instabilities in premixed and nonpremixed combustion. *Annu. Rev. Fluid Mech.* 2007. 39:163-191

Metghalchi, M., & Keck, J. C. 1982. Burning velocities of mixtures of air with methanol, isooctane, and indolene at high pressure and temperature. *Combustion and flame*, 48, 191-210.

Meier, U. 2002. Planar temperature measurement on OH using LIF in commercial combustion systems. *Gaswaerme International*. 51:178-183.

Merola, S. Tornatore, C. Valentino, G. 2011. Optical Investigation of the Effect on the Combustion Process of Butanol-Gasoline Blend in a PFI SI Boosted Engine. SAE Technical Paper 2011-24-0057.

Nakama, K. KUSAKA, J. AND DAISHO, Y. 2008. Effect of Ethanol on Knock in Spark Ignition Gasoline Engines. SAE 2008-32-0020.

OECD. 2008. *Biofuel Support Policies: An Economic Assessment*. Paris.

Ohtomo, M. Nishikawa, K. Suzuoki, T. 2011. Miyagawa, H. Auto-ignition Characteristics of Biofuel Blends for SI Engines. SAE. 2011-01-1989.

Olofsson, J. Seyfried, H. Richter, M. 2005. High-Speed LIF Imaging for Cycle-Resolved Formaldehyde Visualization in HCCI Combustion. SAE Technical Paper 2005-01-0641.

Olikara, C. Borman, G. L. 1975. A Computer Program for Calculating Properties of Equilibrium Combustion Products with Some Applications to I. C. Engines. SAE 750468.

Pastor, J.V. Arrègle J. and Palomares, A. 2001. Diesel Spray Image Segmentation With a Likelihood Ratio Test. *Appl. Opt.* 40(17): p. 2876-2885.

Pitcher G., Wigley G. and Saffman. 1990. *Sensitivity of Drop Size Measurement by Phase Doppler Anemometry to Refractive Index Changes in Combusting Fuel Sprays', Applications of Laser Techniques to Fluid Mechanics*, Lisbon, Springer Verlag.

Reitz, R.D. and Bracco, F.B. 1979. On the Dependence of Spray Angle and Other Spray Parameters on Nozzle Design and Operating Conditions, SAE paper 790494.

Reitz, R. D., and Bracco, F.B . 1982. "Mechanism of atomization of a liquid jet." *Physics of Fluids* 25: 1730-1742.

Roman-Leshkov, R. Barrett, C. J. Liu, Z. Y. Dumesic, J. A. 2007. Production of dimethylfuran for liquid fuels from biomass-derived carbohydrates. *Nature*. 447: 982-6.

Rothamer, D. A. Jennings, J. H. 2012. Study of the knocking propensity of 2,5-dimethylfuran–gasoline and ethanol–gasoline blends. *Fuel*. 98 (2012) 203–212.

Russell, B.L. 1980. Food or fuel: new competition for the world's cropland. *Worldwatch Paper*, Worldwatch Institute 35.

Scholz, J. Wiersbinski, T. and Beushausen, V. 2007. Planar Fuel-Air-Ratio-LIF with Gasoline for Dynamic Mixture-Formation Investigations. SAE Technical Paper 2007-01-0645.

Schulz, C. Sick, V. 2005. Tracer-LIF diagnostics: quantitative measurement of fuel concentration, temperature and fuel/air ratio in practical combustion systems. *Prog Energy Combust Sci* 31:75-121.

Schwarz, C. 2006. Potential of the spray-guided BMW DI combustion system. SAE Paper 2006-01-1265

Scussei, A. 1978. The Ford PProCo engine update. SAE Paper 780669

Shell. 2011. Shell V-Power gasoline material safety data sheet, Available online from: <http://www.shell.com/content/dam/shell-new/local/corporate/trading-shipping/downloads/msds/in-country/uk-stasco/mogas-gasoline-cas-86290-81-5---stil---en.pdf> [accessed on 01/02/2015]

Serras-Pereira, J. Aleiferis, P. Richardson, D. 2008. Characteristics of Ethanol, Butanol, Iso-Octane and Gasoline Sprays and Combustion from a Multi-Hole Injector in a DISI Engine. SAE Technical Paper 2008-01-1591.

Sementa, P. Vaglieco, B. and Catapano, F. 2011. Non-Intrusive Investigation in a Small GDI Optical Engine Fuelled with Gasoline and Ethanol. *SAE Int. J. Engines* 4(1):50-66.

Smallwood, G.J. and Gulder, O.L. 2000. Views on the structure of transient diesel sprays. *Atomization and Sprays*. 10(3-5): p. 355-386.

Sick, V. 2013. High speed imaging in fundamental and applied combustion research.

Proc. Combust. Inst. 34:3509-3530.

Singh, S. Musculus, M. Reitz, R. 2009. Mixing and flame structures inferred from OH-PLIF for conventional and low-temperature diesel engine combustion. *Combustion and Flame* 156:1898-1908

Soid, S. and Zainal, Z. 2011. Spray and combustion characterization for internal combustion engines using optical measuring techniques - A review. *Energy* 36:724-741

Somers, K. P. Simmie, J. M. Gillespie, F. Burke, U. Connolly, J. Metcalfe, W. K. Battin-Leclerc, F. Dirrenberger, P. Herbinet, O. Glaude, P. A. Curran, H. J. 2013. A high temperature and atmospheric pressure experimental and detailed chemical kinetic modelling study of 2-methyl furan oxidation. *Proceeding of the Combustion Institute*. 347(2013)225-232.

Stone, R. 2012a. *Introduction to internal combustion engines*. p70. Hampshire: Palgrave Macmillan. 4th edition.

Stone, R. 2012b. *Introduction to internal combustion engines*. p285. Hampshire: Palgrave Macmillan. 4th edition.

Stone, R. 1999. *Introduction to internal combustion engine, laminar burning velocity*, 3rd Edition. London. P363-365.

Tabaczynski, R. J., Ferguson, C. R., & Radhakrishnan, K. 1977. A turbulent entrainment model for spark-ignition engine combustion (No. 770647). SAE Technical Paper.

Tesla Motors. 2014. About Tesla. [Oline] Available from: http://www.teslamotors.com/en_GB/about [Accessed: 02/04/2014]

Thewes, M. Muether, M. Pischinger, S. Budde, M.; Brunn, A. Sehr, A. Adomeit, P. Klankermayer, J. 2011. Analysis of the Impact of 2-Methylfuran on Mixture Formation and Combustion in a Direct-Injection Spark-Ignition Engine. *Energy Fuels*. 25 (12), pp 5549–5561.

Tian, G. Li, H. Xu, H. Li, Y. Raj, S. M. 2010a Spray Characteristics Study of DMF Using Phase Doppler Particle Analyzer. SAE Technical Paper. 2010-01-1505.

Tian, G. Daniel, R. Li, H. Xu, H. Shuai, S. Richards, P. 2010b. Laminar Burning Velocities of 2,5-Dimethylfuran Compared with Ethanol and Gasoline. *Energy & Fuels*. 24 (7), 3898-3905.

Turns, Stephen R. 2011a. An introduction to combustion: Concepts and Application. P285 London: McGraw-Hill Education

Turns, Stephen R. 2011b. An introduction to combustion: Concepts and Application. P282 London: McGraw-Hill Education

Turns, Stephen R. 2011c. An introduction to combustion: Concepts and Application. P275 London: McGraw-Hill Education

Turns, Stephen R. 2011d. An introduction to combustion: Concepts and Application. P457 London: McGraw-Hill Education

Turns, S. R. 1996. An Introduction to Combustion. New York: McGraw-Hill. P55-56.

Varea, E., Modica, V., Vandel, A., & Renou, B. 2012. Measurement of laminar burning velocity and Markstein length relative to fresh gases using a new postprocessing procedure: Application to laminar spherical flames for methane, ethanol and isooctane/air mixtures. *Combustion and Flame*, 159(2), 577-590.

Verbiezen, K. Klein-Douwel, R. Vliet, A. 2007. Quantitative laser-induced fluorescence measurements of nitric oxide in a heavy-duty Diesel engine. *Prog Energy Combust Sci* 31:765-773

Vukadinovic, V., Habisreuther, P., & Zarzalis, N. 2013. Influence of pressure and temperature on laminar burning velocity and Markstein number of kerosene Jet A-1: Experimental and numerical study. *Fuel*, 111, 401-410.

Wang, C. Xu, H. Daniel. R. Ghafourian, A. Herreros, J. M. Shuai, S. Ma, X. 2013. Combustion characteristics and emissions of 2-methylfuran compared to 2,5-dimethylfuran, gasoline and ethanol in a DISI engine. *Fuel*. 103 (2013) 200–211.

WEI, Y. LIU, S. LI, H. YANG, R. LIU, J. AND WANG, Y. 2008. Effects of Methanol/Gasoline Blends on a Spark Ignition Engine Performance and Emissions. *Energy and Fuels*, 22, 1254-1259.

Wei, L. Tang, C. Man, X. 2012a. High temperature ignition delay times and kinetic study of furan. *Energy & Fuels* 26(4): 2075-2081

Wei, L. Li, Z. Tong, L. 2012b. Primary Combustion Intermediates in Lean and Rich Low-Pressure Premixed Laminar 2-Methylfuran/Oxygen/Argon Flames. *Energy & Fuels* 26:6651-6660.

Wilson, T.S. Xu, H. Richardson, S. 2005. An Experimental Study of Combustion Initiation and development in an Optical HCCI Engine. SAE Technique paper

2005-01-2129.

Wu, X. Daniel, R. Tian, G. Xu, H. Huang, Z. Richardson, D. 2011. Dual-injection: The flexible, bi-fuel concept for spark-ignition engines fuelled with various gasoline and biofuel blends. *Applied Energy*. 88 (2011) 2305–2314.

Wu, X. Huang, Z. Yuan, Kuiwen, Z. Wei, L. 2009. Identification of combustion intermediates in a low-pressure premixed laminar 2,5-dimethylfuran/oxygen/argon flame with tunable synchrotron photoionization. *Combustion and Flame*. 156(2009)1365-1376.

Wu, X. Li, Q. Fu, J. Tang, C. Huang, Z. Daniel, R. Tian, G. Xu, H. 2012. Laminar burning characteristics of 2,5-dimethylfuran and iso-octane blend at elevated temperatures and pressures. *Fuel*. 95 (2012) 234–240.

Wu, X. Huang, Z. Wang, X. Jin, C. 2011. Laminar burning velocities and flame instabilities of 2,5-dimethylfuran-air mixtures at elevated pressures. *Combustion and Flame* 158(3): 539-546

Yaws, C.L. 2011. Yaws' Handbook of properties of the chemical elements. Available from:

http://app.knovel.com/web/toc.v/cid:kpYHPCE007/viewerType:toc/root_slug:yaws-handbook-of-properties-of-the-chemical-elements [Accessed: 02/04/2014]

Zhang, J. Jing, W. Fang, T. 2012. High speed imaging of OH* chemiluminescence and natural luminosity of low temperature diesel spray combustion. *Fuel*. 99:226-234

Zhang, Q. Chen, G. Zheng, Z. Liu, H. Xu, J. Yao, M. 2013. Combustion and emissions of 2,5-dimethylfuran addition on a diesel engine with low temperature combustion. *Fuel*. 103 (2013) 730–735.

Zhang, Z. Huang, Z. Wang, X. Xiang, J. Wang, X. Miao, H. 2008. Measurements of laminar burning velocities and Markstein lengths for methanol–air–nitrogen mixtures at elevated pressures and temperatures. *Combustion and Flame*. 155:358–68.

Zhao, H. Ladammatos, N. 2001. *Engine Combustion Instrumentation and Diagnostics*.: SAE International.

Zhao, H. 2009a. *Advanced Direct Injection Combustion Engine Technologies and Development: Gasoline and gas engines (Vol. 1)*. p2. Cambridge: Woodhead publishing limited

Zhao, H. 2009b. *Advanced Direct Injection Combustion Engine Technologies and Development: Gasoline and gas engines (Vol. 1)*. P3. Cambridge: Woodhead

publishing limited

Zhao, H. 2009c. Advanced Direct Injection Combustion Engine Technologies and Development: Gasoline and gas engines (Vol. 1). p30. Cambridge: Woodhead publishing limited

Zhao, H. Holladay, J. E. Brown, H. Zhang, Z. C. 2007. Metal chlorides in ionic liquid solvents convert sugars to 5-hydroxymethylfurfural. *Science*. 316: 1597-600.

Zhao H. 2012. Laser Diagnostics and Optical Measurement Techniques in Internal Combustion Engines. SAE International.

Zhao H and Ladommatos N. 1998. Optical Diagnostics for In-cylinder Mixture formation measurement in IC engines. *Proc Energ Combust*. 24 (4):297-336.

Zhong, S. Daniel, R. Xu, H. Zhang, J. Turner, D. Wyszynski, M. L. Richards, P. 2010. Combustion and Emissions of 2,5-Dimethylfuran in a Direct-Injection Spark-Ignition Engine. *Energy & Fuels*. 24 (5) 2891-2899

Zhou, J. X., Cordier, M., Mounaïm-Rousselle, C., & Foucher, F. 2011. Experimental estimate of the laminar burning velocity of iso-octane in oxygen-enriched and CO₂-diluted air. *Combustion and Flame*, 158(12), 2375-2383.